POLITECNICO DI MILANO

Facoltà di Ingegneria Industriale

Corso di Laurea Magistrale in
Ingegneria Aeronautica

Numerical investigation of Turbulence Models around an isolated tyre

Relatore: Prof. Sergio DE PONTE

Tutor Aziendale Ing. Nicolò PETRUCCI

Co-relatore: Prof.

Tesi di Laurea di:

Valentina LUCIFREDI Matr. 711779

Anno Accademico 2009 - 2010

Volli e volli sempre, e fortissimamente volli
V. Alfieri

Abstract

The work hereby presented regards a deep investigation, conducted using computational fluid dynamic methods (CFD), with the goal of identifying the best meshing and modelling setup to resolve the flow around an isolated tyre.

Commercial software are used, and all the available features are analysed and used in order to reach a result as close as possible to experimental data. The aim of the first part of the work is to render the computational box mesh insensitive, while the second part deals with the identification of the best turbulence model, considering the computational efforts. In addition, unsteady simulations are executed and compared with the previous ones.

In the final part, a little digression about the shape of the tyre wake is illustrated. Conclusions and further recommendations end the job.

Riassunto

Nel Motorsport la necessità di descrivere il comportamento del fluido che investe la ruota anteriore e la conseguente scia risulta di vitale importanza per la progettazione dell’intera vettura monoposto. Considerando il grande costo delle prove sperimentali in galleria del vento e le pochissime ore di test su pista permesse, è opportuno sfruttare la simulazione numerica come fase fondamentale di progetto.

L’obiettivo di questo lavoro di tesi è stato quello di trovare, per un determinato un codice commerciale [29] la giusta messa a punto delle grandezze caratteristiche atte ad ottenere simulazioni numeriche le più fedeli alla realtà sperimentale per quanto riguarda una ruota isolata. Sono stati utilizzati come dati sperimentali quelli pubblicati da Fackrell [7], ottimo riferimento anche per precedenti lavori [8].

Tramite un modello CAD [27] si è descritta la geometria della simulazione, la quale è stata discretizzata superficialmente usando dei triangoli [28]; successivamente, si è svolta una suddivisione in volumi di tipo non strutturato, ovvero con elementi molto fitti intorno al corpo andando ad aumentare la loro dimensione via via che ci si allontanava dal corpo in esame.

Il codice commerciale utilizzato [29] svolge il calcolo delle Equazioni mediate di Reynolds, stazionarie e non stazionarie, applicando la tecnica dei volumi finiti e presenta svariate soluzioni per approssimare il tensore degli sforzi di Reynolds, altresì note come modelli di turbolenza.

La campagna di simulazioni prevedeva, in una prima fase, la variazione di parametri di discretizzazione del dominio in modo da ottenere un risultato che diventasse indipendente dalla tipo di suddivisione dello stesso. In particolare, data la grande difficoltà a determinare con esattezza il punto di separazione sulla ruota, si è deciso di indagare nella porzione di fluido immediatamente a ridosso del battistrada: in altre parole, si è andato ad investigare quanto sia necessario risolvere approfonditamente lo strato limite per ottenere una simulazione accettabile.

Trovato il miglior compromesso tra costo computazionale - siccome l’aumento di celle comporta un tempo maggiore per calcolare i dati - e veridicità dei risultati trovati, ed avendo notato che il punto di separazione non era perfettamente modellato - trovandosi difatti molto più a valle rispetto all’evidenza sperimentale - si è provveduto a svolgere una simulazione imponendo una parte di flusso laminare attorno ad una porzione di battistrada (secondo Fackrell [7] possiede questo comportamento). Le simulazioni non condussero l’effetto desiderato, anzi in un caso avvenne una separazione in corrispondenza del cerchio che portò il coefficiente di resistenza, dato preliminare principe per i riferimenti, a valori di gran lunga superiori rispetto a

quelli sperimentali, conducendo l’autore di questa tesi alla conclusione che detta separazione non sia effettivamente avvenuta durante le prove in galleria del vento.

Successivamente, mantenendo congelati i parametri di discretizzazione, sono stati variati i sopraccitati modelli di turbolenza e modelli di parete, ovvero il tipo di calcolo da effettuare all’interno dello strato limite. Sono stati utilizzati modelli ad una equazione (Spalart-Allmaras), a due equazioni (K-ε e K-ω SST), e modelli di approssimazione di tutto il tensore (RSM: Reynolds Stress Model). Per quanto riguarda i modelli di parete si è utilizzato un modello denominato “all y+” ed uno denominato “low y+”: nel primo, il solutore decretava quale tipo di approssimazione utilizzare a seconda di dati in suo possesso, il secondo risolveva accuratamente tutto lo strato limite. Da queste prove si è evinto che il miglior caso, in termini di coefficienti di portanza e resistenza si è rivelato essere quello basato sui modelli “K-ε low y+”. Menzione particolare va attribuita al comportamento del modello Spalart-Allmaras il quale fornisce un andamento qualitativo delle grandezze del campo di moto per nulla inferiori ai più accurati modelli a due equazioni, con il vantaggio di una maggiore velocità di convergenza.

Si è provveduto, infine, a svolgere anche simulazioni non stazionarie; Sono state impiegate due diverse condizioni iniziale, una basata sul miglior risultato del caso stazionario, l’altra semplicemente inizializzando il campo di moto. I risultati forniti presentano miglioramenti, ma non di grande entità, solo nel caso di utilizzo come condizione iniziale il risultato della simulazione stazionaria.

Si è voluto altresì indagare la forma della scia provocata dalla ruota, la quale risulta essere determinata da due paia di vortici controrotanti, di cui quello superiore decade rapidamente, mentre quello inferiore, alimentato dai contributi forniti dall’impronta al suolo e dal terreno sembra resistere per una distanza maggiore. In ultima analisi, è stato determinato che anche la forma del cerchione può contribuire all’ampiezza longitudinale di entrambe le coppie di vortici.

In conclusione, la soluzione delle Equazioni mediate di Reynolds presenta notevoli difficoltà in presenza di forti ricircolazioni: un modo per diminuire, ma non per eliminare il problema, è quello di risolvere accuratamente lo strato limite che avvolge la ruota stessa. La predizione del coefficiente di portanza dipende dal punto di separazione, difficile da identificare con questo tipo simulazione, pertanto questo valore contiene un maggior scostamento rispetto al suo valore sperimentale.

Per indagini future, l’autore suggerisce di fare ricorso ad un nuovo tipo di inizializzazione sfruttando, ad esempio, il risultato di un codice a potenziale, oppure, data la non efficienza della legge di parete implementata per modelli di turbolenza differenti dal K-ε, si invita a trovare o definirne altri tipi compatibili con il comportamento dei corpi tozzi. Infine, data la grande importanza nel campo del Motosport per quel che riguarda l’interazione con il suolo, si propone un tipo di simulazione aerodinamica con lo pneumatico deformato, frutto del risultato di una simulazione strutturale utilizzando gli elementi finiti, al fine di determinare con maggior precisione i vortici che si staccano dall’impronta al suolo.

Il presente lavoro è stato condotto durante un periodo di tirocinio presso la Scuderia Toro Rosso sita in Faenza, (RA), Italia.

Ringraziamenti

Vorrei, anzitutto, ringraziare il Professor De Ponte per la pazienza e la grandissima disponibilità avuta per tutto il periodo di realizzazione di questo lavoro. Ringrazio la Scuderia Toro Rosso per avermi dato la possibilità di lavorare nell'eccellenza del Motorsport, quale è la Formula Uno.

Ringrazio l'Ing. Nicolò Petrucci, capo dell'Aerodinamica e l'Ing. Silvio Lorenzo, capo dell'Ufficio CFD, per l'occasione fornitami e per tutto il supporto tecnico e logistico durante la mia permanenza a Faenza.

Ringrazio tutti i colleghi dell'Ufficio Aerodinamico CFD, Fabrizio, Emanuele, Nicola, Marco, Matteo, Luigi, ricordandogli che da ognuno di loro porto e conserverò sempre un insegnamento, sia di vita che di approccio al lavoro; un ringraziamento speciale va a Fabrizio per avermi fornito spunti di sviluppo molto interessanti per la tesi.

Ringrazio la mia famiglia, mamma papà e il mio carissimo fratellino, per avermi sostenuta nei momenti difficili, spronata alla lotta di fronte alle avversità e di non aver mai smesso di ricordarmi chi sono.

Ringrazio le mie amiche, Carlotta Stefania Annabella Benedetta e Valeria, perché sono amiche, indipendentemente da quanto io mi sia fatta sentire e gli voglio bene per questo.

Ringrazio il mio collega ed amico, Giulio per essere sempre stato disponibile, i Davidi e Elisa per il tempo trascorso insieme durante questa splendida esperienza universitaria.

Infine un ringraziamento speciale va a due personalissimi angeli custodi: avrei voluto che foste presenti, ma so che da lassù non mi lascerete mai sola. Questo lavoro è interamente dedicato a voi.

Valentina Lucifredi

Contents

Abstract I

Riassunto III

Ringraziamenti VII

List of figures XI

List of tables XIV

1 Introduction 1
- 1.1 Motorsport aerodynamic development 2
- 1.2 An Introduction to Numerical Techniques and their Automotive Aerodynamics Applications 3
- 1.3 Aims and object 6
- 1.3 Layout of the thesis 6

2 Literary Review 7
- 2.1 Wind tunnel testing 7
- 2.2 Computational model 15

3 Modelling 19
- 3.1 Tyre modelling 19
- 3.2 Boundary condition and initial value 27
- 3.3 Governing equations 28
- 3.4 Wall treatment 33
- 3.5 Turbulence suppression 34
- 3.6 Convergence Criteria 34
- 3.6 Turbulence models 36
  - 3.7.1 K-ε 36
  - 3.7.2 K-ω SST 40
  - 3.7.3 Spalart Allmaras...43
  - 3.7.4 RSM: Reynolds Stress Model 46

4 Results 51
- 4.1 The influence of meshing parameters 52
- 4.2 The introduction of turbulent suppression 57
- 4.3 The influence of turbulent model 64
- 4.4 Unsteady simulation 83
- 4.5 Flow features 87

5 Conclusions 101
- 5.1 Meshing conclusions 101
- 5.2 Turbulence models conclusions 102
- 5.3 Further recommendations 104

Bibliography 107

List of Figures

1.1 Aerodynamic force breakdown of a Formula 1 2
2.1 Fackrell Experimental configuration 9
2.2 Surface Static Pressure Distribution on the Centreline of a Rotating Wheel (Fackrell) 10
2.3 Surface Static Pressure Distribution on the Centreline of a Stationary Wheel (Fackrell) 10
2.4 Flow over an Isolated Wheel (Fackrell) 11
2.5 The Wake Behind Rotating and Stationary Isolated Wheels (Fackrell) .12
2.6 The Wake Behind Rotating and Stationary Isolated Wheels (Fackrell) .13
2.7 Stationary Groundplane Pressure Distributions Beneath an Isolated Rotating Wheel at Various Ride Heights (Cogotti) 14
3.1 Fackrell's B2 wheel 20
3.2 Computational domain 20
3.3 Fackrell's wheel. Front view 21
3.4 Fackrell's wheel. Front view 2 21
3.5 Detail of the contact patch 23
3.6 Split of tyre tread 23
3.7 Wheel meshed 24
3.8 Coordinate system used for the refinement boxes 25
3.9 Refinement box: Contact Patch 26
3.10 Refinement box: Tyre 26
3.11 Refinement box: Downstream 26
3.12 Refinement box: CAR 26
3.13 Refinement box: CAR Big 26
3.14 Streamwise mesh view 27
3.15 Particular of the prism layer on ground, contact patch and tyre 27
3.16 Diffusive term 32
4.1 Residuals. Top run 012, bottom run 022 53
4.2 Drag coefficient value vs iteration. Top 012, bottom run 022 54
4.3 Contour mean streamwise velocity. Top: 4 prism on ground 4 on tyre; bottom: 4 prisms on ground 8 on tyre 55
4.4 Contour mean streamwise velocity. Top: 12 prism on ground 12 on tyre; middle: 12 prism on ground 22 on tyre bottom: 22 prisms on ground 22 on tyre 56
4.5 Contour turbulent viscosity ratio. Top: turbulent suppression from stagnation point to 20°. Bottom: turbulence suppression from stagnation to 80° 58

4.6 Contour mean positive streamwise velocity Top: turbulent suppression from stagnation point to 20°. Bottom: turbulence suppression from stagnation to 80° 59
4.7 Contour mean positive streamwise velocity for turbulent suppression from stagnation point to 20°. From top to bottom: x = 0.5D, x = 0.75D, x= 1D 60
4.8 Contour mean positive streamwise velocity for turbulent suppression from stagnation point to 80° From top to bottom: x = 0.5D, x = 0.75D, x= 1D 61
4.9 Contour mean positive streamwise velocity at z = 0.25 D turbulence suppression from stagnation to 20° 62
4.10 Contour mean turbulent kinetic energy. From top to the bottom turbulence suppression from stagnation to 20°, turbulence suppression from stagnation to 80°, no turbulent suppression 63
4.11 Direction tangential coordinate 64
4.12 Pressure Coefficient in centreline From top to bottom: K-ε all y+, K-ε low y+, K-ω SST, Spalart-Allmaras, Reynolds stress model 66
4.13 Contour turbulent viscosity ratio. From top to bottom: K-ε all y+, K-ε low y+, K-ω SST, Spalart-Allmaras, Reynolds stress model 69
4.14 Contour turbulent kinetic energy (top) and turbulent dissipation rate (bottom) for the K-ε all y+ 70
4.15 Contour turbulent kinetic energy (top) and turbulent dissipation rate (bottom) for the K-ε low y+ 71
4.16 Top view of turbulent dissipation rate for the K-ε all y+ (top) and K-ε low y+ (bottom) 72
4.17 Contour turbulent kinetic energy (top) and turbulent dissipation rate (bottom) for the K-ω SST 73
4.18 Contour turbulent kinetic energy (top) and turbulent dissipation rate (bottom) for Reynolds stress model 74
4.19 Contour mean positive streamwise velocity. From top to bottom: K-ε all y+, K-ε low y+, K-ω SST, Spalart-Allmaras, Reynolds stress model ... 76
4.20 Contour mean positive streamwise velocity for K-ε all y+. From top to bottom: x = 0.5D, x = 0.75D, x = 1D 78
4.21 Contour mean positive streamwise velocity for K-ε low y+. From top to bottom: x = 0.5D, x = 0.75D, x = 1D 79
4.22 Contour mean positive streamwise velocity for K-ω SST. From top to bottom: x = 0.5D , x = 0.75D, x = 1D 80
4.23 Contour mean positive streamwise velocity for Spalart-Allmaras. From top to bottom: x = 0.5D, x = 0.75D, x = 1D 81
4.24 Contour mean positive streamwise velocity for Reynolds stress model. From top to bottom: x = 0.5D, x = 0.75D, x = 1D 82
4.25 Pressure Coefficient in centreline unsteady simulation with steady restart (Top); unsteady simulation without steady restart (Bottom) 84

4.26 Contour of Turbulent viscosity ratio unsteady simulation with steady restart (Top); unsteady simulation without steady restart (Bottom) 85
4.27 Contour of Turbulent kinetic energy unsteady simulation with steady restart (Top); unsteady simulation without steady restart (Bottom) 86
4.28 Isosurface of lambda 2 criterion for steady simulation for K-ε low y+ .87
4.29 Isosurface of lambda 2 criterion for steady simulation for K-ε low y+, top view 88
4.30 Mean positive streamwise velocity as function of z at x=0.35D. From top to bottom: K-ε all y+, K-ε low y+, K-ω SST, Spalart-Allmaras, Reynolds stress model unsteady with steady restart, unsteady without steady restart 91
4.31 Mean positive streamwise velocity as function of z at x=0.5D . From top to bottom: K-ε all y+, K-ε low y+, K-ω SST, Spalart-Allmaras, Reynolds stress model, unsteady with steady restart, unsteady without steady restart 94
4.32 Mean positive streamwise velocity as function of z at x=0.75D . From top to bottom: K-ε all y+, K-ε low y+, K-ω SST, Spalart-Allmaras, Reynolds stress model, unsteady with steady restart, unsteady without unsteady restart 97
4.33 Mean positive streamwise velocity as function of z at x=1D. From top to bottom: K-ε all y+, K-ε low y+, K-ω SST, Spalart-Allmaras, Reynolds stress model, unsteady with steady restart, unsteady without unsteady restart 100

List of Tables

2.1 The Effect of Wheel Edge Profile on the Lift and Drag Coefficients of a rotating (top) or stationary (bottom) Isolated Wheel (Fackrell) 9
2.2 Summary of Literature Review 18
4.1 Experimental values found by Fackrell 51
4.2 Number of simulation, number of prism layer on ground and on the tyre, drag and lift coefficient with their error from the experimental data 52
4.3 Number of simulation turbulence suppression portion, drag and lift coefficient with their error from the experimental data 57
4.4 Number of simulation, Turbulence model, drag and lift coefficient with their error from the experimental data 64
4.5 Number of simulation, drag and lift coefficient with their error from the experimental data 83

Chapter

1

Introduction

Aerodynamics is one of the areas in which automotive science has most advanced over the last few years. A multitude of development goals has arisen to accompany the primary aim of improved fuel efficiency through drag reduction. Newer goals include lift control and cross-wind response to improve high-speed stability, and flow control to reduce spray and soiling in adverse weather conditions.

Nowhere are the goals clearer than in the world of motorsport, where maximizing lift-to-drag ratio is of primary concern. The multi-million dollar aerodynamic development budgets in the upper echelons of the sport reflect the huge performance increases that can be realised through aerodynamic optimization. As time pressures are high in all industrial aerodynamic development, there exists an opportunity for parallel academic research into the more fundamental aspects of automotive aerodynamics.

This chapter will introduce the current state of aerodynamic research within the motorsport industry and highlight, the type of numerical scheme and tools used to describe the behaviuor of the flow using the computer.

From this, the aims and objectives of this study will be presented in the context of extending the available knowledge base to establish the strengths and the weaknesses of the numerical method applied, and clarify the structure of the identified wheel wake. The layout of the whole work will conclude this introductory chapter.

1.1 Motorsport aerodynamic development

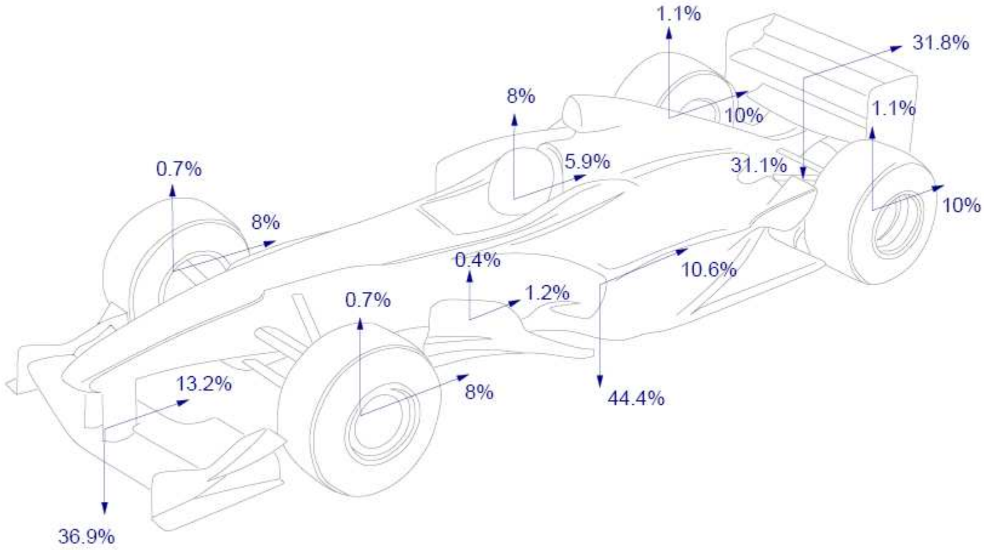

Figure 1.1 Aerodynamic force breakdown of a Formula 1 car

As the demand for wind-tunnel time, and the scale and complexity of testing has increased, the motorsport industry has been forced to move from the rental of aerospace wind-tunnels to the construction of multi-million dollar facilities which better serve the needs of automotive aerodynamics. Chief among these needs is the suppression, or removal, of the boundary layer from the wind tunnel floor in the vicinity of the model. This is accomplished in many motorsport wind tunnels by a combination of mass-transfer and a continuous-belt rolling road, spanning the tunnel working section. The boundary layer is scooped or sucked away before the model and the remaining freestream flow is directed onto the road which, being moving at the freestream speed, does not cause a new ground boundary layer to develop. Whilst other methods are equally effective at boundary layer control, the rolling-road has the added bonus of being able to provide wheel rotation, another of the needs of automotive aerodynamic investigations.

The model is commonly suspended above the ground using an overhead support strut, as the rolling road precludes supporting the model from below. The aerodynamic forces acting on the model are measured using a balance contained within either the car or the support. Generally, the models are also instrumented to record the pressure distribution in key areas such as the wings, floor and radiators. Many of the model components are actively controllable, allowing the configuration of the car to be changed without stopping the tunnel. Such changes include ride height, chassis rake and front-wing flap angle. Other detailed components to be found on many race car models include ventilated brake discs, blown exhausts and engine-air induction.

Constant improvements in aerodynamic performance are often attributable to slight improvements in a multitude of components, rather than a massive change in a few. As the testing methods strive to resolve smaller and smaller differences, the fidelity of those methods becomes of paramount importance. The following sections outline two such issues that have arisen regarding wheel simulation methods.

The exposed wheels of *monoposto* (single-seat) racecars, such as Formula One cars, are tightly regulated to ensure that the formulae retain their distinctive appearance. Figure 1.1 illustrates the force contributions of the major components of a modern Formula One car. It clearly shows that, at around 10 % of the total vehicle drag each, the exposed wheels have a considerable impact on the overall aerodynamic performance of the car. Whilst maintaining the appearance of the car, the regulations also effectively remove the opportunity to reduce this value significantly.

As previously described, the cost and the complexity of a wind tunnel tests are relevant. It is therefore advantageous to use other types of design and analysis tools, with shorter downtime and lower costs; between the possibilities available, Computational Fluid Dynamic techniques can be used in order to have a preliminary estimation of the solution.

1.2 An Introduction to Numerical Techniques and their Automotive Aerodynamics Applications

Computational Fluid Dynamics, or CFD, is the generic term given to the range of techniques and procedures involved in obtaining a numerical solution for the flow of a fluid around, or through, the object of interest. As computer technology has developed over the past twenty-five years so has the complexity of simulation techniques.

In terms of increasing computational effort, these methods can be summarized as:

- Linear Methods: Vortex Lattice and Panel Codes

- Non-Linear Methods:
    - Inviscid or Euler
    - Time Averaged Viscous - Steady State Reynolds Averaged Navier-Stokes Equations (RANS)
    - Unsteady Viscous Methods:
        - Unsteady RANS (URANS)
        - Large Eddy Simulation
        - Direct Numerical Simulation

Imposing the condition of irrotational flow and neglecting the viscous terms reduces the steady Navier-Stokes equations down to the linear Laplace equation. Both vortex lattice and panel method codes are methods that only involve discretization of the surfaces of interest. Whilst these methods can be coupled with corrections for both boundary layer and wake effects, they are seldom used today in the field of production car aerodynamics. However, they are still used in racing car development, particularly for initial design analysis of wing sections, [1].

The addition of non-linear terms in the governing equations to be solved dramatically increases the complexity of the numerical method. Whilst inviscid, or Euler, methods only add first order partial differential terms the complexity of viscous interactions in the flow fields of interest, this simplification is generally considered irrelevant in vehicle aerodynamics. Simulation of viscous flow fields means solving second order partial differential equations.

Consider a fully turbulent flowfield. The time-dependent dynamics of the fluid will be governed by the Navier-Stokes equations, for which many derivations exist in print, for example Batchelor, [1]. The turbulence itself is characterised by fluctuations in all of the fluid variables around mean values. These small-scale turbulent components are computationally very intensive to resolve and hence the classical approach is to average the instantaneous equations, in time, over these turbulent fluctuations. The fluid motion is split into two components; a mean flow, upon which a second fluctuating flow is superimposed. This leads to the time-dependent Reynolds Averaged Navier-Stokes (RANS) equations. Averaging over much larger time steps typical of the mean flow components gives the steady state RANS equations.

Direct Numerical Simulation, DNS, is the term given to the solution of the complete unsteady Navier-Stokes equations. An intermediate step between DNS and RANS is Large Eddy Simulation, LES, where the larger turbulent eddy length scales are solved, and the smaller eddies are modelled empirically.

Due to the computational demands of the last two numerical methods, viscous simulation of vehicle aerodynamics generally employs RANS methods, usually steady state. However, this introduces turbulence modelling. The simplifications employed in the governing equations means that products of the fluctuating terms, the so-called Reynolds Stresses, exist, leading to a number of unknowns greater than the number of equations. Therefore, closing the set of RANS equations requires the addition of further equations, such the turbulence model, so that the effect of the turbulent motion on the mean flow can be modelled. This means that the realism of a flow simulation with RANS methods is highly dependent on the turbulence model employed.

To calculate the solution, the continuum properties of the RANS equations have to be discretized, in terms of both the fluid volume of interest and the mathematical equations. This discretization of the space through which the fluid passes is known as mesh generation, and it is only this grid that provides the solver with geometric information.

Whilst linear methods only require the body surface to be meshed, all the other schemes require meshing of both the geometry of interest and the surrounding computational domain. Thus, if a geometric component or flow region is not resolved adequately with the mesh, it becomes impossible for the solver to give an adequate solution in this area. However, no theoretical methods are available for determining the appropriate size and detail of the mesh other than numerical experimentation and previous experience.

Thus, for a successful CFD simulation, both the volume mesh and numerical scheme have to be appropriate for the expected flow physics of the solution, otherwise numerical errors tend to dominate. For the complex flows found around automotive shapes, minimising the influence of the numerics requires a lot of effort, and thus much of the published information still relates to numerical effects and not actual conclusions about the aerodynamics modelled. For example, Hajiloo *et al*, [2] and Ramnefors *et al*, [3], have looked at the effects of mesh refinement on the computed solution.

The effectiveness of a turbulence model is not only dependent on the quality of its mathematical reasoning, but also on the computational grid, especially in terms of its requirements for the range of permissible first cell centre $y+$ values' next to, and cell size growth away from, wall boundaries. The many different versions of the k-ε model are still frequent choices for simulations. Comparisons of different types of model are becoming more widely published; for example Ramnefors *et al*, [3], Axelsson *et al*, [4], and Perzon *et al*, [5]. However, no specific turbulence model shows consistently good results; the choice still seems to be dependent on the configuration of interest.

Despite these issues, numerical techniques have been applied to a wide range of automotive problems. Dhaubhadel, [6], provides a comprehensive review. As well as external aerodynamics, climate control, engine cylinder flows and combustion, engine cooling, exhaust systems, engine bay flows, and rotating systems such as disc brakes have all been subject to published CFD studies.

1.3 Aims and object

The main object of this work is to determine a useful set of tools for the investigation of an isolated tyre using numerical software. Since the need of experimental data to correlate the model is crucial, one set of data among the ones used by Fackrell in his deep investigation of the phenomena has been chosen [7]. This choice is motivated not only by the mere necessity of an experimental feedback, but also to compare the outcomes of this project with the numerical results of studies that use this type of wheel [8].

The first phase consists in analysing the result of the simulation, varying mesh characteristics, number of prisms for instance, without varying the type of simulation performed, in order to find a compromise between accuracy of the results and the time necessary to obtain them.

Starting from a suitable set of mesh parameters, the second phase is an investigation about the different type of turbulence model, different equations and Reynolds stress models and their results in term of pressure distribution or wake form.

The work has been carried out during a period of apprenticeship in Scuderia Toro Rosso, Faenza Italy.

1.4 Layout of the thesis

This thesis work is comprised of the following steps. Chapter 2 contains a review of previously published work concerning the aerodynamic properties of wheel flows; this will refer to both experimental and computational data.

Details of modelling of the tyre computational box, meshing parameters volume and superficial feature, followed by a short description of numerical method and computational model used are presented in chapter 3, while chapter 4 contains all the obtained results,divided into meshing and numerical model sensibility.

Chapter 5, the last one, summarises all the most relevant aspects and suggests recommendations for the further works.

Chapter

2

Literature Review

The following pages present a review of the most important work existing in literature concerning the flow around an isolated tyre, divided into wind tunnel testing and computational testing.

2.1 Wind tunnel testing

Morelli, in [9] and [10], was the first to publish details of research specifically related to the flow around a rotating automotive wheel. His work covered flows over both isolated and shrouded wheels. In the 3 m diameter closed working section wind tunnel of the University of Turin a flat plate was mounted parallel to the free stream to represent a stationary ground plane. The solitary exposed wheel, a typical 1960s racing tyre with a diameter of 0.630 m, was located into a rectangular recess in the aforementioned plate, without touching it, in the stated attempt to represent the deflection of the wheel on the ground. Aerodynamic forces and moments were measured with a six components balance connected to the faired driveshaft of the wheel which could be yawed, together with the ground plane, up to an angle of twenty degrees.

The measurements on the isolated rotating wheel showed a resulting negative vertical force, i.e. a downforce, contrary to the accepted direction of positive lift. The results relating to wheel drag showed that the use of faired rims on the centre of the wheel reduced drag by 22%, whilst wheel drag was doubled by increasing the yaw angle of the wheel from zero to twenty degrees. However, these must be viewed with caution due to the aforementioned wheel lift results.

Stapleford and Carr [11] used a slender streamlined body fitted with four unenclosed wheels as a basis to study the effects of ground plane movement, wheel rotation and wheel ground clearance on vehicle wind tunnel force measurements. Both the MIRA quarter-scale tunnel and the Imperial College 5'×4' tunnel were used. The circular cross-section slender body was fitted, via simple fixed suspension units, with four wheels of 0.1524 m diameter, giving an approximate Reynolds number Re_D of $2.0 \cdot 10^5$. Total forces on the vehicle were measured using an underfloor balance at MIRA, and with an overhead balance at Imperial College. Wheel forces were extracted from the overall forces by subtracting tares for the strut, body, and suspension units at the corresponding ride height. Thus, the interference effects between the body and wheels were not quantified.

The lift generated by the four stationary wheels at a large ground clearance was very small. As this gap was reduced, C_{Lw} the lift coefficient of the wheel, increased rapidly. Wheel drag also increased with decreasing ground clearance. Rotation of the wheels caused a large negative wheel lift to be generated when a gap between the wheels and the stationary ground plane was present. The lift became positive when this gap was sealed with strips of paper. Tuft flow visualization showed that the wheels rotation draws air through the gap between the wheel itself and the groundplane, thus creating large local negative pressures. With zero ground clearance, rotation of the wheels reduces both the overall lift and drag, compared to the stationary case under otherwise identical test conditions.

The effect on the derived wheel forces of using a moving ground plane, as investigated by Imperial College, was found to be small. Most coefficients only changed by a few percent when compared to the same configuration with the belt stationary. The only exception was when the wheels were rotating at a close distance from the moving belt. This was, however, without any seal between the wheels and groundplane. The optimum case of zero gap was not studied due to the contact forces between the wheel and the ground plane not being able to be isolated from the aerodynamic forces.

Probably, the most well-known work concerning isolated wheel aerodynamics is that of Fackrell. This is described briefly in [12] and [13], and in more depth in [7].

Using two wheels of varying profile and tread width, and with a diameter of 0.415m, surface static pressure measurements and total head wake surveys were conducted at a Reynolds Number, Re_D, of $5.3 \cdot 10^5$. The wheels, machined from light alloy, were kept in contact with the moving ground plane by a system of supports not dissimilar to a racing car suspension system, Figure 2.1. A pressure transducer, able to measure the cyclical pressure distribution by means of flush tapping across the semi-span of the wheel surface, was mounted inside mounted inside the wheel hub; its electrical output was recorded outside the wheel with the use of slip rings formed of low noise silver-graphite bushings.

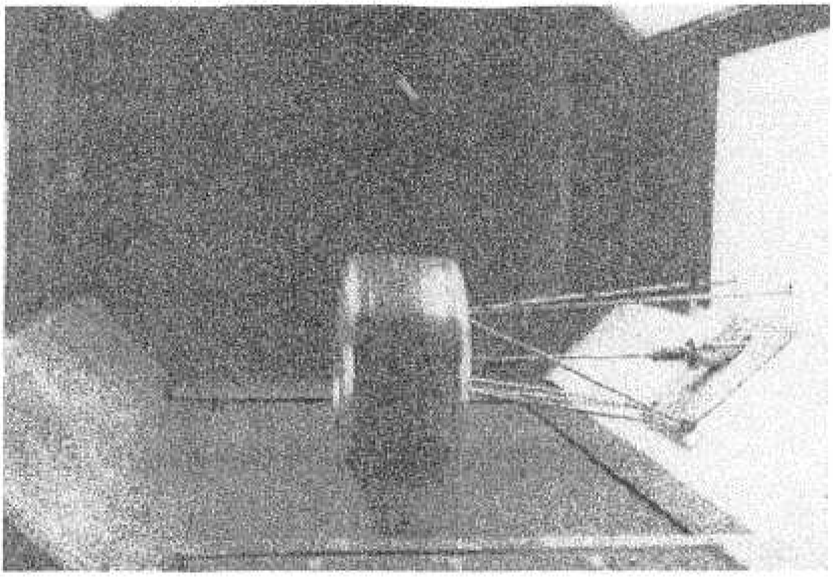

Figure 2.1: Fackrell Experimental configuration

Pressure distributions on the centreline of the wheel are shown in Figure 2.2. The MIRA results are those of Stapleford and Carr, [11], measured with an external static probe. The differences between the two show the effect of tyre profile when the wheel was rotating. Wheel 2 has a more rounded profile than wheel 1, but is slightly narrower (AR=61.2% compared to AR=65.8%, equating to a 5% decrease in frontal area). The pressures on top and behind wheel 2 were found to be more negative, showing that the edge profile can have significant effects on the wake structure even in the plane of the wheel centreline. Integration of the complete set of pressure profiles measured across each wheel gave a higher lift coefficient and a lower form drag coefficient for wheel 2 compared to wheel 1, as summarised in the upper rows of Table 2.1.

Table 2.1: The Effect of Wheel Edge Profile on the Lift and Drag Coefficients of a rotating (top) or stationary (bottom) Isolated Wheel (Fackrell)

Wheel #	C_{dw}	C_{lw}
1	0.40	0.63
2	0.5606	0.4183

Wheel #	C_{dw}	C_{lw}
1	0.5410	0.3010
2	0.5606	0.4183

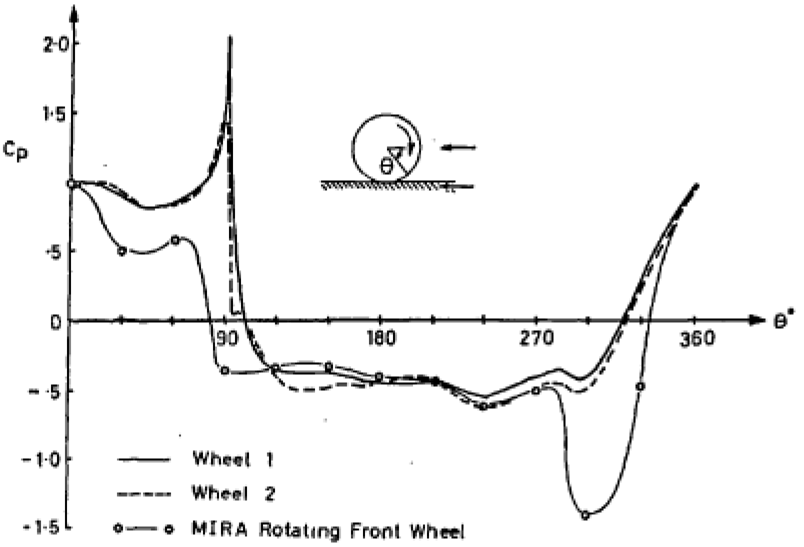

Figure 2.2 Surface Static Pressure Distribution on the Centreline of a Rotating Wheel (Fackrell)

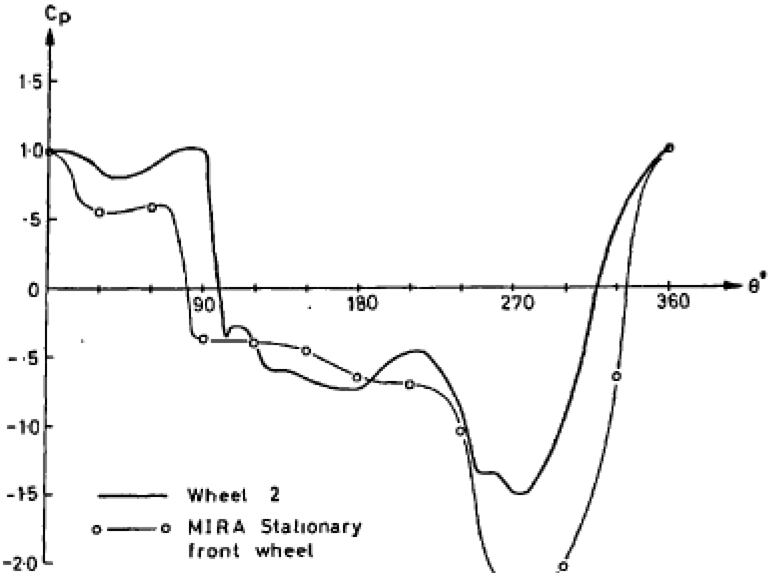

Figure 2.3: Surface Static Pressure Distribution on the Centreline of a Stationary Wheel (Fackrell)

Figure 2.3 shows the major differences between the centreline pressure profiles of a rotating wheel and moving groundplane and these for a fixed wheel and stationary groundplane. A rotating wheel was found to produce very high pressures at the front of the contact patch, whereas a stationary wheel showed a lower base pressure as well as a lower suction pressure on the top of the wheel surface, due to the later flow separation (Figure 2.4). These differences translate in the fact that the stationary wheel produced 73% more lift and 33% more form drag than the rotating wheel under the equivalent test conditions, as summarised in the bottom rows of Table 2.1 at page 9.

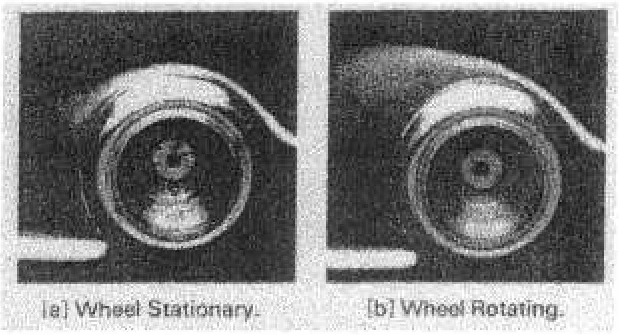
(a) Wheel Stationary. (b) Wheel Rotating.

flow direction: right to left wheel rotation: clockwise

Figure 2.4: The Flow over an Isolated Wheel (Fackrell)

Using the angular notation shown in Figure 2.2, Fackrell postulated that the boundary layer remained attached over the stationary wheel until approximately θ = 210°. The separation process on the wheel centreline was said to be similar to that of a solitary two-dimensional circular cylinder in the trans-critical regime i.e. a laminar separation bubble, turbulent reattachment, and final turbulent separation. When the wheel was rotating, however, the attached wheel boundary layer meant that this type of separation could not occur. As the top part of the rotating wheel moves in the opposite direction to that of the free stream, an iso-surface with zero velocity has to exist within the boundary layer. Fackrell suggested that the centreline "separation" point for a rotating wheel occurred on this zero velocity iso-surface, in a favourable pressure gradient, 70° further forward than in the case of a stationary wheel.

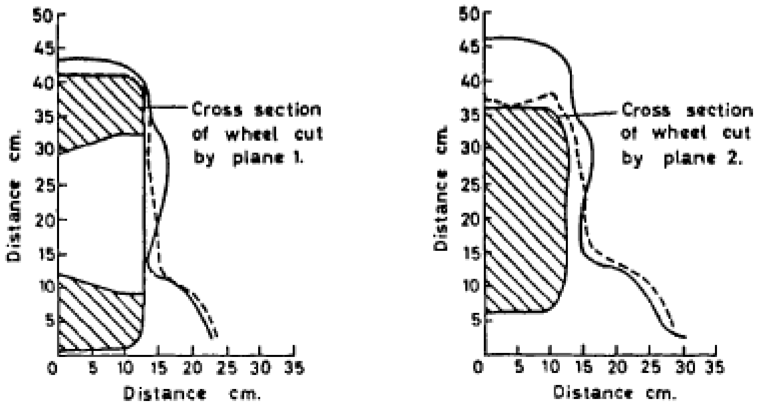

(1.) Plane 1, 4·3 cm. from wheel centre

(2.) Plane 2, 14·5 cm. from wheel centre.

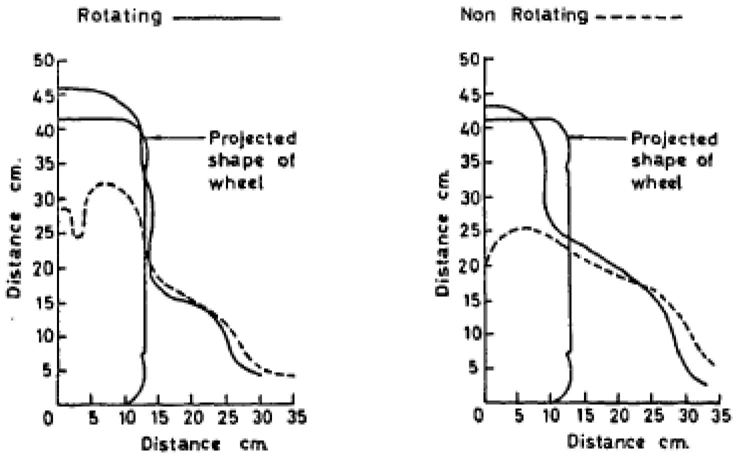

(3.) Plane 3, 21·6 cm. from wheel centre

(4.) Plane 4, 31·6 cm. from wheel centre.

Figure 2.5: The Wake Behind Rotating and Stationary Isolated Wheels (Fackrell)

Investigations into the characteristics of the wake were made with a total head survey, in four planes perpendicular to the free stream, with a Kiel tube which was stated to be insensitive to yaw up to deflection angles of ±35°. Plots of 90% total head, intended to represent the edge of the wake, are shown in Figure 2.5. These support the pressure measurements by showing that the flow “separated” earlier when the wheel was rotating, thus giving a thicker wake. The bulges near the ground plane show the presence of vortices shed from the front of the wheel. For the stationary wheel it was stated that these probably represented the formation of a horseshoe vortex due to the wheel causing upstream ground plane separation (no thickness of this boundary layer was stated).

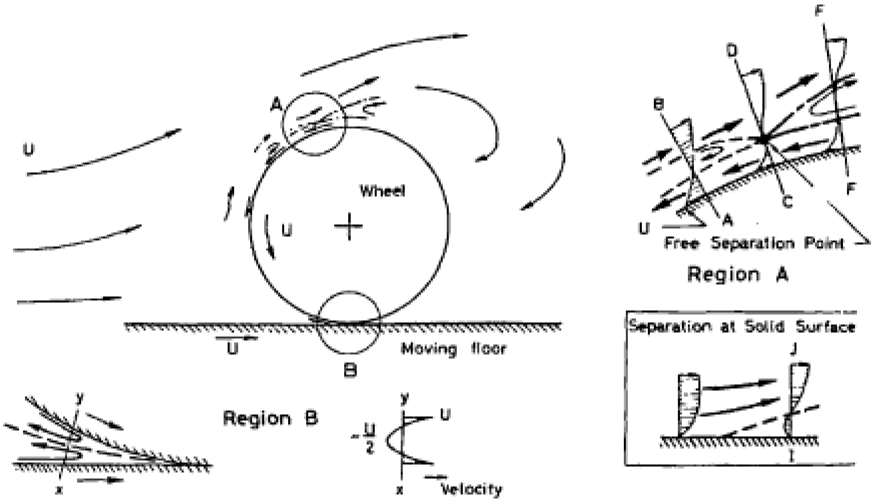

Figure 2.6: The Wake Behind Rotating and Stationary Isolated Wheels (Fackrell)

When the wheel was rotating, the surfaces of the wheel and ground plane converged towards the front of the contact patch at the free stream velocity. Fackrell postulated, Figure 2.6, that air was drawn into this region due to the non-slip conditions, air that was then forced out between the two attached layers. In this very small region the viscous forces dominated, and it was this squeezing of the flow which resulted in pressure coefficients greater than unity. As the wheel was of finite aspect ratio(the ratio between the with and the diameter), this “jet” of air was then deflected sideways by the freestream and then passed down on either sides of the wheel.

Limited investigations were also performed into the effect of wheel aspect ratio and grooves in the wheel surface, similar to those found on current Formula 1 cars.

As part of a study in the Pininfarina wind tunnel about wheelhouse cavity flows, Cogotti [14] also documented a number of initial experiments concerning the flow around isolated wheels. However, no mention of the use of a moving groundplane is made, nor any detail about the characteristics of the fixed groundplane boundary layer is given.

To emphasize the importance of sealing the gap between a rotating wheel and groundplane, pressure measurements on the tunnel floor for a range of wheel to ground distances were made (Figure 2.7). The wheel, a Pirelli 145 SR 10 tyre filled with foam and turned on a lathe until almost slick, was of diameter 0.485m and AR=28%. It was driven by an adjacent faired motor to give matching circumferential wheel and free stream velocities and $Re_D = 1.1 \cdot 10^6$. It was found that, when the rotating wheel approached the ground, the flow in the narrowing gap became increasing accelerated, and hence more negative groundplane pressures were generated beneath the wheel.

However, when the gap between wheel and groundplane was sealed, the pressures at the front of the “contact patch” became positive. The magnitude of this positive pressure was stated to be dependent on the quality of this seal - a foam rubber insert, fitted under slight pressure, between the rotating wheel and tunnel floor was favoured by Cogotti.

For force measurements, the wheel was mounted above a pad of the underfloor balance. Evidence was found of a critical Reynolds number for a stationary wheel which was independent of any fairing on the central hub of the wheel. How this was affected by upstream boundary layer thickness was not considered. The addition of these fairings decreased the wheel drag coefficient; the reduction was greater for a rotating wheel than for a stationary wheel. The drag coefficient for the stationary wheel in contact with the fixed groundplane was slightly greater than for the rotating wheel and, in both cases, the wheel produced positive lift. The stationary wheel generated more lift than the rotating wheel. Changing the yaw angle of the wheel from 0° to 15° increased the drag coefficient of the isolated (i.e. without motor) stationary wheel by 10% and its lift coefficient by 40%.

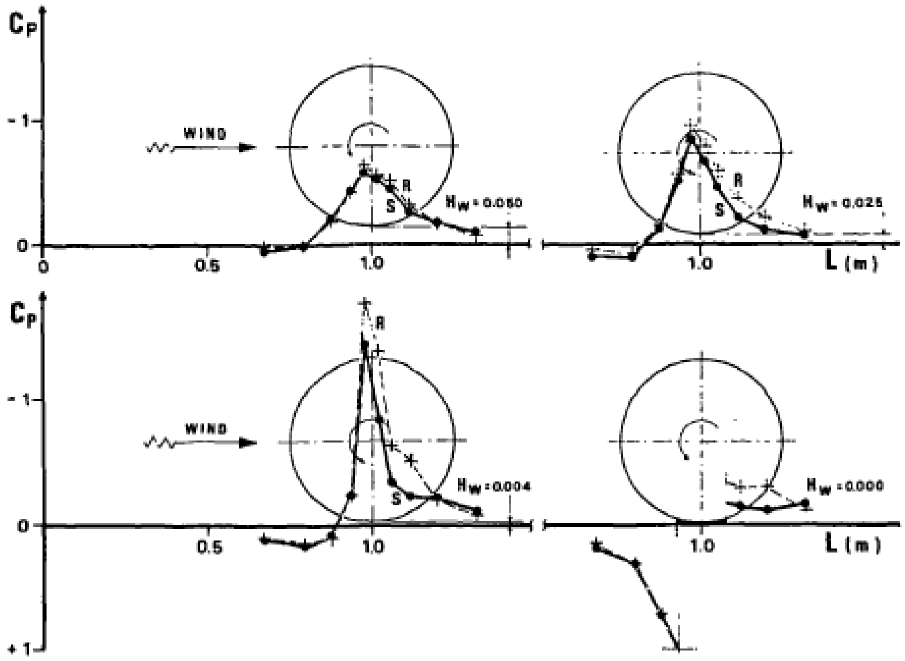

Figure 2.7: Stationary Groundplane Pressure Distributions Beneath an Isolated Rotating Wheel at Various Ride Heights (Cogotti)

Other experimental studies reporting results regarding isolated wheel aerodynamics include Bearman *et al*, [15], who performed further wake studies behind one of Fackrell's wheels with a nine hole pressure probe. Contour plots of both total pressure and vorticity were presented. A taller, narrower wake was found behind the rotating wheel on a moving groundplane when compared to the stationary wheel fixed groundplane case at Re_D $5.5 \cdot 10^5$. Both wakes were dominated by a vortex on either side of the wheel near to the groundplane. The vortices behind the rotating wheel were found to be much weaker, and closer to the wheel, than those behind the stationary wheel.

Both Hilhorst and Giachi [16], and Schiefer *et al* [17], have reported results for isolated wheels both on their own and in an open wheel race-car configuration. It was found that a wheel placed behind another is strongly influenced by the wake flow for separation distances of up to ten wheel diameters. The drag of the rear wheel, in particular, was significantly reduced compared to the value determined in an isolated configuration. However, for the race-car configurations, interactions between the wheel flows and the nearby bodywork surfaces were found to be considerable, and thus the results are not generally applicable to studies of totally isolated wheels.

2.2 Computational model

Basara, Beader and Pzulj [18] joined Axon [8] and Skea [19] in being the first to publish the results of CFD studies of wheel flows, doing so in the late 1990s. Each study used a different commercial, finite-volume code based upon the use of structured grids and Reynolds Averaged Navier-Stokes (RANS) equations. The effects of turbulence models and solver numerics were assessed in each case, although no consensus was reached.

Axon [8] used Fackrell's surface pressure and wake data [7] as validation criteria for his isolated wheel simulations. Both of these showed reasonable correlation, notwithstanding the fact that Axon greatly simplified the wheel geometry. In particular, Axon's model appeared to capture correctly the upstream contact patch jet. The work of Basara, Beader and Pzulj [18] took a similar approach to Axon, although more limited in its scope as it was essentially a promotional exercise by the supplier of the CFD code. Skea [19] used a simplified wheel model: a finite aspect ratio square edged three-dimensional cylinder in ground effect. Both his experimental and computational work used centreline pressures of Fackrell with $Re_D = 6.9 \cdot 10^5$ instead of $Re_D = 5.3 \cdot 10^5$ and the different edge as computational validation.

Whilst the isolated wheel data produced by these studies did not add further information respect Fackrell's work, it did show that CFD could be used to provide qualitative information about this type of flow-field. One particular cause for concern was the poor prediction of flow separation by all turbulence models and discretisation schemes[1].

It is unsurprising that some issues remain, as the RANS turbulence models currently used are essentially those used by Axon, Skea and Basara, Beader and Pzulj in those first studies.

Current studies serve to illustrate the improvement in CFD simulation which has been brought along by increased computational power and enhanced meshing and solution strategies. However, the work of Wäschle et al. [20] showed that improved predictions of both the flow-field and lift force were possible with a code based not upon RANS, but upon the Lattice-Boltzmann method.

Knowles continued the study started with its PhD thesis [21], together with Saddington [22], with the goal of investigating with experimental tests the main structures existing in the near wake of an isolated Formula One wheel rotating in ground contact. A 50 percent-scale isolated wheel assembly, geometrically similar to the configuration mounted on a Formula One racing car, was tested in a closed-return three-quarter open-jet wind tunnel. Using laser Doppler anemometry, three velocity components were measured with a total of 1966 data points distributed across four spanwise planes and within one diameter downstream of the wheel axis. He proposed a revised model of the trailing vortex system induced in the wake of such a wheel, which tries to clarify the contradictory ones published in the literature to date.

Also Axerio and Iaccarino [23] studied experimentally the flow field around a 60% scale stationary Formula 1 tyre in contact with the ground in a closed wind tunnel, in order to validate the accuracy of different turbulence modelling techniques. The results of steady RANS and Large Eddy Simulation (LES) are compared with data from Particle Image Velocimetry (PIV), performed within the same project. The locations of the vortex cores, extracted from the LES and PIV data as well as computed using different RANS models, show that the LES predictions are closet to the PIV vortex cores. All turbulence models are able to accurately predict the region of strong downward velocity between the vortex cores in the centerplane of the tyre, but discrepancies arise when velocity profiles are compared close to the inboard and outboard edges of the tyre, due to the sensitivity of the solution to the tyre shoulder modelling. In the near wake region directly behind the contact patch of the tyre, contour plots of in plane-velocity are compared for all three datasets. The LES simulation again matches well with the PIV data.

As regard as the URANS, the Unsteady Reynols Average Navier Stokes equation, the first was performed by Basara et al., [24] as improvement of the previous work: unfortunately, disparate wheel geometries and limited results make these studies of limited use in assessing the accuracy of the computational methods when applied to the wheel flow.

---

[1] It is important to mention that the RANS equation has problems when the flow presents recirculation.

MacManus and Zhang [25] present a URANS computation of the flow around the exact wheel geometry studied by Fackrell and Harvey [12], and to compare this to their experimental results. They acknowledge that the highly separated three dimensional flow around the wheel is far removed from the thin shear layers used for RANS turbulence model calibration. However, RANS is the method of choice for vehicle aerodynamic simulations and this situation will most probably not change for the foreseeable future because of the prohibitive computational expense of alternative approaches. For the authors, the RANS method is capable of capturing the mean flow structures with good accuracy and to gain an understanding of the mean flow, its constituent structures and their mechanisms of formation. The study also clarifies the understanding of the flow and resolves some of the uncertainties arising from previous studies, providing a new model of the tyre wake.

Table 2.2 tries to summarize in a quick glance what has been described in these few pages.

Table 2.1: Summary of Literature Review

Author & Ref	Type		Wheel		Ground		Reynolds	Measurement
	Exp	CFD	Stat.	Rot	Fix	Mov		
Morelli [9]	X			X	X		$1.25 \cdot 10^6$	6-comp forces
Stapleforr & Carr [11]	X		X	X	X		$2.0 \cdot 10^6$	Lift, Drag Surface static pressure
Cogotti [14]	X		X	X	X		$1.1 \cdot 10^6$	Lift and Drag
Fackrell [7,13,14]	X			X		X	$5.3 \cdot 10^5$	Lift, Drag Surface static pressure
Bearman *et al.* [15]	X		X	X		X	$5.5 \cdot 10^5$	9 hole probe velocities
Knowles *et al.* [22]	X			X		X	$3.7 \cdot 10^5$	Drag 3D-LDA
Axon [8]	X	X	X	X		X	$8.5 \cdot 10^5$	Drag
Skea [19]	X	X	X	X		X	$5.5 \cdot 10^5$	Drag Tyre surface static pressure
Basara [18]		X					n/a	
Washle *et al.* [20,24]	X	X	X	X		X	$5.4 \cdot 10^5$	Drag, Wake total pressure, 2D-LDA
Axerio & Iaccarino [23]	X	X		X		X	$5.0 \cdot 10^5$	PIV, Velocities
Mc Manus & Zhang [25]		X		X		X	$5.3 \cdot 10^5$	Surface static pressure, vorticity vectors, Lift , Drag, Streamlines and Isosurfaces

Chapter

3

Modelling

The current section illustrates the modelling of the tyre, its computational box, its meshing parameters as volume and superficial feature, followed by a short description of numerical method and computational model used.

3.1 Tyre modelling

The work hereby presented has followed the path undertaken by Axon [8], therefore using the B2 Fackrell wheel as the base model for the analyses, and investigating if the change of turbulence model can lead to improvement of his results. Although he used a very simple shape profile, a cylinder of constant diameter, without modelling details such as the rim or the tyre tread, he achieved a discreet accuracy with his mesh and his CFD code. The author hopes to achieve similar corresponding results by using a model which better fits the reality of the experimental simulation, and by using an unstructured mesh, widely used in industrial flow computation.

Figure 3.1 illustrates the tyre modelled by a CAD software [27]; by whom it is also modelled all the computational box, which dimensions are 5D, where D stands for the wheel nominal diameter upstream and 15D direction downstream, 10D in spanwise direction and 5D in height direction, as it can be seen in Figure 3.2.

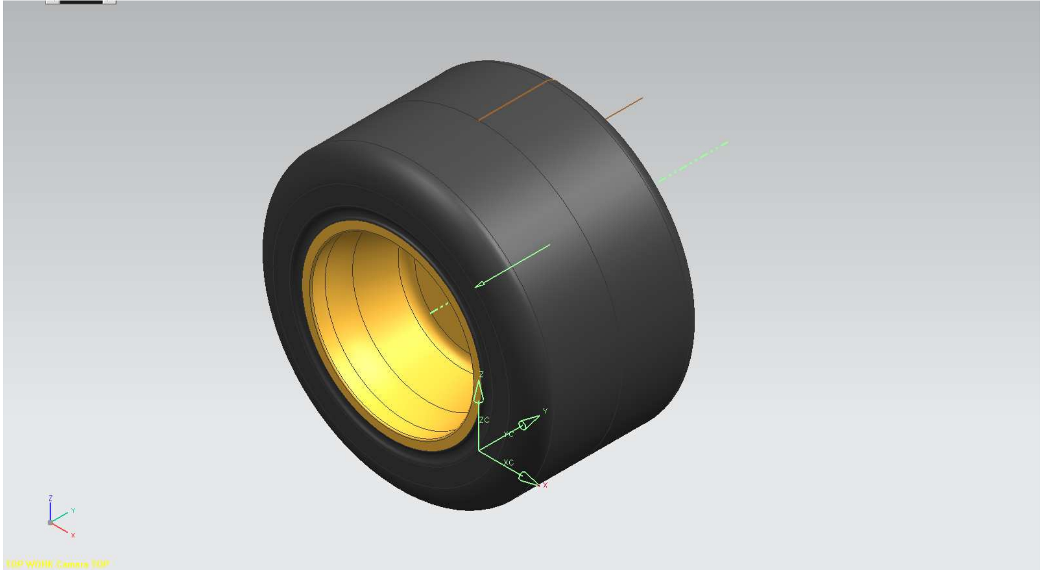

Figure 3.1: Fackrell's B2 wheel

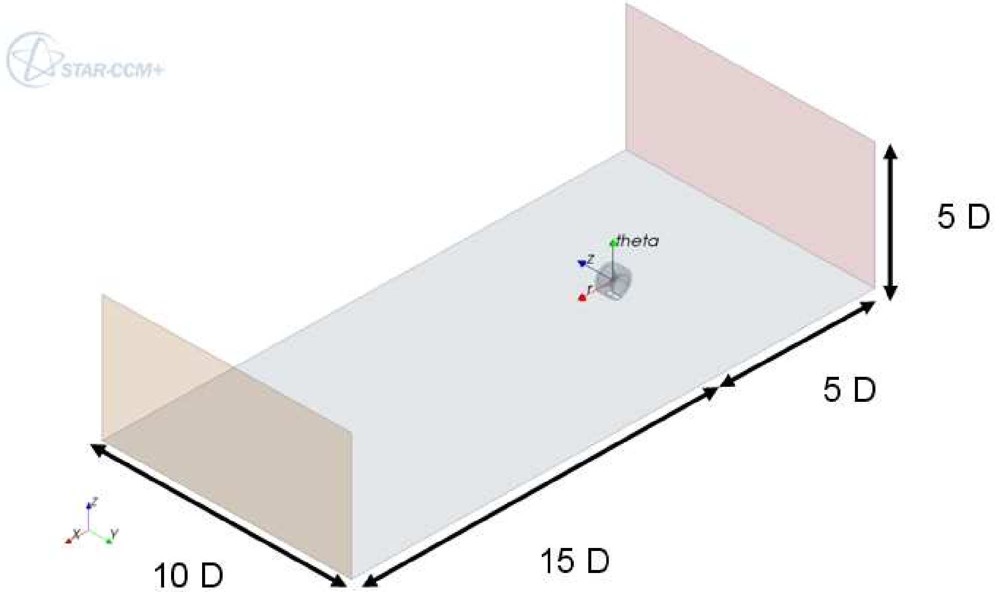
STAR-CCM+
theta
z
r
5 D
5 D
15 D
10 D
Z
X
Y

Figure 3.2: Computational domain

Next Figures 3.3 and 3.4 presents quoted views of the Fackrell's tyre in order to show all the dimensions needed to the reader.

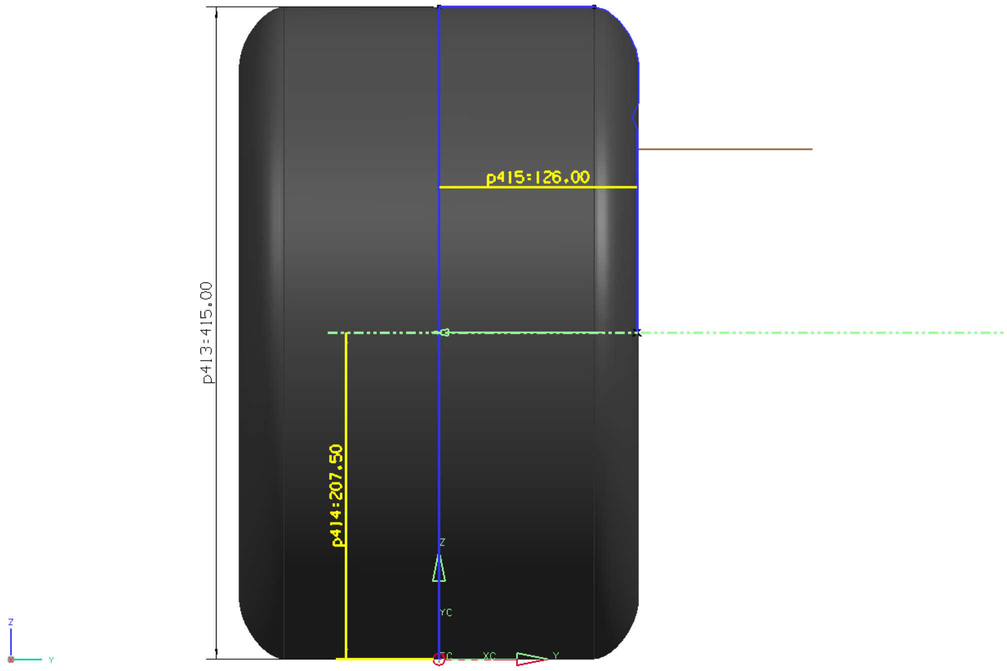
p413:415.00
p415:126.00
p414:207.50
Z
YC
XC
Y
Z
Y

Figure 3.3: Fackrell's wheel. Front view

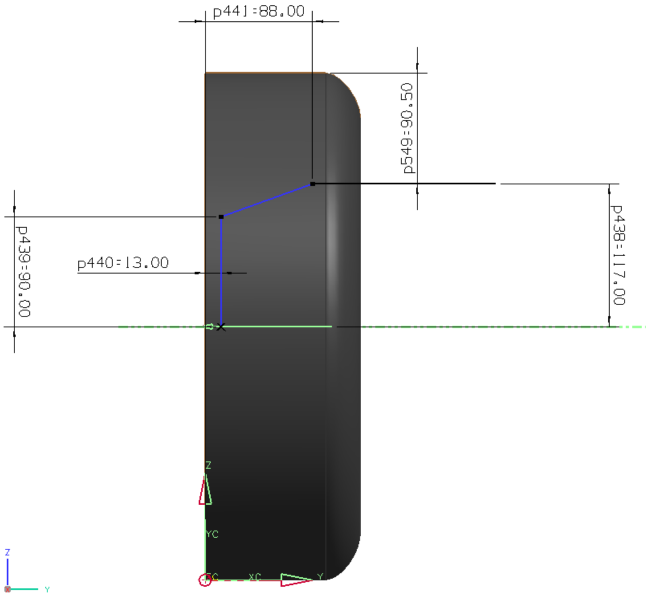
p441:88.00
p549:90.50
p439:90.00
p440:13.00
p438:117.00
Z
YC
XC
Y
Z
Y

Figure 3.4: Fackrell's wheel. Front view 2

Regarding the contact patch, i.e. the interaction between the ground and the tyre, the author has used the same procedure followed by Axon: a solid element represents the connection between the tyre and the ground plane; the size of this part is such to intersect with the tyre at a height of 3 mm above the ground (model depicted in Figure 3.5).

Once the geometry is described by means of a CAD software, the next step has been to mesh the boundaries: the surfaces are divided into triangle through another commercial software, in contrast to what Axon did (he used a structured hexahedral mesh). Before beginning with the meshing operation, the surface of the tyre tread is divided into two different zones: a slice with an amplitude of 120°, symmetrical with respect to the contact patch, is meshed separately from all the rest of the surface in order to obtain a better resolution; Figure 3.6 shows the split of the tyre tread using different colour for better understanding.

Dimensionally speaking, the main common characteristics of the surface mesh are the growth rate, i.e. the geometric growth factor, set to 1.1, and the feature angle, i.e. the maximum allowed angle between normals of two consecutive edges, set to 10°. The length of the elements has a common lower limit of *0.8 mm* in the areas representing the tyre tread; this limit becomes lower reaching *0.4 mm* in the contact patch zone, and higher – up to *2 mm* – in the rim zone. The maximum distance between two nodes is also different depending on the part of the wheel: the bottom part has a lower value of *4 mm*, while the upper one has a limit of *5 mm*. Regarding the contact patch, it is meshed with the same length, *0.4 mm*. The rim, instead, presents a higher length limit of *5 mm*, in order to keep the skewness factor, a quality meshing parameter, under the value of 0.35.

An overview of the whole meshed tyre is represented in Figure 3.7; the mesh is comprised of 238'784 triangles.

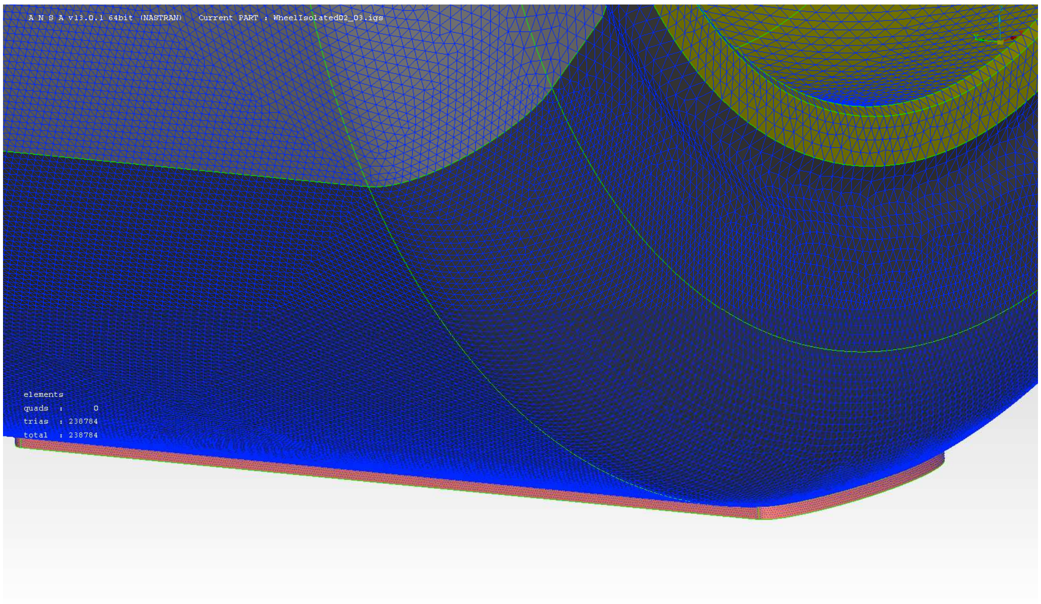
A N S A v13.0.1 64bit (NASTRAN) Current PART : WheelIsolated02_03.igs
elements
quads : 0
trias : 238784
total : 238784

Figure 3.5: Detail of the contact patch

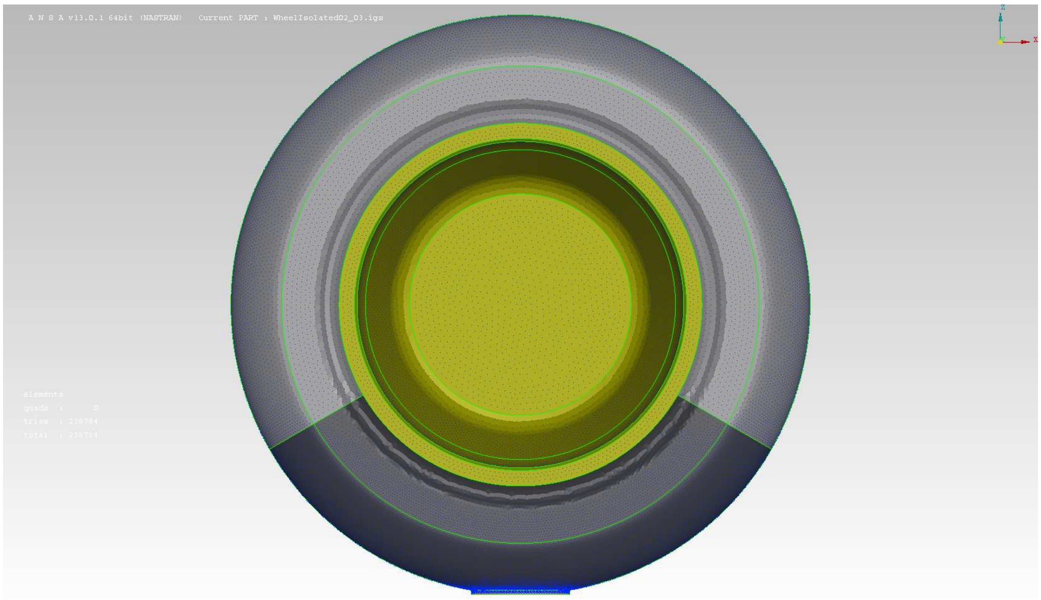
A N S A v13.0.1 64bit (NASTRAN) Current PART : WheelIsolated02_03.igs
Z
X
elements
quads : 0
trias : 238784
total : 238784

Figure 3.6: Split of tyre tread

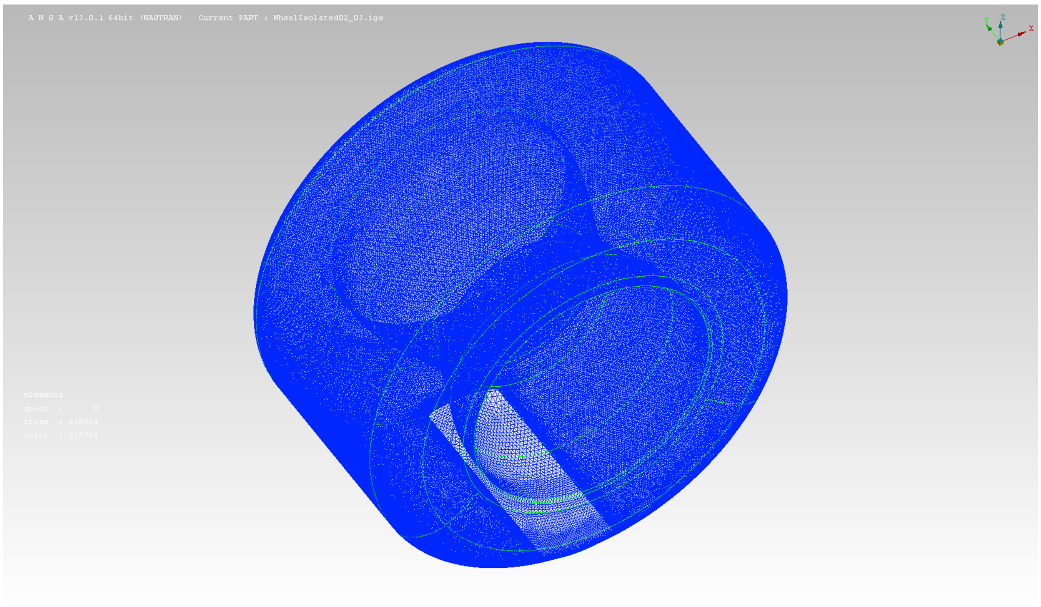

```
A N S A v13.0.1 64bit (NASTRAN)   Current PART : WheelIsolated02_03.igs
```

```
elements
quads  :      0
trias  : 238784
total  : 238784
```

Figure 3.7: Wheel meshed

With regards to the volume mesh, the computational box is divided into different boxes with different limit dimensions in order to control the growing meshes and avoid high residuals. The volume mesh is, as already mentioned, unstructured, and characterized by a thin layer of prisms on the tyre, the contact patch and the ground under an unstructured polyhedral mesh. The use of unstructured mesh is motivated by its widespread use in the industrial flow computation.

The computational domain can be considered as an ensemble of nested boxes: the contact patch, the whole tyre, a box downstream to describe with a high level of detail the wake region and two other boxes whose aim is to smooth the transition between refinement boxes. Before describing the dimensions of the refinement boxes, it’s important to illustrate the coordinate system used for the mesh dimensions, which isn’t the same that has been used for the calculation of the pressure coefficient and the imposition of the angular velocity, seen in Figure 3.2. Figure 3.8 tries to remedy of this inconvenience.

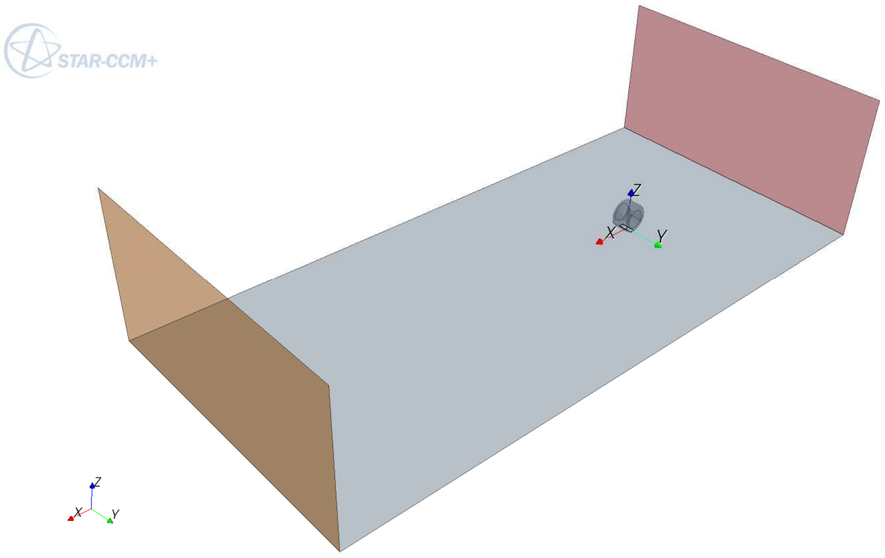

Figure 3.8: Coordinate system used for the refinement boxes

The dimensions of these boxes are:

- for the box named *contact patch*, Figure 3.9, x=±1.2D, y=±0.7D, z=0.25D, with a cell size of *0.005m*;
- for the box named *tyre*, Figure 3.10, x=±2.82D, y=± 4D, z=1.2D with a cell size of *0.008m*;
- for the box named *downstream*, Figure 3.11, x=3.31D, y=±1.5D, z = 1.2D with a cell size of *0.01m*;
- for the box named *CAR*, Figure 3.12, x=2.5D (upstream) 5.5D (downstream), y=±4.3D, z=2.2D with a cell size of *0.02m*;
- for the box named *CAR Big*, Figure 3.13, x=3.5D (upstream) 10.5D (downstream), y=±4.5D, z=2.5D with a cell size of *0.04m*.

Other parameters of the mesh are, concerning the polyhedral part, its growth ratio, set to 1.3; for the prism layer, the stretch factor is set to 1.2, and the thickness of this mesh part is set to 0.01m: the number of prism elements is the parameter the author decided to vary in order to resolve the viscous sub-layer and to use two different wall treatments.

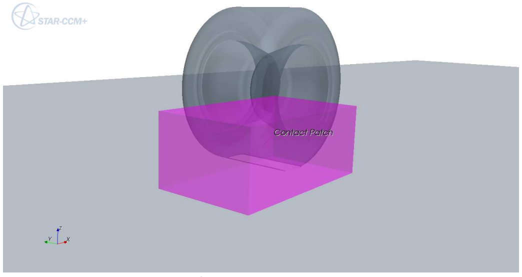
Contact Patch

Figure 3.9: Refinement box: Contact Patch

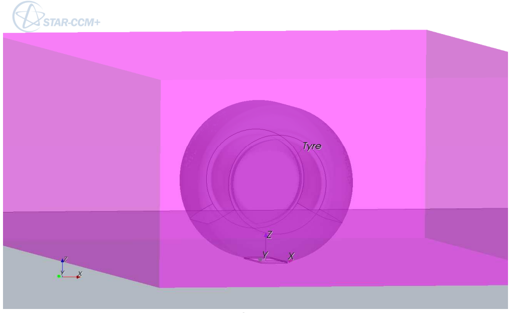

Figure 3.10: Refinement box: Tyre

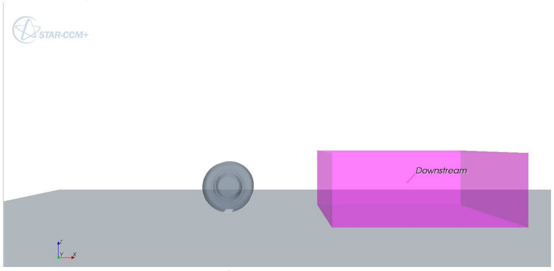
Downstream

Figure 3.11: Refinement box: Downstream

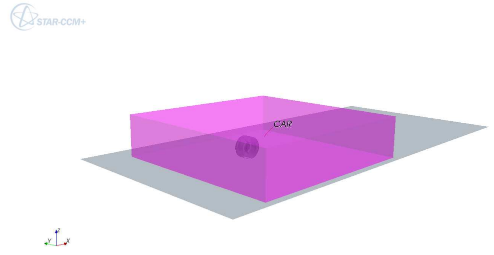

Figure 3.12: Refinement box: CAR

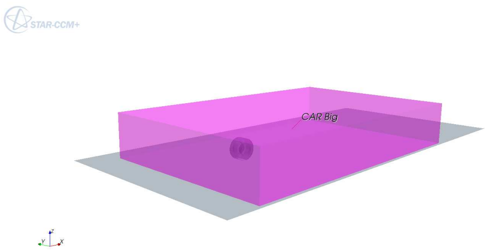

Figure 3.13: Refinement box: CAR Big

To conclude the section, Figure 3.14 and 3.15 show a streamwise view of the mesh and a detailed view of the contact patch.

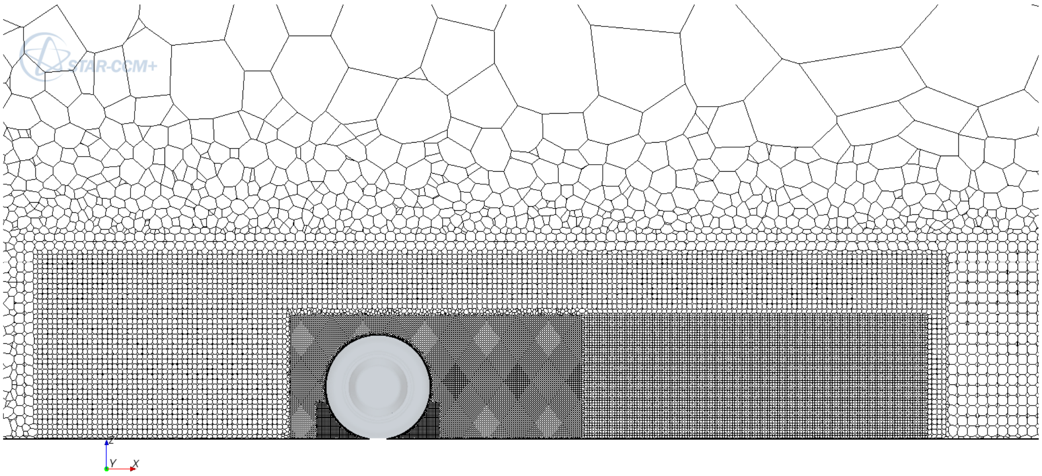

Figure 3.14: Streamwise mesh view

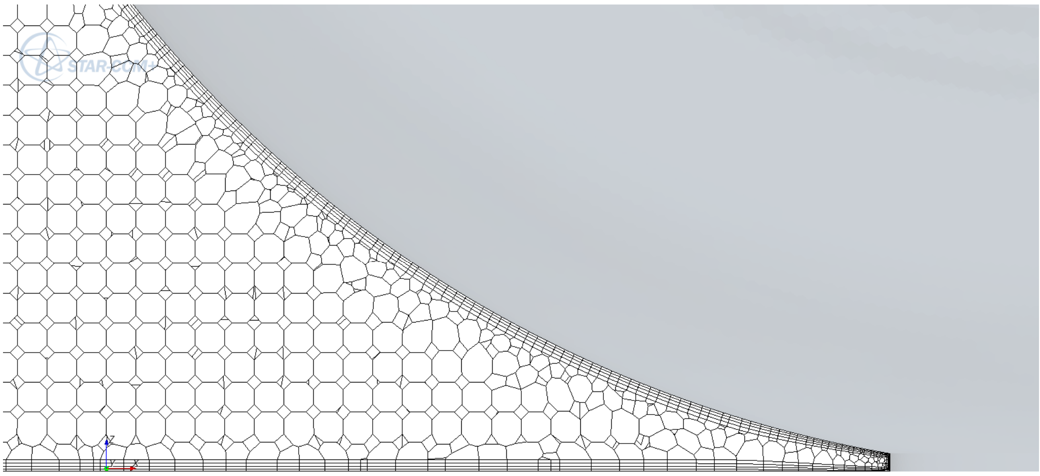

Figure 3.15: Detail of the prism layer on ground, contact patch and tyre.

3.2 Boundary condition and initial value

In order to reproduce faithfully the environmental condition of Fackrell's experiment, at the inflow boundary an uniform x-wise velocity was set, with a value of *18.6m/s*. This speed corresponds to a Reynolds Number, based on the wheel nominal diameter, of $5.3 \cdot 10^5$. Additionally, an imposed level of free turbulence is set to 0.01, very low with a value of turbulent viscosity ratio, i.e.

the ratio between the turbulent viscosity and the physical viscosity, of 10. The outflow boundary was set as a 1-atm pressure outlet; the ground is a moving smooth wall with the same speed of the flow as the inlet, while the ceiling and the lateral boundaries are set as smooth wall with slip condition. Also the contact patch has the same set of the previous boundaries; finally, the boundaries describing the wheel are set as moving smooth wall with an angular velocity equal to *89.63855rad/s*.

Concerning the flow approximation, common feature are: three dimensional, gas (air), segregated, constant density turbulent and moving reference frame. Since the other settings are variable from simulation to simulation, in the following pages they are widely described.

With regards to the steady simulations, the number of iteration has been set to 10000 unities, using the last 3000, to obtain the mean value: the choice of such high value is dictated by the will to capture the details of the difficult domain, and by the necessity to obtain a solution as stable as possible, in order to get reliable mean value.

On the other hand, concerning the unsteady simulation, the values used require a brief explanation, due the complexity of the choice of the settings. Total duration of simulation is of 0.56 s, corresponding to exactly 8 tyre rotations; this value has been chosen in order to get a fully developed flow: the simulation time should be more than a couple of rotation of the tyre. Additionally, it’s important to consider the period of vortex release, described by the Strouhal number, which for the case in exam is of 0.2. This number, together with the diameter of the wheel and the velocity of the flow, leads to a period of 0.1115s, almost two times of revolution period. Using the last consideration, the choice of 8 tyre rotation can be seen as 4 times the period of vortex release.

The physical time illustrated above has a time step of 0.001s: in this way the time is divided into 560 intervals, and for each intervals 20 inner iteration are performed. The averaging process starts at 0.28s, exactly at the middle of the physical time, using the 20th and last value found for each time step.

3.3 Governing equation

This section describes the two type of governing equation. Since in the previous section the turbulence settings have been mentioned, the equation governing the fluid dynamics is, obviously, the incompressible Reynolds Average Navier Stokes one, also known as RANS. In the present work the governing equations are presented using the numerical way, in order to make the reader more confident with the results presented in the next chapter. The aim is to describe the governing equation in the same way as they are implemented in the commercial code, avoiding the theoretical part, which is supposed to be known to the reader (described in [26]).

Considering the subdivision obtained by the mesh, as seen in the previous section, finite volume discretisation applies for each cell, called control volume, a discrete formulation of the integral governing equation, i.e. continuity x,y,z-momentum. The discrete continuity equation is computed as

$$\sum_f \dot{m}_f = \sum_f \left(\dot{m}_f^{\ *} + \dot{m}_f^{\ '} \right) = 0 \qquad (3.1)$$

where $\dot{m}_f^{\ *}$ is the computed mass flow through the interface between the consecutive cell-0 and cell-1, derived from the momentum equation, and $\dot{m}_f^{\ '}$ is the correction, in order not to violate the mass conservation.

The $\underline{v}$-momentum is discretised in the following way

$$\frac{d}{dt}\left(\rho \underline{v} V\right)_0 + \sum_f \underline{v}\rho\left(\underline{v} - \underline{v}_g\right)\cdot \underline{a} = \sum_f \left(p\underline{\underline{I}}\cdot\underline{a}\right)_f + \sum_f \underline{\underline{T}}\cdot\underline{a} \qquad (3.2)$$

where ρ is the fluid density, $\underline{v}$ is the velocity vector, V is the volume of the cell-0, $\underline{v}_g$ is grid velocity, $\underline{a}$ is the face area vector, p is the pressure value in the flow field, $\underline{\underline{I}}$ is the identity matrix and $\underline{\underline{T}}$ is the viscous stress tensor

Equation 3.2 contains, from the left to the right, the following terms: transient, convective, diffusive and volumetric source. In the following paragraphs, each term of this equation is illustrated, and the numerical scheme applied during the simulation will be described.

Transient term This term appears only in the unsteady simulation (URANS), and in this work a second order differentiation scheme is used. Considering the equation 3.2, the first time-dependent terms are calculated in the following way.

$$\frac{d}{dt}\left(\rho \underline{v} V\right)_0 = \frac{\left(\rho_0 \underline{v}_0\right)^{n+1} - 4\left(\rho_0 \underline{v}_0\right)^{n} + \left(\rho_0 \underline{v}_0\right)^{n-1}}{\Delta t} V_0$$

the transient term is therefore a weighted sum of the values picked from three different time steps. This method is not applicable for the first time step, for which the first order derivative described here is used:

$$\frac{d}{dt}\left(\rho \underline{v} V\right)_0 = \frac{\left(\rho_0 \underline{v}_0\right)^{n+1} - \left(\rho_0 \underline{v}_0\right)^{n}}{\Delta t} V_0$$

Convective term With regards to the convective term, the finite volume discretisation transforms the terms in

$$\sum_f \underline{v}\rho\left(\underline{v}-\underline{v}_g\right)\cdot \underline{a} = \left(\dot{m}\underline{v}\right)_f = \left(\dot{m}_f\,\underline{v}_f\right) \tag{3.3}$$

the second order upwind scheme has been used:

$$\left(\dot{m}_f\,\underline{v}_f\right)=\begin{cases}\dot{m}_f\,\underline{v}_{f0}\;\dot{m}_f>0\\ \dot{m}_f\,\underline{v}_{f1}\;\dot{m}_f<0\end{cases}$$

where the face value of the velocity vector $\underline{v}_{f0}$ and $\underline{v}_{f1}$ are linearly interpolated from cell values from either side of the face as explained hereby

$$\underline{v}_{f0}=\underline{v}_0+\underline{s}_0\cdot\left(\nabla\underline{v}\right)_{r,0}$$
$$\underline{v}_{f1}=\underline{v}_1+\underline{s}_1\cdot\left(\nabla\underline{v}\right)_{r,1}$$

$\left(\nabla\underline{v}\right)_{r,0}$ and $\left(\nabla\underline{v}\right)_{r,1}$ are the limited reconstruction gradients in cell 0 and 1 respectively. while

$$\underline{s}_0=\underline{x}_f-\underline{x}_0$$
$$\underline{s}_1=\underline{x}_f-\underline{x}_1$$

and $\underline{x}_f,\underline{x}_0,\underline{x}_1$ are the face and the cell centroids.

As said before, this type of scheme is second order accurate; however, the use of limited reconstruction gradient helps to reduce local extremes and thus introduce more dissipation with respect to a central differencing scheme. The downside is, since this is always a second-order accurate scheme, that the reduced numerical dissipation might be result, in some conditions, in a poorer convergence compared to a first order scheme.

The reconstruction velocity gradient $\left(\nabla\underline{v}\right)_{r,0-1}$ is limited because the value of reconstruction face velocity $\underline{v}_{f0-1}$ shouldn't exceed neither the maximum nor the minimum of the cell centroid value, including cell-0 value. The parameter α is a scale factor expressing the ratio between the limited and the unlimited value

$$\alpha=\frac{\left(\nabla\underline{v}\right)_{r,1}}{\left(\nabla\underline{v}\right)^{u}{}_{r,0}}$$

The value of $(\nabla \underline{v})^{u}{}_{r,0}$, is computed using the Gauss' divergence theorem, which in discrete form becomes

$$(\nabla \underline{v})^{u}{}_{r,0} = \frac{1}{V_0} \sum_f \underline{v}_f \underline{a}_f$$

and the velocity vector on the face is calculated as the arithmetical mean of the two adjacent vectors

$$\underline{v}_f = \frac{\underline{v}_0 + \underline{v}_1}{2}$$

Regarding α, for each cell-0 the following quantities are defined

$$\underline{v}^{\max}{}_0 = \max\left(\underline{v}_0, \underline{v}_{neighbors}\right)$$
$$\underline{v}^{\min}{}_0 = \min\left(\underline{v}_0, \underline{v}_{neighbors}\right)$$

where $\underline{v}_{neighbors}$ represent the velocity vector of each cell that has a common face with cell-0. Manipulating the previous definition yields

$$\Delta_{\max} = \underline{v}^{\max}{}_0 - \underline{v}_0$$
$$\Delta_{\min} = \underline{v}^{\min}{}_0 - \underline{v}_0$$

For each face *f* of the cell-0 the following quantity is defined

$$\Delta_f = \underline{v}_{f,0} - \underline{v}_0 = \underline{s}_0 (\nabla \underline{v})^{u}{}_{r,0}$$

and

$$r_f = \begin{cases} \dfrac{\Delta_f}{\Delta_{\max}} if \Delta_f > 0 \\ \dfrac{\Delta_f}{\Delta_{\min}} if \Delta_f \le 0 \end{cases}$$

For each face, α_f is

$$\alpha_f = \frac{2r_f + 1}{r_f (2r_f + 1) + 1}$$

finally, for each cell α is

$$\alpha = \min(\alpha_f)$$

Diffusive term The pressure term is written using a suitable scheme, which secures a second order accuracy. In Figure 3.16 a scheme useful to understand the numerical scheme in equation 3.4 is illustrated

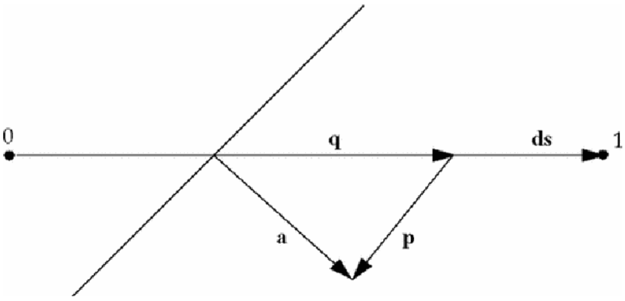

Figure 3.16: Diffusive term.

$$\Gamma_f \left[(p_1 - p_0)\vec{\alpha} \cdot \underline{a} + \overline{\nabla p} \cdot \underline{a} - \left(\overline{\nabla p} \cdot ds \right) \vec{\alpha} \cdot \underline{a} \right] \tag{3.4}$$

with

$$\vec{\alpha} = \frac{\underline{a}}{\underline{a} \cdot ds}$$

$$ds = \underline{x}_1 - \underline{x}_0$$

$$\overline{\nabla p} = \frac{(\nabla p_0 + \nabla p_1)}{2}$$

The second and the third term in the equation 3.4 represent the secondary, or cross-diffusion, contribution. These are of vital importance for unstructured meshes as the ones used in this work.

Viscous flux In turbulent flows, the stress tensor is divided into two parts: the laminar one and the turbulent one.

$$T = T_l + T_t$$

where

$$T_l = \mu \left[\nabla \underline{v} + \nabla \underline{v}^T - \frac{2}{3} (\nabla \cdot \underline{v}) I \right]$$

and T_t is called Reynolds stress tensor. Unless Reynolds stress models (RSM) are used, Boussinesq approximation is applied.

$$T = \mu_{eff} \left[\nabla \underline{v} + \nabla \underline{v}^T - \frac{2}{3} (\nabla \cdot \underline{v}) I \right]$$

and

$$\mu_{eff} = \mu + \mu_{visc}$$

The determination of the eddy viscosity, or turbulent viscosity is the subject of the following section.

To evaluate the stress tensor T in the interior cells, the velocity tensor gradient at the face should be written in term of cell velocity:

$$\nabla v_f = \left[(v_1 - v_0) \otimes \vec{\alpha} + \overline{\nabla v_f} - \left(\overline{\nabla v_f} \cdot ds \right) \otimes \vec{\alpha} \right]$$

and $\overline{\nabla v_f} = \frac{(\nabla v_0 + \nabla v_1)}{2}$, where $\nabla v_{0,1}$ are explicitly computed velocity gradient tensor in the cell.

Concerning boundary faces, it depends if they are defined as slip or no slip walls. If a slip condition is set, the viscous shear force is simply set to zero.

For no-slip walls, it is assumed that only the component of the velocity parallel to the wall is of interest. A linear relationship between the wall shear force and the wall-parallel component of the velocity difference between the wall and the cell is assumed.

$$(T \cdot \underline{a})_f = -\gamma (v^t - v_f^t)$$

Using the definition of wall shear stress magnitude $\tau_w = \rho u^{*2}$ and the reference velocity $u^+ = |v_p| / u^*$, γ, the coefficient of proportionality is

$$\gamma = |\underline{a}| \frac{\rho u^*}{u^+}$$

the reference velocity, u^*, is computed according to the specific turbulence model. The value of u^+ is obtained, as function of y^+, from the wall law used.

3.4 Wall treatment

In this section, the two type of wall law used are described. A wall law is the way the CFD code uses to determine some quantities as mean velocity, pressure and so on in turbulent boundary layer. There are many regions where it is necessary to resolve the viscous-affected region, especially the region which surrounds the wheel. The laminar and turbulent profile is blended smoothly in a buffer layer and this type of behaviour isn’t controlled by the user, but the way the turbulent boundary layer is resolved depends, not exclusively, on the quality of the mesh, and how fine it is in the closest part of the wall (i.e. the prism layer).

The two type of wall treatments used are the *all y+* and the *low y+* wall treatment. The first method, *all y+*, provide itself to determine if the wall y+ value, namely the value of the first mesh cell above the wall boundary in wall unit, and determines in which zone of the boundary layer the cell are situated and calculates the velocity value therefore. The *all y+* wall treatment is peculiar in the determination of the reference velocity u^* and its first derivatives: the calculation is done not by using the proper definition $u^* = \sqrt{\tau_w / \rho}$, but a computed formulation depending from $y \approx \sqrt{\upsilon u / y}$.

The latter, *low y+*, makes no modelling assumption, so the wall y+ value must be less than 1, in order to have reliable results.

3.5 Turbulence suppression

Using this type of tool, the CFD code calculates the transition distance and tries to mimic the effect of the transition by suppressing the turbulence in a pre-defined region.

The turbulence suppression can be achieved in different ways, such as setting to zero either the turbulence viscosity, the Reynolds stressed or the production terms in the turbulence transport equation; another kind of way might be to avoid using the wall function to compute the wall shear stress, but using the laminar method instead.

The region in the flow field in which the turbulence is suppressed is defined as any point in the field where the transition boundary distance, i.e. the distance between the field point and the nearest point in the transition boundary, is less than the wall distance, defined as the distance between the same field point and a wall which isn’t a transition boundary.

3.6 Convergence criteria

The way to get acceptable results requires the updating of the solution. The solution of a general transported scalar in the cell-p ϕ_p at the next iteration should be updated as

$$a_p \phi_p^{k+1} + \sum_{neighbour} a_n \phi_n^{k+1} = b$$

where b is explicit, i.e. evaluated with the result of from the iteration k, contribution to the discretised equation, and ϕ_n are the same scalar transported function calculated in the neighbour cells, and a_p a_n are obtained directly from the discretised term. This type of upgrading may lead to a diverging solution; due to the complex flow structures that are being predicted in literature, it is necessary to introduce another type of solution update. Under-Relaxation factor are employed in order to make the updating more gradual, especially in the first iterations

$$\frac{a_p}{\varpi}\phi_p^{k+1}+\sum_{neighbour}a_n\phi_n^{k+1}=b+\frac{a_p}{\varpi}\phi_p^k(1-\varpi)$$

therefore in the right-hand side a source value is present, evaluated at the previous iteration. Regarding ϖ, the relaxation factor, its value depends on the transport equation discretized; its value is set to 0.4 for the momentum equation, while for the pressure it is set to 0.2. For the other transport equations that close the budget unknowns-equations, the relaxation factor is described in the section regarding the turbulence model.

To monitor the convergence of the solution, for each transport equation and at each iteration the residual is computed. This value is defined as the degree to which the discretized equation is not completely satisfied in each cell; in a perfectly converged solution, the residual for each cell would be equal to the machine round-off.

For each iteration and for each transport equation, the residual value is determined as

$$\sqrt{\frac{\sum_{n_{cells}} r^2}{n_{cells}}}$$

where the value r is computed as, recalling the previous equation,

$$r=b-a_p\phi_p^{k+1}-\sum_{neighbour}a_n\phi_n^{k+1}$$

It is worth to note that this value is weighted using the residual value of the first iteration, obviously higher than the next if the simulation goes towards convergence. Given the complexity of the simulation, and the low capacity of dissipation of the commercial code, residual values around 10^{-3} are considered as acceptable.

3.7 Turbulence model

The aim of this section is to describe the key feature of all the turbulence models investigated in this work. For each turbulence model, the wall function scheme used is illustrated. The turbulence models used are the most common in an industrial environment.

3.7.1 K-ε

A K-ε turbulence model is a two-equation model in which transport equations are solved for the turbulent kinetic energy K and its dissipation rate ε. Various forms of the K- ε model have been in use for several decades, and it has become the most widely used model for industrial applications. Since the inception of the K- ε model, there have been countless attempts to improve it.

In this work, two types of K- ε models are used: the realizable two-layer and the Standard Low Reynolds Number. The first is the one widely used because of its extreme flexibility; transport equations are

$$\frac{d}{dt}\int_V \rho k\,dV + \int_A \rho k(\mathbf{v}-\mathbf{v}_g)\cdot d\mathbf{a} =$$

$$\int_A \left(\mu + \frac{\mu_t}{\sigma_k}\right)\nabla k \cdot d\mathbf{a} + \int_V [G_k + G_b - \rho((\varepsilon-\varepsilon_0)+\Upsilon_M) + S_k]\,dV$$

$$\frac{d}{dt}\int_V \rho\varepsilon\,dV + \int_A \rho\varepsilon(\mathbf{v}-\mathbf{v}_g)\cdot d\mathbf{a} =$$

$$\int_A \left(\mu + \frac{\mu_t}{\sigma_\varepsilon}\right)\nabla\varepsilon \cdot d\mathbf{a} + \int_V \left[C_{\varepsilon 1} S\varepsilon + \frac{\varepsilon}{k}(C_{\varepsilon 1}C_{\varepsilon 3}G_b - C_{\varepsilon 2}\rho(\varepsilon-\varepsilon_0)) + S_\varepsilon\right] dV$$

where S_k and S_ε are user specified source and ε_0 is the ambient turbulence value in source terms that counteracts turbulence decay. The production term G_k is determined as with the standard K- ε model:

$$G_k = \mu_t S^2 - \frac{2}{3}\rho k \nabla\cdot\underline{v} - \frac{2}{3}\mu_t(\nabla\cdot\underline{v})^2$$

where $\nabla \cdot \underline{v}$ is the velocity divergence and is the modulus of the mean strain rate tensor:

$$S = \left|\underline{\underline{S}}\right| = \sqrt{2\underline{\underline{S}} : \underline{\underline{S^T}}} = \sqrt{2\underline{\underline{S}} : \underline{\underline{S}}}$$

and

$$S = \frac{1}{2}\left(\nabla \underline{v} + \nabla \underline{v^T}\right)$$

and the relation of the turbulent viscosity is computed as

$$\mu_t = \rho C_\mu \frac{k^2}{\varepsilon}$$

where the coefficient C_μ is not constant, as with the standard K-ε model, but is instead given by:

$$C_\mu = \frac{1}{A_0 + A_S U^{(*)} \frac{k}{\varepsilon}}$$

where

$$U^{(*)} = \sqrt{\underline{\underline{S}} : \underline{\underline{S}} - \underline{\underline{W}} : \underline{\underline{W}}}$$

with **S** strain rate tensor and **W** rotation rate tensor. Other coefficients are

$$A_S = \sqrt{6}\cos\phi$$

$$\phi = a\cos\left(\sqrt{6}W\right)$$

$$W = \frac{S_{ij}S_{jk}S_{ki}}{\left(\sqrt{2}S\right)^3}$$

$$A_0 = 4.0$$

$$C_{\varepsilon 1} = \max\left(0.43, \frac{\eta}{5+\eta}\right)$$

where

$$\eta = \frac{Sk}{\varepsilon}$$

Finally,

$$C_{\varepsilon 2} = 1.9, \qquad \sigma_k = 1.0 \ , \qquad \sigma_\varepsilon = 1.2$$

The two-layer model blends a one-equation model, which solves for K but prescribes algebraically ε with distance from the wall, with the two-equation K- ε model. The two-layer model is parameterized as a length scale function, $l_\varepsilon = f\left(y, \mathrm{Re}_y\right)$ and turbulent viscosity ratio function $\mu_t / \mu = f\left(\mathrm{Re}_y\right)$ where $\mathrm{Re}_y = \frac{\sqrt{k}\,y}{\nu}$. The dissipation rate computed from the two-layer formulation is

$$\varepsilon = \frac{k^{3/2}}{l_\varepsilon}$$

using the following blending function

$$\lambda = \frac{1}{2}\left[1 + \tanh\left(\frac{\mathrm{Re}_y - \mathrm{Re}_y^*}{A}\right)\right]$$

where Re_y^* defines the limit of applicability of two-layer formulation, which in the present work is set to 60. The constant *A* determines the width of the blending function. By defining a width such that the value of λ will be within 1% of its far-field value for a given variation of $\Delta \mathrm{Re}_y$, the following relation between *A* and $\Delta \mathrm{Re}_y$ can be obtained

$$A = \frac{\left|\Delta \mathrm{Re}_y\right|}{\tanh 0.98}$$

where $\Delta \mathrm{Re}_y$ is set to 60.

The turbulent viscosity is blended with the two-layer formulation in this way

$$\mu_t = \lambda \mu_t\big|_{k-\varepsilon} + (1-\lambda)\mu\left(\frac{\mu_t}{\mu}\right)_{two-layer}$$

Since cell values of ε may be specified by setting the coefficients of the solution matrix to satisfy

$$\frac{a_p}{\varpi}\Delta\varepsilon_p = a_p\left(\varepsilon_p^{n+1}\Big|_{spec} - \varepsilon_p^n\right)$$

the discretized transport equation for ε may be combined with this to obtain:

$$\frac{a_p}{\omega}\Delta\varepsilon_p + \sum_n a_n \lambda \Delta\varepsilon_n =$$

$$\lambda\left(b - a_p\varepsilon_p^n - \sum a_n\varepsilon_n^n\right) + (1-\lambda)a_p(\varepsilon_p^{n+1}\Big|_{2\text{layer}} - \varepsilon_p^n)$$

Regarding the standard K-ε model, the transport equations are

$$\frac{d}{dt}\int_V \rho k dV + \int_A \rho k(\mathbf{v}-\mathbf{v}_g)\cdot d\mathbf{a} =$$

$$\int_A \left(\mu + \frac{\mu_t}{\sigma_k}\right)\nabla k \cdot d\mathbf{a} + \int_V [G_k + G_b - \rho((\varepsilon - \varepsilon_0) + \Upsilon_M) + S_k]dV$$

$$\frac{d}{dt}\int_V \rho\varepsilon dV + \int_A \rho\varepsilon(\mathbf{v}-\mathbf{v}_g)\cdot d\mathbf{a} =$$

$$\int_A \left(\mu + \frac{\mu_t}{\sigma_\varepsilon}\right)\nabla\varepsilon \cdot d\mathbf{a} \; +$$

$$\int_V \frac{1}{T}[C_{\varepsilon 1}(G_k + G_{nl} + G' + C_{\varepsilon 3}G_b) - C_{\varepsilon 2}f_2\rho(\varepsilon - \varepsilon_0) + \rho\Upsilon_y + S_\varepsilon]\, dV$$

where S_k and S_ε are user specified source and ε_0 is the ambient turbulence value in source terms that counteracts turbulence decay. G’ is an additional production term, calculated as

$$G' = Df_2\left(G_k + 2\mu\frac{k}{y^2}\right)\exp\left(-0.00375\,\text{Re}_y^2\right)$$

where f_2 is defined as

$$f_2 = 1 - 0.3\exp\left(\mathrm{Re}_T^2\right)$$

with $\mathrm{Re}_y = \frac{\sqrt{k}y}{\nu}$ and $\mathrm{Re}_T = \frac{k^2}{\varepsilon\nu}$

In the original model, the value of D is given by $D = {C_{\varepsilon 2}}/{C_{\varepsilon 1}} \approx 1.3$. However, DNS data for low-Reynolds number channel flow suggests that better results are obtained with *D* = 1; for this reason, it is set as default value.

Regarding the turbulent production, this is computed as illustrated above for the realizable scheme, and for this reason it isn't repeated anymore.

The turbulent viscosity is calculated as

$$\mu_t = \rho C_\mu f_\mu k T$$

where *T* is the turbulent timescale computes as follows

$$T = \max\left(\frac{k}{\varepsilon}, C_t\sqrt{\frac{\nu}{\varepsilon}}\right)$$

while f_μ is a damping function computed as

$$f_\mu = 1 - \exp\left[-\left(C_{d0}\sqrt{\mathrm{Re}_y} + C_{d1}\mathrm{Re}_y + C_{d2}\mathrm{Re}_y^2\right)\right]$$

and the values of the coefficient are $C_{d0} = 0.091$, $C_{d1} = 0.0042$ $C_{d2} = 0.00011$

It is important to note that, although the equation used for the blending function isn't the same used in the original scheme, its asymptotical behaviour for $\mathrm{Re}_y \to 0$ remains the same.

3.7.2 K-ω SST

The K- ω model is a two-equation model alternative to the K- ε model. The transport equations solved are for the turbulent kinetic energy K and a quantity called ω, which is defined as the specific dissipation rate, that is, the dissipation rate per unit turbulent kinetic energy ω ~ ε/K. Wilcox [30], its creator widely explains the superiority of the ω transport equation, for instance its improved performance for boundary layers under adverse pressure gradients. Perhaps the most significant advantage, however, is that it may be applied throughout the boundary layer, including the viscous-dominated region, without further modification.

The biggest disadvantage of the K- ω model, in its original form, is that boundary layer computations are very sensitive to the values of ω in the free stream. This can be translated into extreme sensitivity to inlet boundary conditions for internal flows, a problem that does not exist for the K- ε models.

The problem of sensitivity to free-stream/inlet conditions was addressed by Menter [31], who recognized the transport equation from the standard K-ε model could be transformed into a ω transport equation by a variable substitution. The transformed equation looks very similar to the one in the standard K- ω model, but adds an additional non-conservative cross-diffusion term containing the dot product $\nabla k \cdot \nabla \varpi$. Inclusion of this term in the transport equation will potentially make the K- ω model give identical results to the K- ε model. Menter suggested using a blending function (which includes functions of wall distance) that would include the cross-diffusion term far from walls, but not near the wall. This approach effectively blends a K- ε model in the far-field with a K-ω model near the wall. Purists may object that the blending function crossover location is arbitrary, and could obscure some critical feature of the turbulence. Nevertheless, the fact remains that this approach cures the biggest drawback to applying the K- ω model to practical flow simulations.

In addition, Menter also introduced a modification to the linear constitutive equation and dubbed the model containing this modification the SST (shear-stress transport) K-ω model. The SST model has seen fairly wide application in the aerospace industry, where viscous flows are typically well resolved and turbulence models are generally applied throughout the boundary layer.

The two transport equations are

$$\frac{d}{dt}\int_V \rho k\, dV + \int_A \rho k(\mathbf{v}-\mathbf{v}_g)\cdot d\mathbf{a} =$$

$$\int_A (\mu + \sigma_k \mu_t)\nabla k \cdot d\mathbf{a} + \int_V (\gamma_{eff} G_k - \gamma' \rho \beta^* f_\beta(\omega k - \omega_0 k_0) + S_k)\, dV$$

$$\frac{d}{dt}\int_V \rho \omega\, dV + \int_A \rho \omega(\mathbf{v}-\mathbf{v}_g)\cdot d\mathbf{a} =$$

$$\int_A (\mu + \sigma_\omega \mu_t)\nabla \omega \cdot d\mathbf{a} + \int_V (G_\omega - \rho \beta f_\beta(\omega^2 - \omega_0^2) + D_\omega + S_\omega)\, dV$$

where S_k and S_ω are the user-specified source terms, k_0 and ω_0 are the ambient turbulence values in source terms that counteract turbulence decay, γ_{eff} is the effective intermittency that in this case is set to 1 and:

$$\gamma' = \min[\max(\gamma_{eff}, 0.1), 1]$$

The production G_k is evaluated as with the standard K- ω model

$$G_k = \mu_t S^2 - \frac{2}{3}\rho k \nabla \cdot \underline{v} - \frac{2}{3}\mu_t (\nabla \cdot \underline{v})^2$$

where $\nabla \cdot \underline{v}$ is the velocity divergence and is the modulus of the mean strain rate tensor:

$$S = \left|\underline{\underline{S}}\right| = \sqrt{2\underline{\underline{S}} : \underline{\underline{S}}^T} = \sqrt{2\underline{\underline{S}} : \underline{\underline{S}}}$$

and

$$S = \frac{1}{2}\left(\nabla \underline{v} + \nabla \underline{v}^T\right)$$

The production of ω G_ω is evaluated as

$$G_\omega = \rho\gamma\left[\left(S^2 - \frac{2}{3}(\nabla \cdot \mathbf{v})^2\right) - \frac{2}{3}\omega\nabla \cdot \mathbf{v}\right]$$

and γ is a blended coefficient of the model.

The term D_ω is a cross-derivative term, defined as

$$D_\omega = 2(1 - F_1)\rho\sigma_{\varpi 2}\frac{1}{\omega}\nabla k \cdot \nabla\omega$$

And the turbulent viscosity is computed as

$$\mu_t = \rho k T$$

where the time scale is computed using Durbin’s realizability constraint [32] as:

$$T = \min\left(\frac{1}{\max(\omega/\alpha^*, (SF_2)/a_1)}, \frac{0.6}{\sqrt{3}S}\right)$$

and is the modulus of the mean strain rate tensor defined above. Note that in Menter’s original model, the modulus of the vorticity tensor was used in the definition of the turbulent viscosity for the SST. This slight modification extends the applicability of the model beyond aerodynamic applications.

Furthermore, Durbin's realizability constraint is used instead of Menter's proposal that turbulent production be limited to some multiple of the dissipation. The function F_2 is given by

$$F_2 = \tanh(\mathrm{arg}_2{}^2)$$

where

$$\mathrm{arg}_2 = \max\left(\frac{2\sqrt{k}}{0.09\,\omega y}, \frac{500\nu}{y\omega}\right)$$

and a_1 is set to 0.31.

3.7.3 Spalart Allmaras

This turbulence model [33] is the only one-equation model used and presented in this work, and the reason has to seek in the less computational efforts in order to get an acceptable accuracy. Several works investigating tyre wake behaviour used this model, for instance [25]; for this reason, the author das decided to include in the investigation.

Operatively, Spalart-Allmaras turbulence model solves a single transport equation that determines the turbulent viscosity. This is in contrast to many of the early one-equation models that solve an equation for the transport of turbulent kinetic energy and required an algebraic prescription of a lengthscale.

In its own standard form, the Spalart-Allmaras model is a low-Reynolds number model, meaning it is designed to be applied without wall functions. According to the model's formulation, the entire turbulent boundary layer, including the viscous sublayer, ought to be accurately resolved so it can be applied on fine meshes, i.e. small values of y+.

The wall law used is the low y+, which implements the model and boundary conditions in low-Reynolds number form as suggested by Spalart and Allmaras. Damping functions are used for the source terms in the transport equation, which is solved without modification all the way to the wall cell. Wall laws are not used to evaluate shear stress. Spalart and Allmaras devised the model such u*=ν/ƙd that would remain constant throughout the viscous sublayer as well as in the log region.

The transport equation for the Spalart-Allmaras model is:

$$\frac{d}{dt}\int_V \rho\tilde{\nu}\,dV + \int_A \rho\tilde{\nu}(\mathbf{v}-\mathbf{v}_g)\cdot d\mathbf{a} =$$

$$\frac{1}{\sigma_{\tilde{\nu}}}\int_A (\mu+\rho\tilde{\nu})\nabla\tilde{\nu}\cdot d\mathbf{a} + \int_V [C_{b2}\rho(\nabla\tilde{\nu}\cdot\nabla\tilde{\nu}) + G_{\tilde{\nu}} - \Upsilon_{\tilde{\nu}} + S_{\tilde{\nu}}]\;dV$$

Where $S_{\tilde{\upsilon}}$ is the user specified source term and the transported variable is a modified eddy viscosity. The terms on the right-hand side represent diffusion, production and dissipation.

The first term inside the last integral of the above equation is a non-conservative diffusion term that can lead to convergence problems if it is discretised as an explicit source term. Therefore, following the recommendations of Spalart and Allmaras, it is rewritten and combined with the conservative diffusion term as follows

$$\frac{1}{\sigma_{\tilde{\nu}}}\int_A (\mu+\rho\tilde{\nu})\nabla\tilde{\nu}\cdot d\mathbf{a} + \int_V C_{b2}\rho(\nabla\tilde{\nu}\cdot\nabla\tilde{\nu})\;dV \approx$$

$$\frac{1+C_{b2}}{\sigma_{\tilde{\nu}}}\int_A (\mu+\rho\tilde{\nu})\nabla\tilde{\nu}\cdot d\mathbf{a} \;-\frac{C_{b2}}{\sigma_{\tilde{\nu}}}\int_V (\mu+\rho\tilde{\nu})\nabla\tilde{\nu}^{2}dV$$

The production term is modelled as:

$$G_{\tilde{\nu}} = (1-f_{t2})\;C_{b1}\rho\tilde{S}\tilde{\nu}$$

where C_{b1} is a constant.

The function f_{t2} is given by

$$f_{t2} = 1 - \frac{\chi}{1+\chi f_{v1}}$$

while the deformation parameter is

$$\tilde{S} = f_{v3} S + \frac{\nu}{\kappa^2 \tilde{d}^2} f_{v2}$$

where k is Von Karman constant, d is the distance to the nearest wall, and a damping function is

$$f_{v2} = 1 - \frac{\chi}{1 + \chi f_{v1}}$$

and the other one is set to 1. The additional damping function f_{v1} is calculated as:

$$f_{v1} = \frac{\chi^3}{\chi^3 + C_{v1}^3}$$

and $\chi=\nu/\nu$. In the determination of the scalar deformation, Dacles-Mariani *et al.* [34] suggestion is used, which combines the strain rate and vorticity tensor magnitudes as follows:

$$S = |\mathbf{W}| + C_{\mathrm{prod}} \min\,[0, |\mathbf{S}| - |\mathbf{W}|]$$

where

$$|\mathbf{S}| = \sqrt{2\mathbf{S}:\mathbf{S}^T} = \sqrt{2\mathbf{S}:\mathbf{S}}$$

$$\mathbf{S} = \frac{1}{2}(\nabla\mathbf{v} + \nabla\mathbf{v}^T)$$

and the coefficient $C_{prod} = 2$. The dissipation term is modelled as

$$Y_{\tilde{\nu}} = C_{w1}\rho f_w\left(\frac{\tilde{\nu}}{d}\right)^2$$

where

$$f_w = g\left(\frac{1+C_{w3}^6}{g^6+C_{w3}^6}\right)^{1/6}$$

$$g = r + C_{w2}(r^6 - r)$$

$$r \equiv \frac{\tilde{\nu}}{\tilde{S}\kappa^2 \tilde{d}^2}$$

So the turbulent viscosity μ_t is computed as

$$\mu_t = \rho\nu f_{v1}$$

3.7.4 RSM: Reynolds stress model

Reynolds stress transport (RST) models, also known as second-moment closure models, are the most complex turbulence models. By solving transport equations for all components of the specific Reynolds stress tensor, **T**, these models naturally account for effects such as anisotropy due to strong swirling motion, streamline curvature, rapid changes in strain rate and secondary flows in ducts. The RST model carries significant computational overhead. Seven additional equations must be solved in three dimensions (as opposed to the two equations of a K-ε model). Apart from the additional memory and computational time required for these equations to be solved, there is also likely to be a penalty in the total number of iterations required to obtain a converged solution due to the numerical stiffness of the RST equations. The reasons that the RST model requires the solution of seven equations in three dimensions are as follows. The Reynolds stress tensor is symmetric, so that only six of the nine components are unique. In addition to the six RST equations, a model equation is also needed for the isotropic turbulent dissipation. This is the same equation as the one used in the Standard K- ε model.

The starting point for the development of RST models is generally the exact differential transport equation for the Reynolds stresses, which is derived by multiplying the instantaneous Navier-Stokes equations by a fluctuating property and Reynolds-averaging the product. In the resulting equations, only the transient, convective and molecular diffusion terms require no modelling. The terms remaining to be modelled are the diffusion term, the dissipation term and, perhaps the greatest challenge, the pressure-strain term. Appropriate models for these terms have received much attention during the past few decades. The type of Reynolds stress model used in this work is linear pressure strain Two-layer.

The advantage of the linear pressure-strain model is that it lends itself to being incorporated into a two-layer formulation which can be used to resolve the viscous sublayer for low-Reynolds number type applications. In this model's approach, suggested by Rodi [35], the computation is divided into two layers. In the layer adjacent to the wall, the turbulent dissipation rate and the turbulent viscosity μ_t are specified as functions of wall distance. The values of ε specified in the near-wall layer are blended smoothly with the values computed from solving the transport equation far from the wall.

The transport equation for the specific Reynolds stress tensor, **R**=v'v' is

$$\frac{d}{dt}\int_V \rho\mathbf{R}\,dV + \int_A \rho\mathbf{R}(\mathbf{v}-\mathbf{v}_g)\cdot d\mathbf{a} =$$

$$\int_A \mathbf{D}\cdot d\mathbf{a} + \int_V \left[\mathbf{P}+\mathbf{G}-\frac{2}{3}\rho\mathbf{I}(\varepsilon+\Upsilon_M)+\underline{\Phi}+\mathbf{S}_{\mathbf{R}}\right]dV$$

where the terms on the right-hand side are diffusion, turbulent production, buoyancy production, turbulent dissipation, dilatation dissipation, pressure strain and user-specified source.

A simple isotropic form of the turbulent diffusion is adopted, such that:

$$\mathbf{D} = \left(\mu + \frac{\mu_t}{\sigma_k}\right)\nabla\mathbf{R}$$

where the turbulent Schmidt number is $\sigma_k = 0.82$ and the turbulent viscosity is computed as:

$$\mu_t = \rho C_\mu \frac{k^2}{\varepsilon}$$

and the turbulent kinetic energy is computed as the half trace of the tensor **R**. As concern the turbulence production, it is obtained without recourse to model as follows:

$$\mathbf{P} = -\rho(\mathbf{R} \cdot \nabla \mathbf{v}^T + \nabla \mathbf{v} \cdot \mathbf{R}^T) = -\rho(\mathbf{R} \cdot \nabla \mathbf{v}^T + \nabla \mathbf{v} \cdot \mathbf{R})$$

The isotropic turbulent dissipation rate is obtained from a transport equation analogous to the K-ε model (and with identical boundary conditions):

$$\frac{d}{dt}\int_V \rho\varepsilon dV + \int_A \rho\varepsilon(\mathbf{v}-\mathbf{v}_g) \cdot d\mathbf{a} =$$

$$\int_A \left(\mu + \frac{\mu_t}{\sigma_\varepsilon}\right)\nabla\varepsilon \cdot d\mathbf{a} + \int_V \left\{\frac{\varepsilon}{k}[C_{\varepsilon 1}(\mathrm{tr}(\mathbf{P}) + C_{\varepsilon 3}\mathrm{tr}(\mathbf{G})) - C_{\varepsilon 2}\rho\varepsilon]\right\} dv$$

where $C_{\varepsilon 1}$ and $C_{\varepsilon 2}$ are specified coefficients and $C_{\varepsilon 3}$ is determined as in the Standard K-ε model. The coefficient $C_{\varepsilon 1}$ has the value 1.44. The coefficient $C_{\varepsilon 2}$ has the value 1.92 when the linear pressure-strain term is used, and has the value 1.83 when the quadratic pressure-strain term is used.

A two-layer formulation, which solves for but prescribes algebraically with distance from the wall, is available for use with the linear pressure-strain model.

The linear model for the pressure-strain term comprises four terms; these are the rapid part, the slow part, and their respective wall-reflection terms:

$$\underline{\Phi} = \underline{\Phi}_1 + \underline{\Phi}_2 + \underline{\Phi}_{1w} + \underline{\Phi}_{2w}$$

The first term in the right hand side, the slow pressure strain term, is modelled as

$$\underline{\Phi}_1 = -C_1\rho\frac{\varepsilon}{k}\left(\mathbf{R} - \frac{2}{3}k\mathbf{I}\right)$$

While the second one, the rapid pressure strain term is

$$\underline{\Phi}_2 = -C_2\left[\mathbf{P} + \mathbf{G} + \mathbf{F} - \frac{1}{3}\mathbf{I}\ \mathrm{tr}(\mathbf{P} + \mathbf{G})\right]$$

and the slow wall-reflection term is

$$\underline{\Phi}_{1w} = \rho C_{1w}\frac{\varepsilon}{k}\left[(\mathbf{R}:\mathbf{N})\ \mathbf{I} - \frac{3}{2}(\mathbf{R}\cdot\mathbf{N} + \mathbf{N}\cdot\mathbf{R})\right]f_w$$

where

$$f_w = \min\left(\frac{k^{3/2}}{C_l \varepsilon d}, f_w^{\max}\right)$$

$$f_w^{\max} = 1.4$$

d is the wall distance and N is defined as

$$\mathbf{N} = \mathbf{n} \otimes \mathbf{n}$$

where n is the “wall-normal unit vector” defined as the negative of the wall direction.

and, in the end, the rapid wall reflection term, modelled as

$$\underline{\Phi}_{2w} = C_{2w}\left[(\underline{\Phi}_2:\mathbf{N})\ \mathbf{I} - \frac{3}{2}(\underline{\Phi}_2\cdot\mathbf{N} + \mathbf{N}\cdot\underline{\Phi}_2)\right]f_w$$

If the two-layer model is used, the first four coefficients are expressed in terms of the turbulent Reynolds number and anisotropy tensor.

$$C_1 = 1 + 2.58\ a\ a_2^{1/4}\{1 - \exp[(-0.0067 Re_t)^2]\}$$

$$C_2 = 0.75\sqrt{a}$$

$$C_{1w} = -\frac{2}{3}C_1 + 1.67$$

$$C_{2w} = \max\left(\frac{4C_2 - 1}{6C_2}, 0\right)$$

$$Re_t = \frac{k^2}{\varepsilon\nu}$$

The parameter a and the tensor invariants a_2 and a_3 are defined as

$$a = 1-\frac{9}{8}(a_2 - a_3)$$

$$a_2 = \mathbf{A}:\mathbf{A}$$

$$a_3 = A_{ik}A_{kj}A_{ji}$$

Where the anisotropy tensor **A** is defined as

$$\mathbf{A} = \frac{\mathbf{R}}{k} - \frac{2}{3}\mathbf{I}$$

Chapter

4

Results

In this chapter results and post processing of the simulations produced are shown, divided into mesh and turbulence model. Subsequently, the results of the unsteady simulations are presented; finally, a section describing the shape of the tyre wake together with the profile of streamwise velocity in centreline at different downstream stations closes the section.

All the post processing has been developed with STARCCM+ software [29], as the images collected in this chapter. As a reminder for the next results, in Table 4.1 are set the experimental results found by Fackrell [7] in term of drag and lift coefficients[2].

Table 4.1: Experimental values found by Fackrell

Cd	Cl
0.58	0.44

---

[2] As reference surface the tyre frontal area is used

4.1 The influence of the meshing parameters

The first aim of the present work is to make the problem “mesh insensitive”, in other words the solution hasn’t be dependent by the meshing parameters used, in order to provide a common set up where investigate how the various turbulence models behave in the same meshing condition.
It is decided to vary the number of prism in the prism layer: this parameter provides how well viscous sublayer is resolved, keeping constant the thickness of the prism boundary.

In the Table 4.2 are collected the number of run, the number of prisms in the layer divided between number put on ground and on tyre. Also the total number of cells together with the result in terms of lift coefficient and drag coefficient, as mean value on the last 3000 iterations, with their error from experimental data in terms of percentage are illustrated.

One of the most important fact to note is the extreme difficulty to reach an acceptable value of lift coefficient C_l, despite raising the number of prism layer, and, regarding the drag coefficient C_d, a good compromise is achieved using a ratio prism ground – prism tyre 1:2.

Another type of considerations are necessary to be drawn for the simulation that uses the ratio prism ground – tyre 1:3, the number 014. It, in fact, presents several problems of convergence: the values of both coefficients suffer of wide oscillation probably due to something happened during the simulation.

Table 4.2: Number of simulation, number of prism layer on ground and on the tyre, drag and lift coefficient with their error from the experimental data

	Prisms number						
RUN	**Ground**	**Tyre**	**Cells**	**C_d**	**%err**	**C_l**	**%err**
012	4	4	6063671	0.5410	-6.7241	0.3100	-29.5455
014	4	12	7037311	0.6630	14.3103	0.3260	-25.9091
014a	12	12	7652519	0.5460	-5.8621	0.3010	-31.5909
015	4	8	6550491	0.5440	-6.2069	0.2990	-32.0455
018	12	22	8267727	0.5590	-3.6207	0.3100	-29.5455
022	22	22	14447634	0.5410	-6.7241	0.3010	-31.5909

The aim of this kind of simulations is to reduce the residuals convergence criteria explained in sect 3.6, in order to get an acceptable simulation. In the following Figure 1.1 are shown the residuals of the equation just for the coarsest mesh and the finest one; in order not to make the chapter heavy.

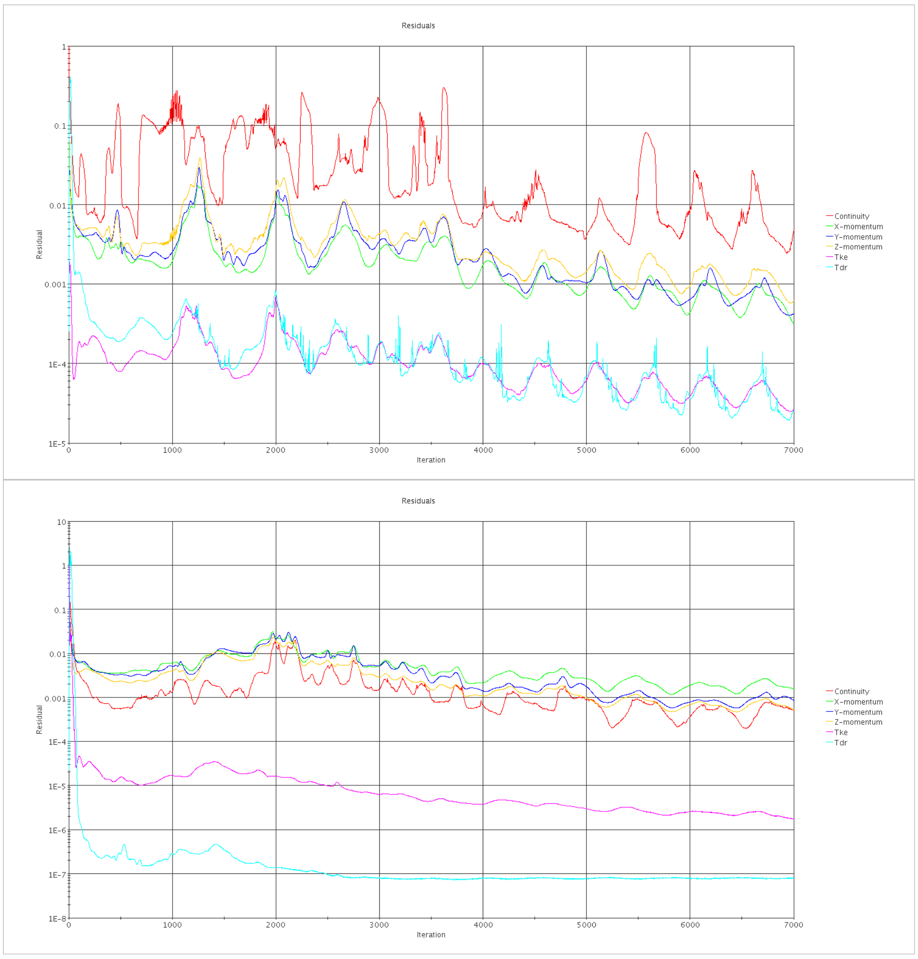

Figure 4.1: Residuals. Top run 012, bottom run 022

As it can be seen, the fluctuations are drastically reduced introducing a finer meshing, although the result and the behaviour of the values of coefficient of lift and drag get a smoother solution nearly in the same time as the Figure 4.2 shows.

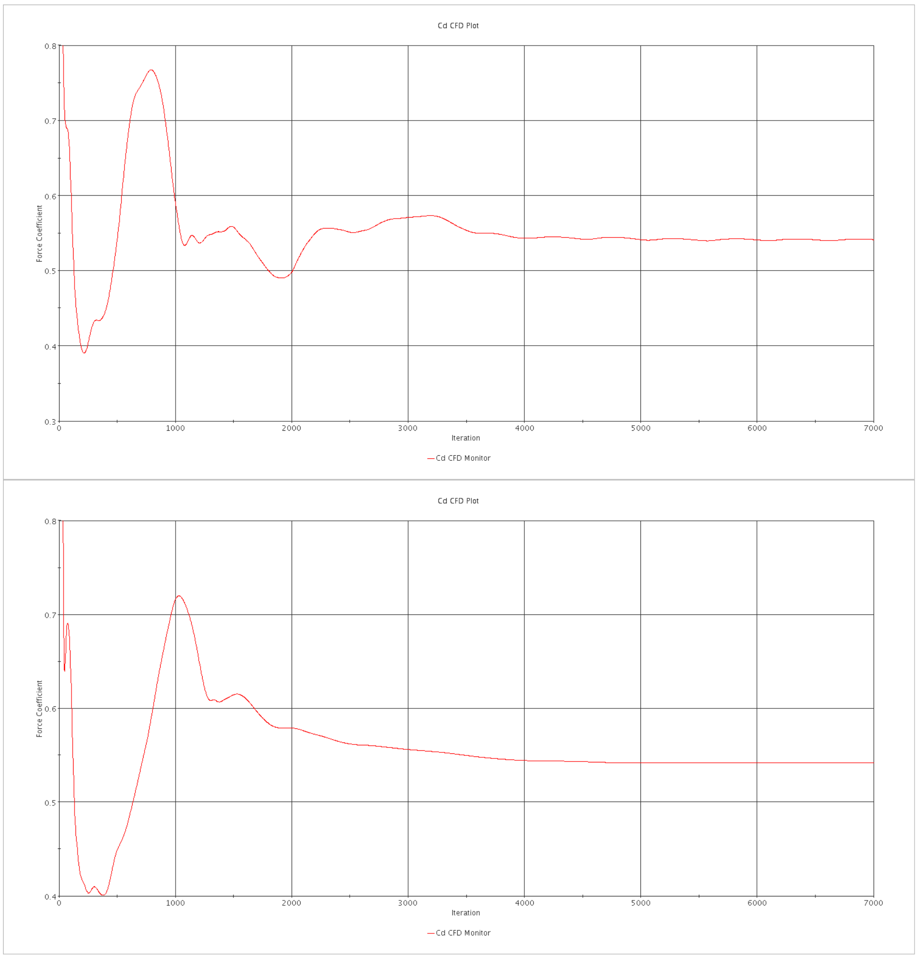

Figure 4.2 Drag coefficient value vs iteration. Top 012, bottom run 022

Obviously, the coarsest mesh has more fluctuation and his behaviour is less smooth than the finest one. The next Figure, 4.3, illustrates contour of mean positive streamwise velocity in the frontal section collocated at x = 0.75D, where D stands for the tyre nominal diameter; of two different simulations. The first using 4 prism layer on ground and tyre, while the second using 4 prisms on ground and 8 on the tyre. Using an higher number of prisms lets to resolve better the viscous sublayer and this is visible in a smoother velocity profile, in other words the thickness of the contour is bigger; it’s important to note that the upper vortex of the tyre remain more squeezed using the same number of prism on the ground and on the tyre, for the same reason it diffuses more, as highlighted by the same figure.

As regard the centreline pressure coefficient, the variation of meshing condition hasn’t lead to sensible variation, so in order not to make the section redundant, it was only reported the best meshing case as first plot in the turbulence model plots Figure 4.12. To announce a result in advance, the separation point is shifted downstream to what predicted by Fackrell, it happens at 1.5 radians respect to the experimental that states at 1.74 radians, considering the rotation used for the calculation and explained in Figure 4.11

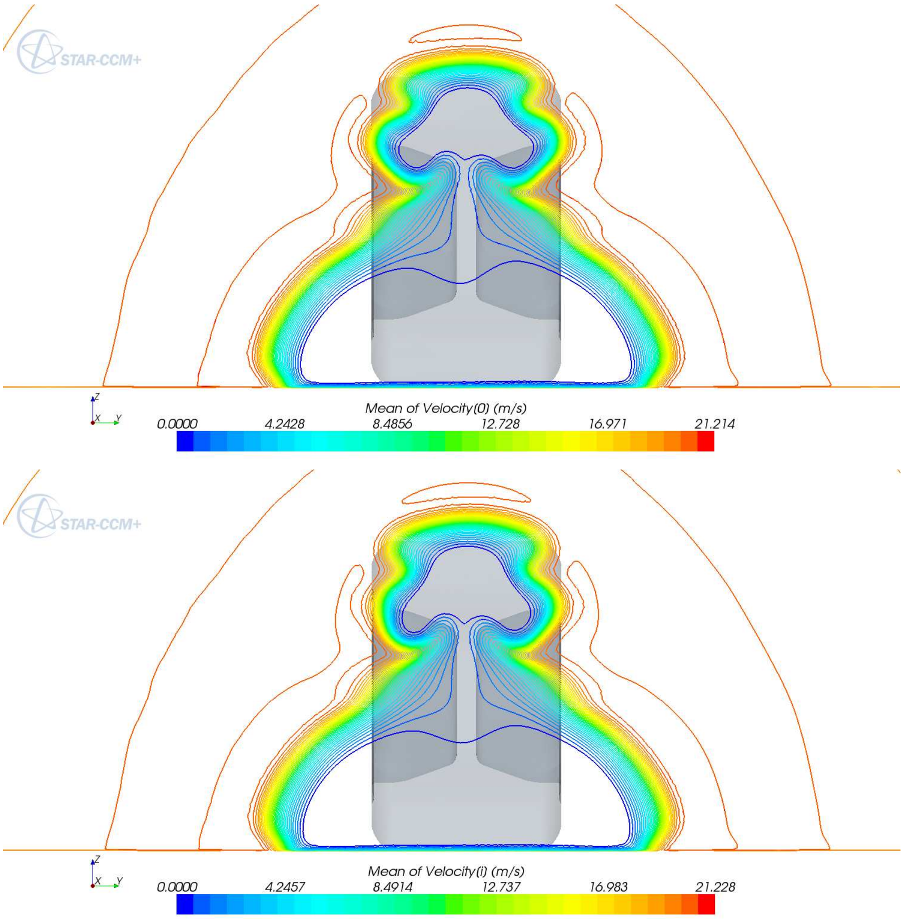

Figure 4.3 Contour mean streamwise velocity. Top: 4 prism on ground 4 on tyre; bottom: 4 prisms on ground 8 on tyre

Since the number of prisms that makes the less difference between the experimental value of drag coefficient and the calculated one is for 12 it has been investigated the combination of 12 prisms on ground and 12 prisms on tyre, 12 on the ground and 22 on the tyre and 22 on the ground and tyre and it is found the mesh insensitive sought, as witnessed by Figure 4.4 in which is presented the same type of value at the same downstream station as Figure 4.3.

It has been chosen the last value, corresponding to the combination of 22 prism on ground and 22 on tyre, because the will to investigate a wall treatment in which no approximation in the very first part of the velocity field near boundaries is used, requires a wall y+ value, namely the value in wall unit which corresponds to the first superficial element on the wall boundary, less than 1. Although the ratio 1:2 seems to be the one which provides best results.

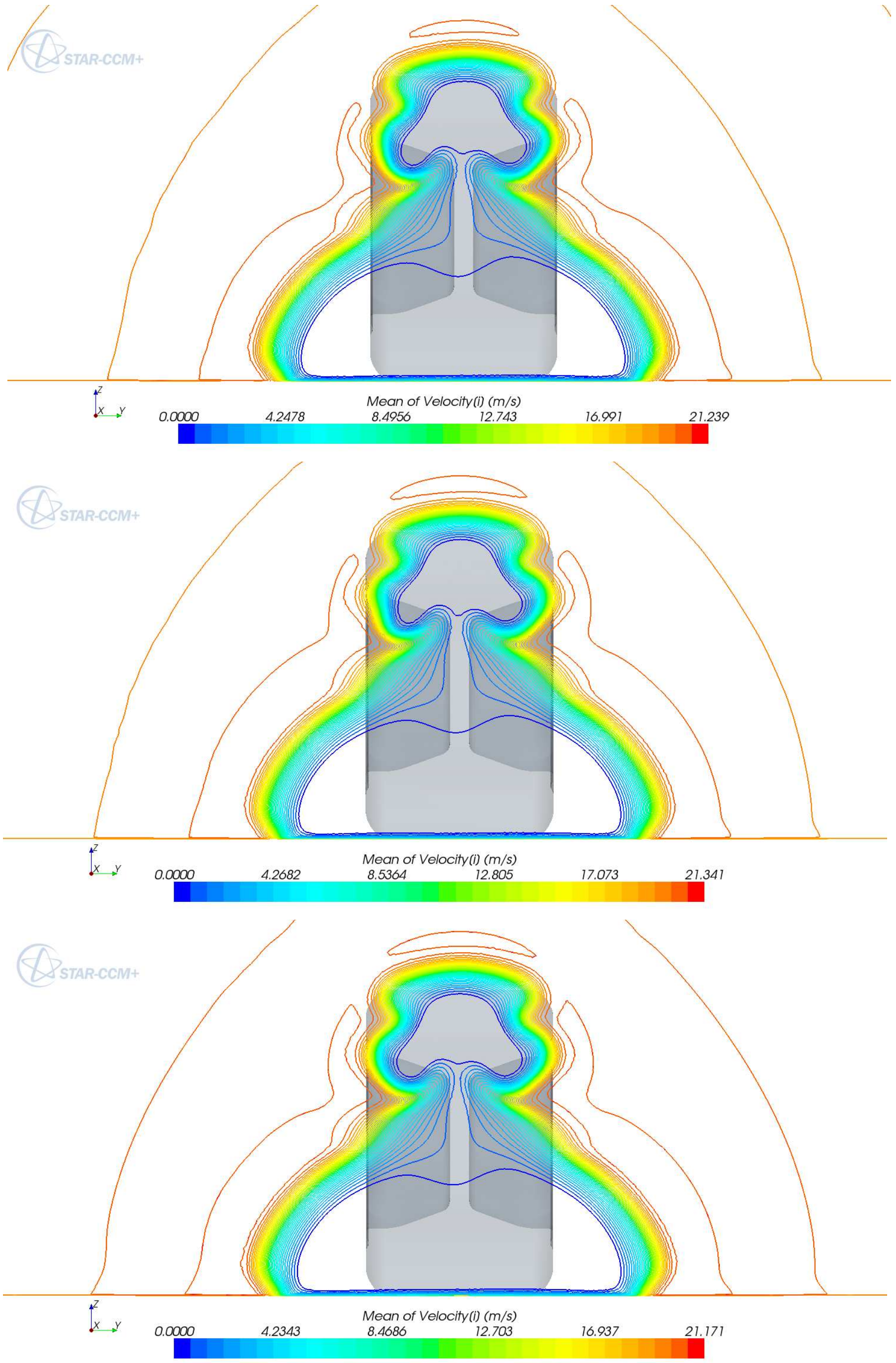

Figure 4.4 Contour mean streamwise velocity. Top: 12 prism on ground 12 on tyre; middle: 12 prism on ground 22 on tyre bottom: 22 prisms on ground 22 on tyre

4.2 The introduction of turbulent suppression

According to what written by Fackrell

"… Smoke visualization experiments show that separation occurs on the rotating wheel at about 280° … [in other words, flow on rotating wheel separates at 80 ° downstream from the stagnation point]

… the layer becomes turbulent far forward on the rotating wheel, within about 20° of the stagnation point. There is no sudden transition to turbulence, but its intensity gradually grows until separation is reached. …"

Keeping in mind what just reported, other two simulations are planned, in which the turbulence is suppressed for 20° from the stagnation point and the second for 80° starting from the same beginning.

The result in form of mean lift and drag coefficient are tabulated in Table 4.3; the value is oscillating with variation larger than 5% for both coefficients.

Table 4.3: Number of simulation turbulence suppression portion, drag and lift coefficient with their error from the experimental data

RUN	Cd	%err	Cl	%err
030 TBL suppr. st~20°	0.6582	13.4828	0.3188	-27.5455
031 TBL suppr. st~80°	0.5479	-5.5345	0.3445	-21.7045

It's important to note that the simulation where the turbulence is suppressed for the first 20° presents an overestimate value of drag coefficient and a consequent raise of the value of lift coefficient; on the other hand, the values provided by the second simulation seem in trend with what seen in the previous pages. The cause of the results of the first simulation will be investigate in this section.

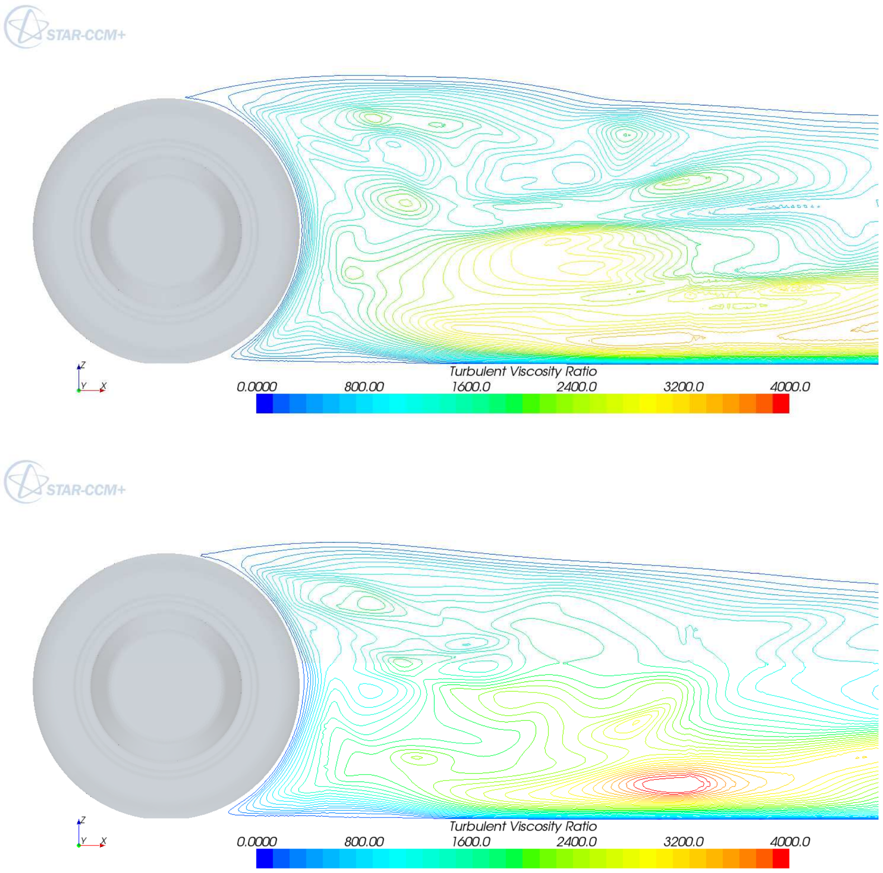

Figure 4.5: Contour turbulent viscosity ratio. Top: turbulent suppression from stagnation point to 20°. Bottom: turbulence suppression from stagnation to 80°

Concerning how the turbulence suppression affects the tyre wake, in Figure 4.5 and 4.6 are illustrated the contour of turbulent viscosity ratio in centreline, the ratio between the turbulent viscosity and the cinematic viscosity, using a same range scale for both the simulations and a contour of mean positive streamwise velocity in centreline, in order to explain how turbulent viscosity distribution is reflected in the behaviour of the velocity field.

As said in the previous chapter the turbulent viscosity has its weight in the part of shear velocity profile. It’s clear to note that if the turbulence is suppressed for the first 20° from the stagnation point the height and the flow shear leaving the tyre are higher than the second one, while the high value of viscosity ratio in the middle zone leads to a higher vertical dimension of the lower vortex.

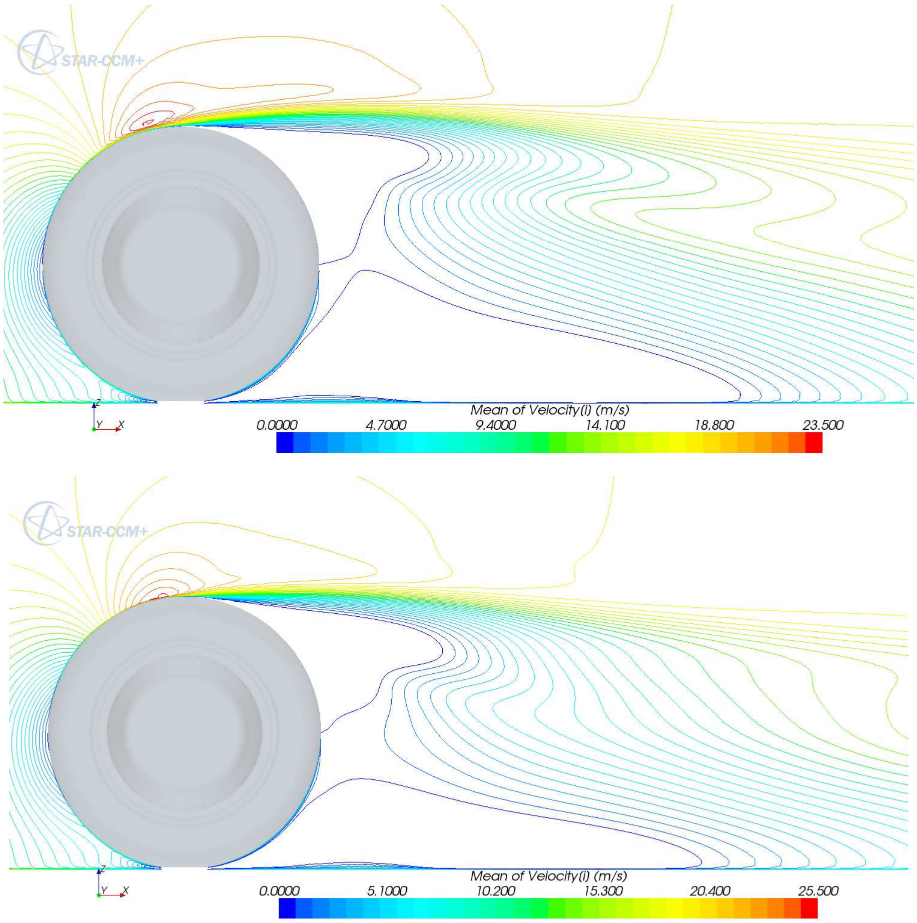

Figure 4.6: Contour mean positive streamwise velocity Top: turbulent suppression from stagnation point to 20°. Bottom: turbulence suppression from stagnation to 80°

Figure 4.7 and 4.8 show the contour of mean positive streamwise velocity at different station of streamwise position in frontal view: 0.5D, 0.75D and 1D, where D stands for the nominal diameter. The lower vortex for the case with turbulent suppression for the first 20° from the stagnation point has got a very different shape respect to all the other in this chapter and this is caused by the presence of separation occurs in the edge of the rim as it shown in Figure 4.9. This separation causes the particular shape of the vortex to be narrow, his diffusion downstream is little and the Fackrell’s jetting phenomena isn’t present. Also the upper vortex is affected by this separation becoming more squeeze than the other already seen and it will be illustrated in the following results.

To link to what described at the beginning of the section, the separation is the cause of the rise of drag coefficient and this leads to the consideration that separation on the rim doesn’t occur in the real Fackrell’s facility.

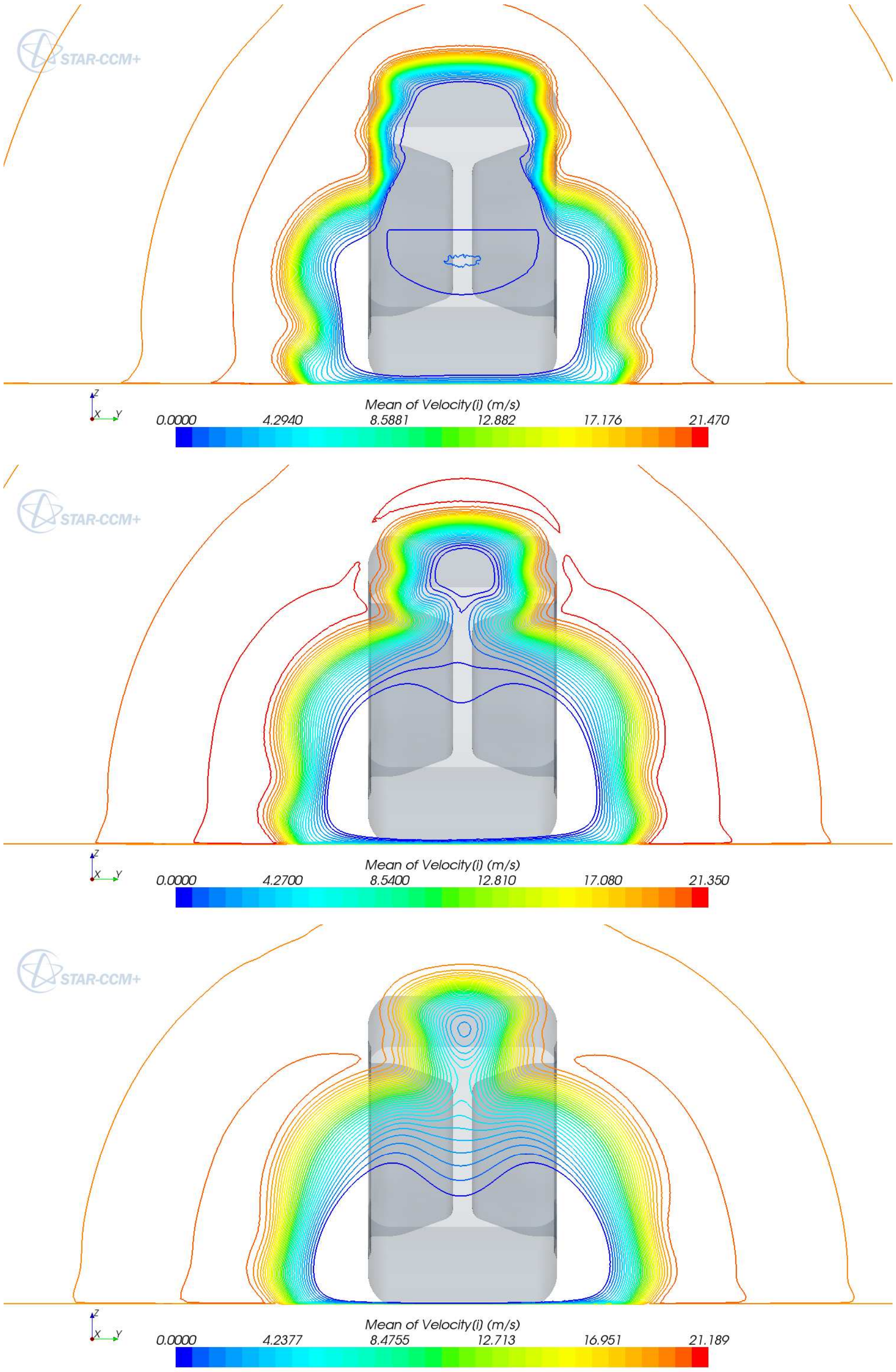

Figure 4.7: Contour mean positive streamwise velocity for turbulent suppression from stagnation point to 20°. From top to bottom: x = 0.5D, x = 0.75D, x = 1D

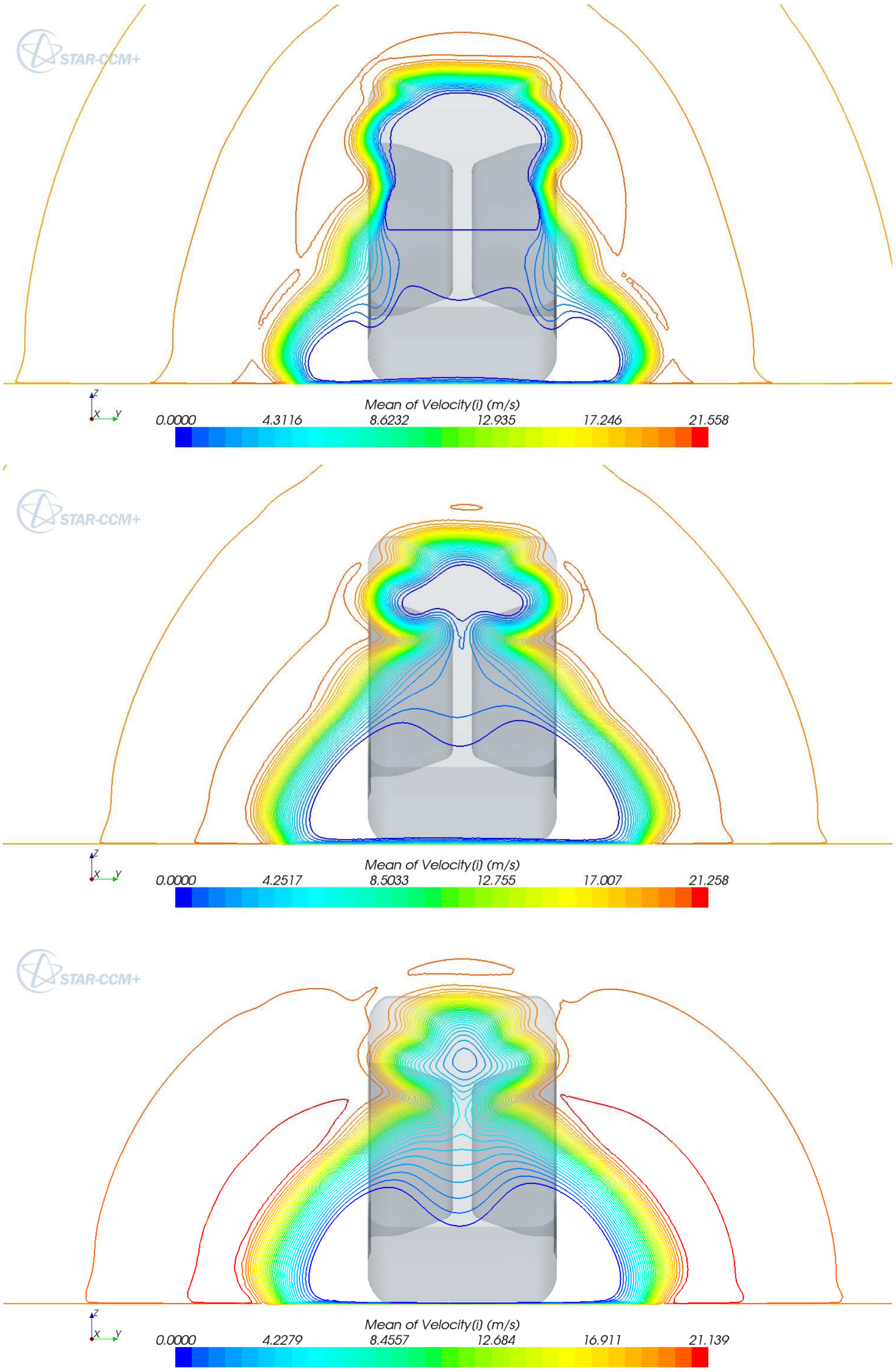

Figure 4.8: Contour mean positive streamwise velocity for turbulent suppression from stagnation point to 80°
From top to bottom: x = 0.5D, x = 0.75D, x = 1D

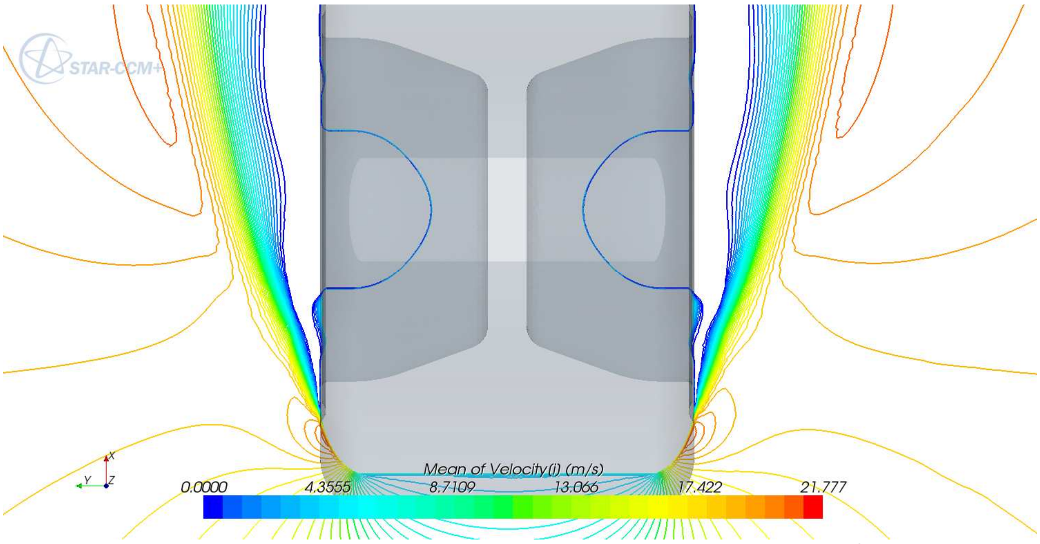

Figure 4.9: Contour mean positive streamwise velocity at z = 0.25 D turbulence suppression from stagnation to 20°

From the other hand, the jetting phenomena is clearly observed from the contour of Figure 4.8 in the top figure closest to the tyre. As it is predicted by the contour of the Figure 4.7 the bottom part of the upper vortex is shifted up, while its shear dives downstream, as predicted by the contour of turbulent viscosity ratio (Figure 4.5).

As far as the upper vortex, it’s important to note that the presence of zone of turbulent suppression causes the rapid decay of the vortex itself, since the turbulent kinetic energy produced is less than what produced if there isn’t turbulent suppression. As prove of that, in Figure 4.6 is illustrated the contour of mean turbulent kinetic energy in centreline for the two simulations in comparison with the same, from mesh characteristics point of view, without any turbulent suppression. Suppressing the turbulence in the first 20° from the stagnation point seems to have similar behaviour, respect to the one without suppression, but the turbulent kinetic energy decays more rapidly, and more rapidly decays for the 80° suppression, for the reason that the amount produced is less as it can be seen by the upper limit of the scale.

As regard as the tyre wake, Figure 4.10 supports the statement that the more turbulent kinetic energy is produced, the more the tyre wake rises up downstream; this could be seen from a numerical point of view because the turbulent viscosity is directly proportional to the square of turbulent kinetic energy, so its contribution makes the fluid more viscous.

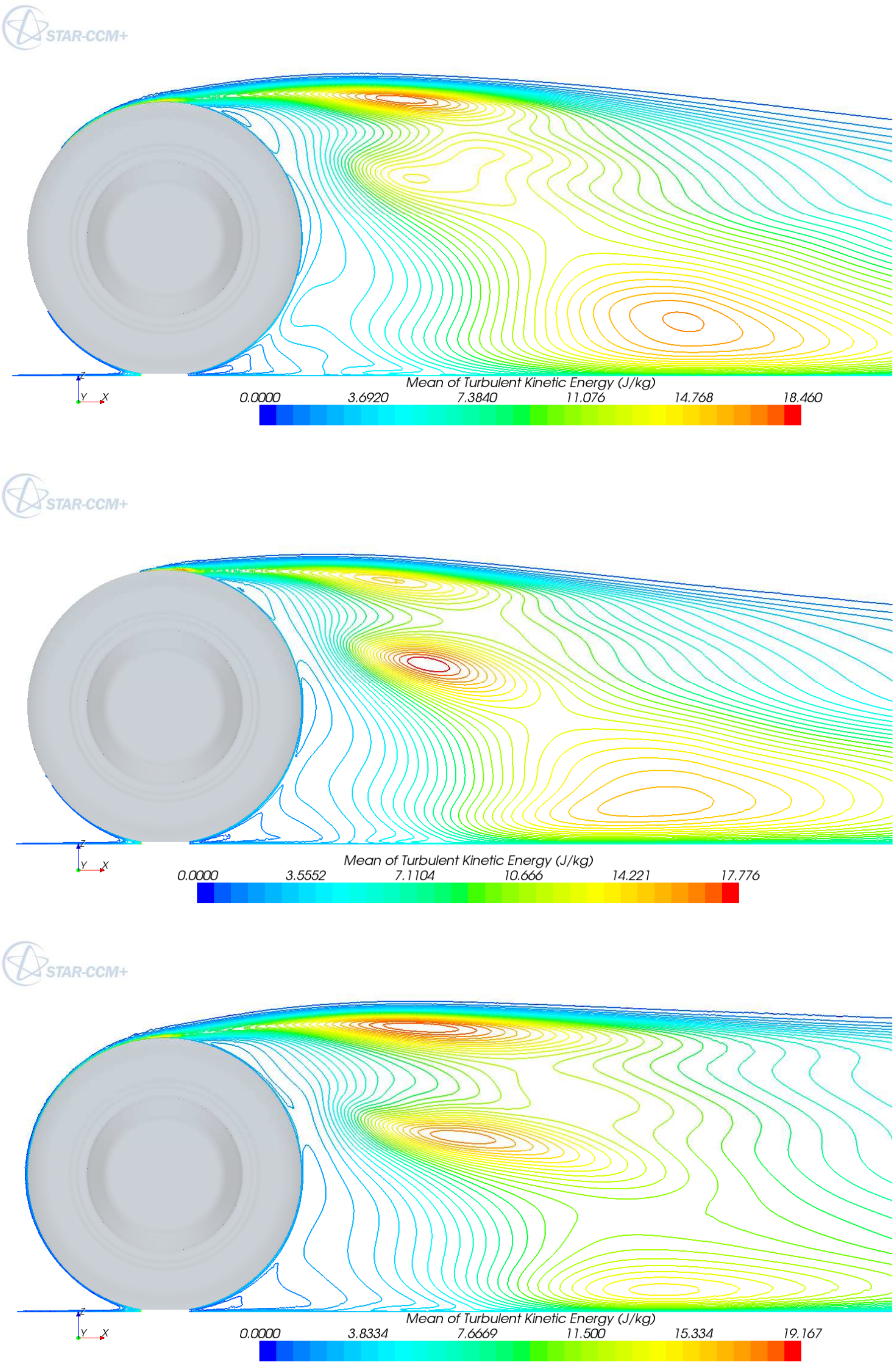

Figure 4.10: Contour mean turbulent kinetic energy. From top to the bottom turbulence suppression from stagnation to 20°, turbulence suppression from stagnation to 80°, no turbulent suppression

4.3 The influence of the turbulence model

In order to get easier the fruition of the results, in the following Table 4.3 are summarized the case investigated by the author. It's useful remember that the meshing parameters remain the same and they refer to the last configuration seen in the previous section. The number of runs developed is 5 and the turbulence model chosen are the most common and the most used in commercial CFD code, as previous mentioned. Together with the turbulence model, Table 4.3 shows the result of the lift and the drag coefficient, as mean value on the last 3000 iteration, and their difference in term of percentage from the experimental value found by Fackrell. It's important to note that all the turbulence models underestimate the experimental data: as regards the coefficient of drag, the K-ω SST model provides less difference, while the K-ε low y+ is the model with the less difference from the experimental lift coefficient; since the differences in drag coefficient error is similar in all the turbulence model the last still remains the best turbulence model which fits both the coefficient.

Table 4.4: Number of simulation, Turbulence model, drag and lift coefficient with their error from the experimental data

RUN	TBL MOD	C_d	%err	C_l	%err
022	K-ε all y+	0.5410	-6.7241	0.3010	-31.5909
034	K-ε low y+	0.5606	-3.3448	0.4183	-4.9318
035	K-ω SST	0.5319	-8.2931	0.3142	-28.5909
036	Spalart-Allmaras	0.5622	-3.0690	0.3092	-29.7273
043	RSM	0.5100	-12.0690	0.3430	-22.0455

In order to complete the comparison with experimental and numerical data in Figure 4.12 in the following page are illustrated the values of pressure coefficient; in each image is plotted also the experimental data and the sequence of the images follows the line of the Table 4.4.

In order not to create misunderstanding in the reader the convention of the direction theta is illustrated in the figure below, Figure 4.11.

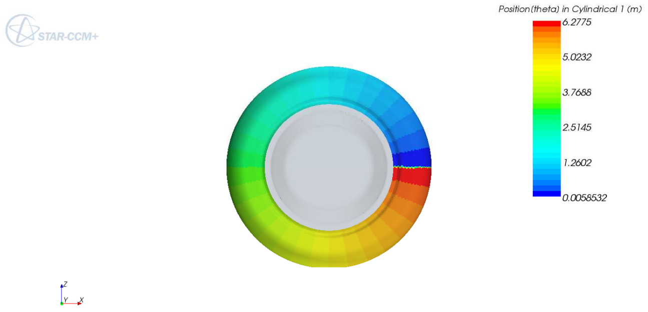

Figure 4.11: Direction tangential coordinate

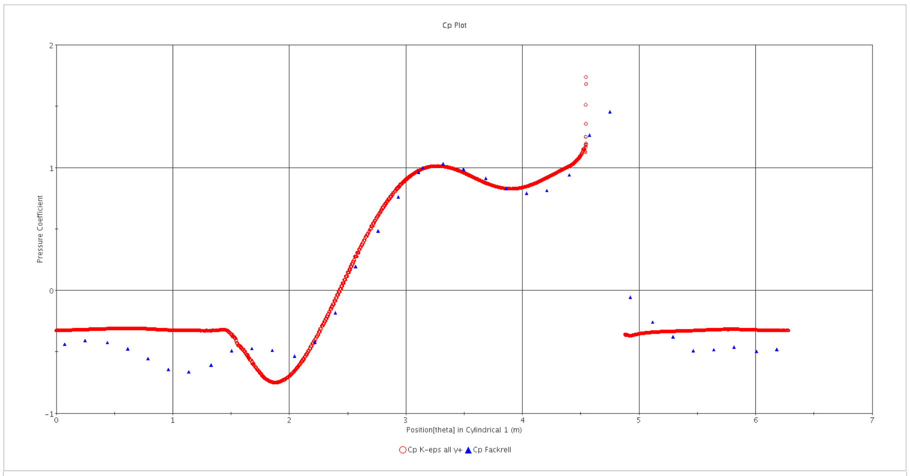
Cp Plot
Pressure Coefficient
2
1
0
-1
0
1
2
3
4
5
6
7
Position[theta] in Cylindrical 1 (m)
○ Cp K-eps all y+ ▲ Cp Fackrell

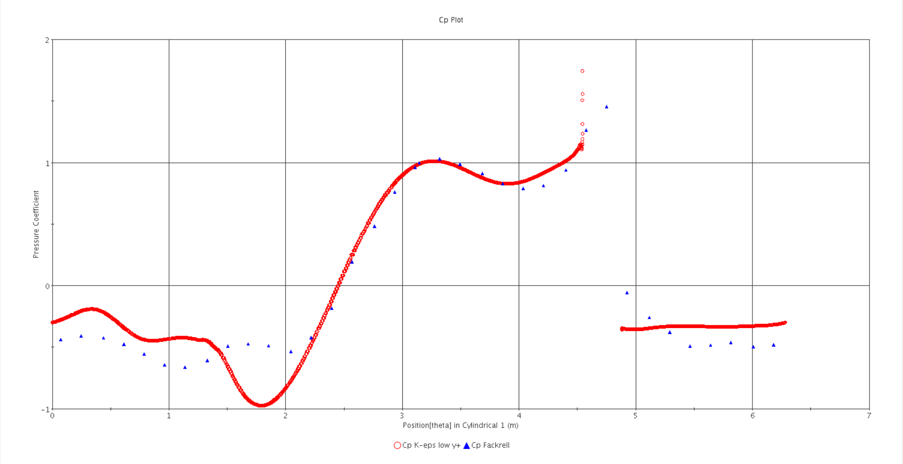
Cp Plot
Pressure Coefficient
2
1
0
-1
0
1
2
3
4
5
6
7
Position[theta] in Cylindrical 1 (m)
○ Cp K-eps low y+ ▲ Cp Fackrell

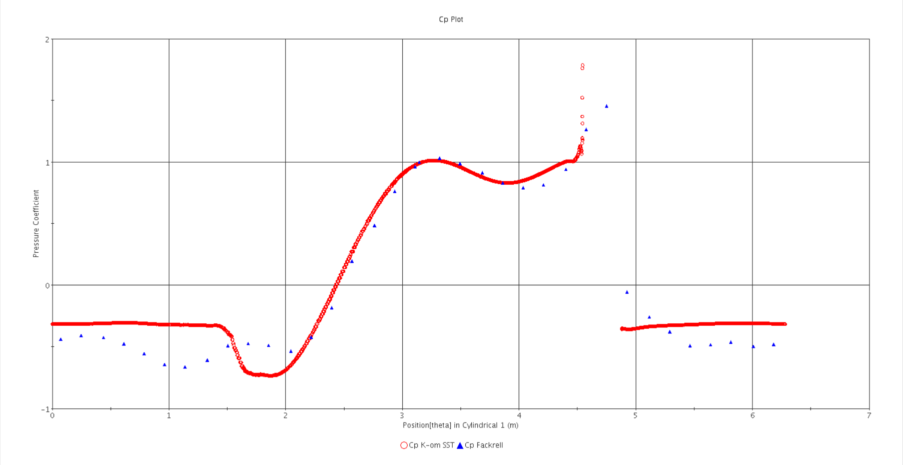
Cp Plot
Pressure Coefficient
2
1
0
-1
0
1
2
3
4
5
6
7
Position[theta] in Cylindrical 1 (m)
○ Cp K-om SST ▲ Cp Fackrell

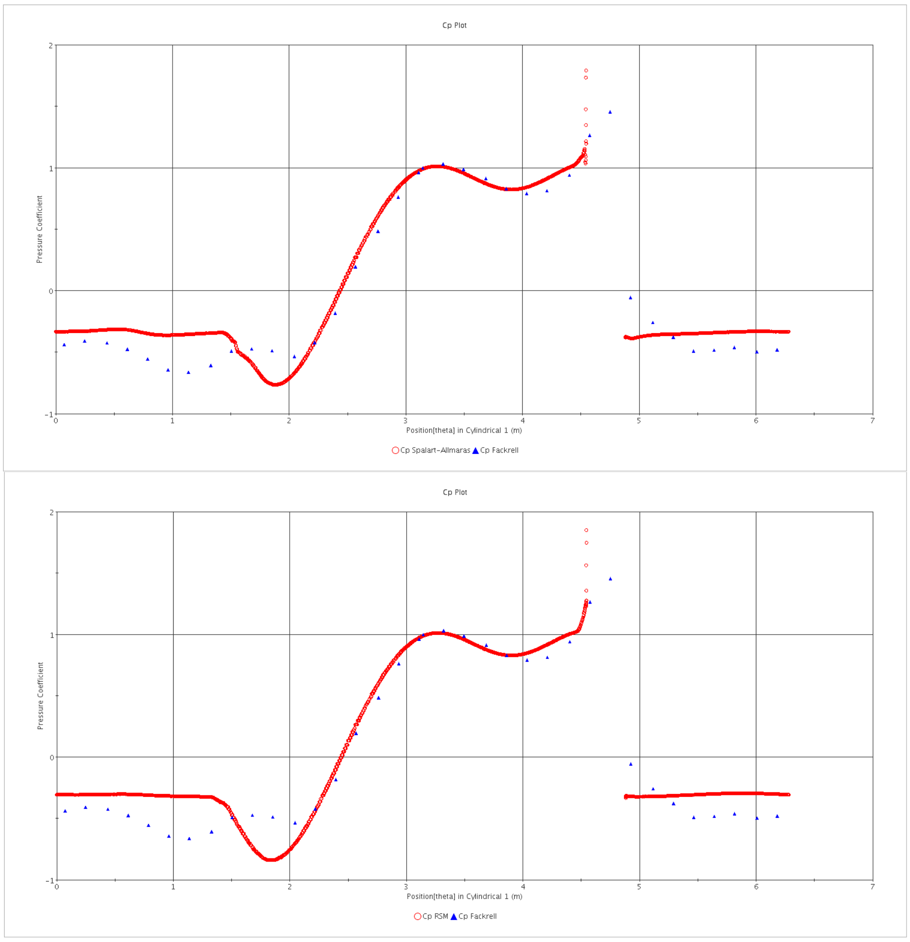

Figure 4.12: Pressure Coefficient in centreline From top to bottom: K-ε all y+, K-ε low y+, K-ω SST, Spalart-Allmaras, Reynolds stress model

The first plot, the K- ε all y + is what anticipated in the previous section; the author has decided to put it in, in order to read the plot from the turbulence model side, since the grid sensitivity is almost transparent. The difference between the changing of wall treatment is visible in the first part of the plot where a non constant trend in captured; this trend is similar qualitatively, but not quantitatively with the one described by experimental data. By contrast, the inferior peak of the pressure coefficient is lower respect of the other, maybe caused by the fully resolution of viscous sublayer.

The K-ω SST has the closest value of the mentioned peak, but as all the turbulence model investigated, his location is upstream respect of the real location.

Although Spalart-Allmaras is the only one equation model investigated, and it isn’t recommended for this kind of simulation, his behaviour is comparable with the other two equation model, especially for the K- ε all y+, with the advantage of less computational efforts.

Also Reynolds stress model seems, from this plot, not provide the right behaviour where the other model can’t, while where the trend is captured it provide a better solution.

In conclusion, no turbulence model can catch the trend seen in the inferior part of the wheel downstream, in other words the trend in the last part of the plot results almost constant for all the plot here investigated.

In Figure 4.13 is illustrated the turbulent viscosity ratio, i.e. the ratio between the turbulent viscosity and the dynamic viscosity: each figure has the same range scale in order to get easier to the reader the comparison between the turbulence models. This parameter well explain how the turbulent model affects the solution in the flow: the turbulent viscosity is the link between the momentum continuity and the one or two equations that describe the Reynolds stress tensor; for the Reynolds stress model, the turbulent viscosity is determined using the half trace of the tensor itself, divided with the dissipation rate.

The most macroscopic difference regard the second figure, K-ε low y+, respect the other: its thickness decade rapidly downstream, and the high values of turbulent viscosity is concentrate in the lower part. The K-ε model, both wall treatment, are the models with the highest value of turbulent viscosity, while the K-ω SST, has comparable gradient near the wall with Reynolds Stress model and far downstream in the upper part is comparable with K-ε one; this confirms how the scheme was built: a K-ε model away from the wall and a K- ω model near the wall.

Spalart-Allmaras has smoother gradient near the tyre tread, especially in the zone near contact patch. The distribution of turbulent viscosity in the upper part is more similar to the K-ε all y+ and it increases moving downstream, witnessed the high diffusivity of the one equation scheme.

Finally, Reynolds Stress model presents similarity to K-ε low y+ in the very first upper part, while in centreline the shear is smoother as K-ω. The presence of the ground is higher felt by the K-ε models.

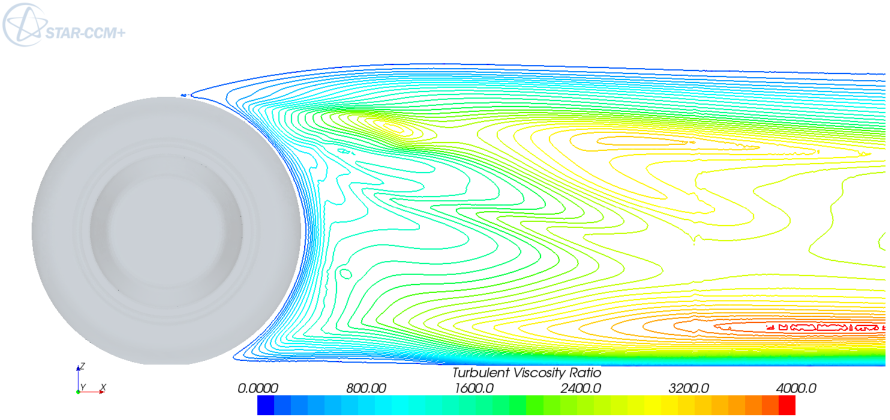
Z
Y
X
Turbulent Viscosity Ratio
0.0000
800.00
1600.0
2400.0
3200.0
4000.0

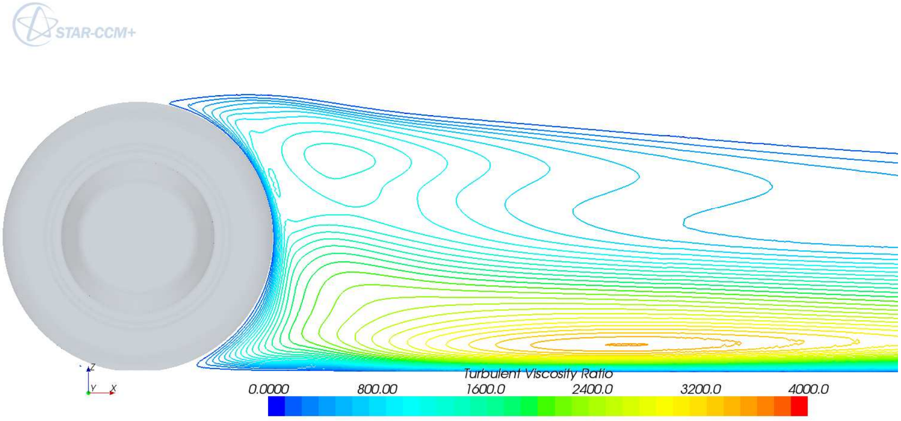
Z
Y
X
Turbulent Viscosity Ratio
0.0000
800.00
1600.0
2400.0
3200.0
4000.0

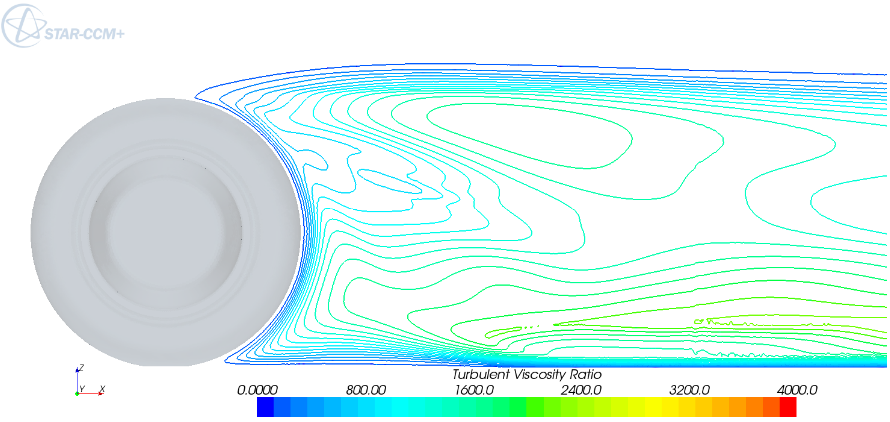
Z
Y
X
Turbulent Viscosity Ratio
0.0000
800.00
1600.0
2400.0
3200.0
4000.0

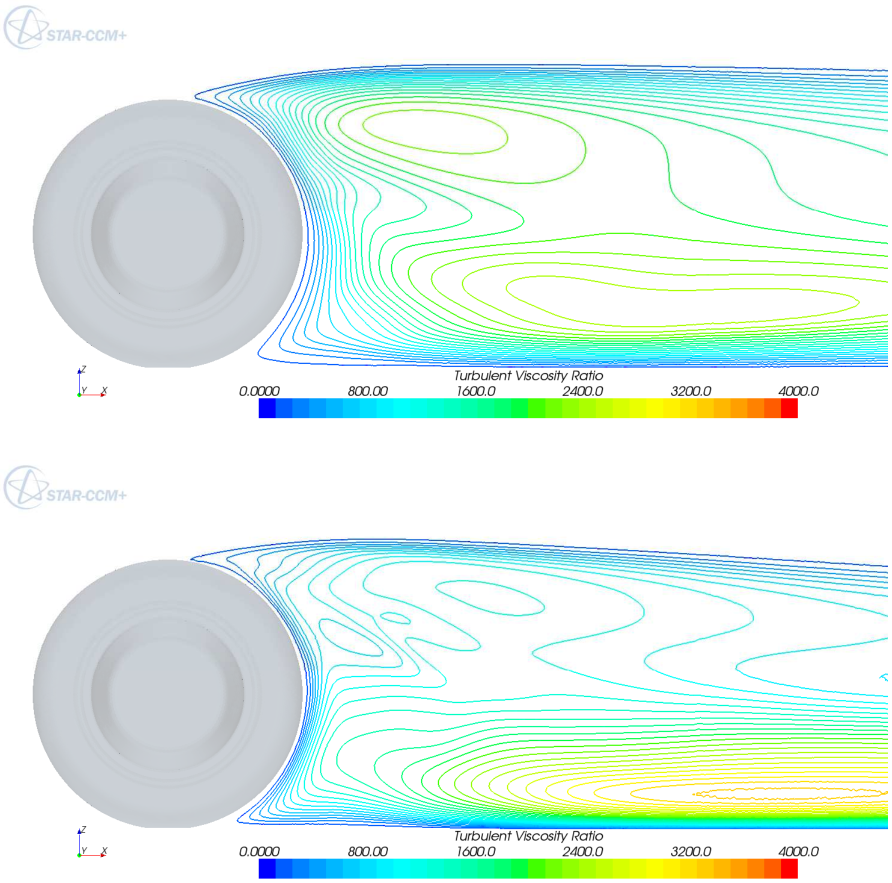

Figure 4.13: Contour turbulent viscosity ratio. From top to bottom: K-ε all y+, K-ε low y+, K-ω SST, Spalart-Allmaras, Reynolds stress model

Turbulent viscosity ratio is determined by two main contributions: the turbulent kinetic energy and the turbulent dissipation rate. Next figures show for each turbulence model, with the only exception of the Spalart Allmaras model, the turbulent kinetic energy first and turbulent dissipation then, using for each models the same range scale, in order to get the comparison clearly. By investigating this type of values, the aim of the author is to identify which of the two values has more weight respect to the other in each part of the flow field.

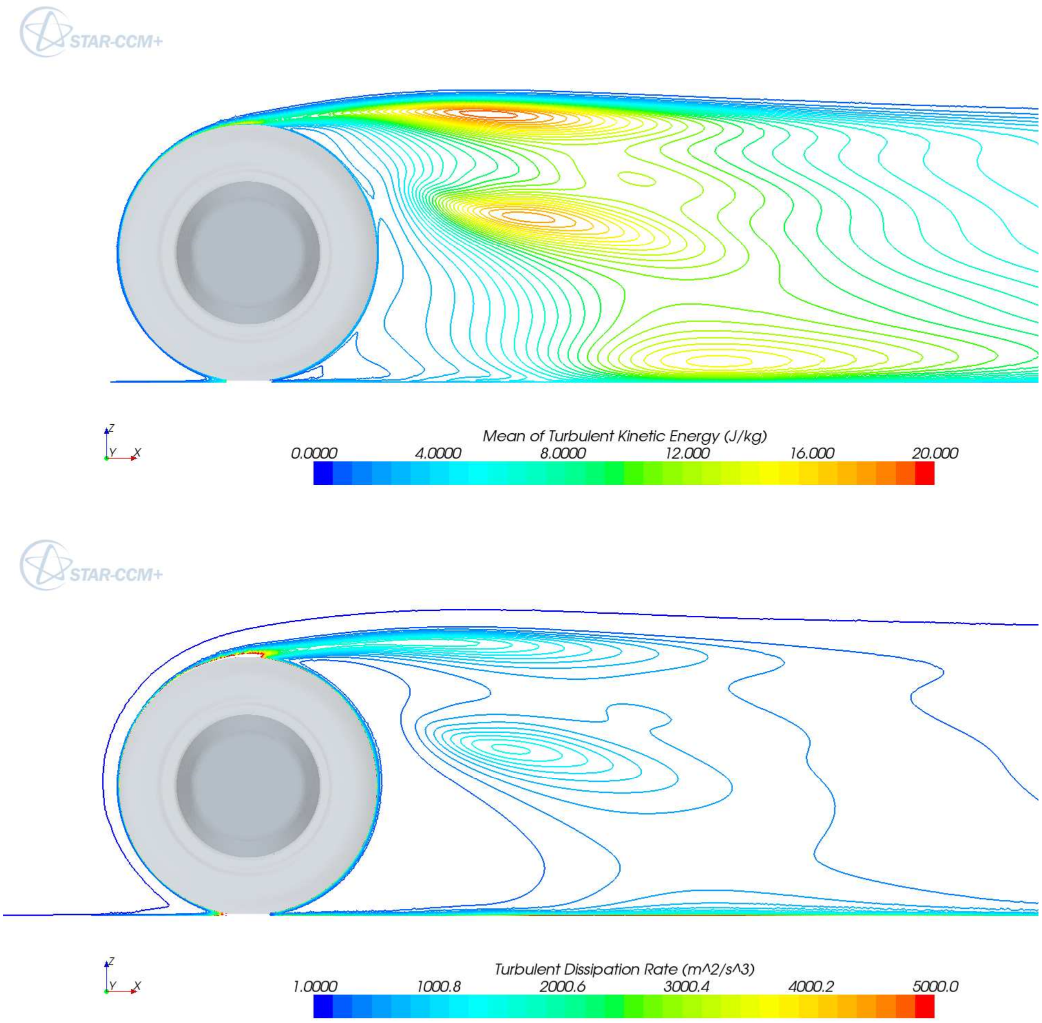

Figure 4.14: Contour turbulent kinetic energy (top) and turbulent dissipation rate (bottom) for the K-ε all y+.

Figure 4.14 illustrate the K-ε all y+ turbulence model. A very important part of dissipation spreads throughout the centreline of the flow field: also an elevated value of turbulent kinetic energy is discovered and this holds the value of turbulent viscosity almost constant in the very first part leaving the upper of the tyre. When moving downstream the value of dissipation fades, while the shear of the kinetic energy stands almost constant, and this leads to an increase of the turbulent viscosity, (the reader should remember the turbulent viscosity is the ratio between the square of turbulent kinetic energy to the turbulent dissipation rate), especially in the part closest to the edge of the shear. This is one of the reasons why the upper wake, using this type of turbulence model, diffuses more downstream.

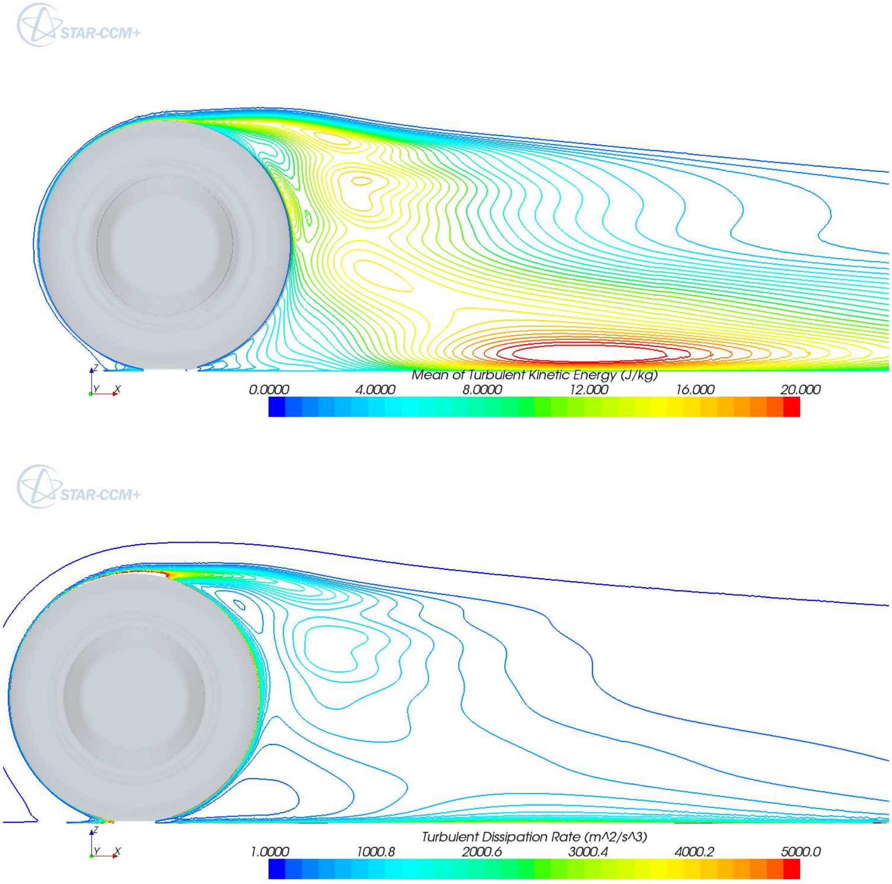

Figure 4.15: Contour turbulent kinetic energy (top) and turbulent dissipation rate (bottom) for the K-ε low y+.

Changing only, and the author desires to stress this important aspect, wall treatment, Figure 4.15 illustrates the same contour for the K-ε low y+ turbulence model. One of the first observations that comes up is the density of the contour of the turbulent kinetic energy, which means the extremely variation moving downstream of the one of the leading actors in the prediction of the velocity itself. A core of high value of turbulent kinetic energy is placed near of the ground in a position, as next figures show, in which the lower tyre wake seems to affect the flow no more. As concerns the upper spot presents in the Figure 4.14 and, to announce a result in advance, found in all the next turbulence model here there isn't no evidence of it, so it can be argue that this type of feature could be cause by the wall treatment itself. The rapid decay of both values obliges the wake not to diffuse more than the other value.

Continuing the investigation of the rapid decay of the upper tyre wake, Figure 4.16 sets in comparison the turbulent dissipation rate on the tyre tread for this two cases, using a top view a the same range scale.

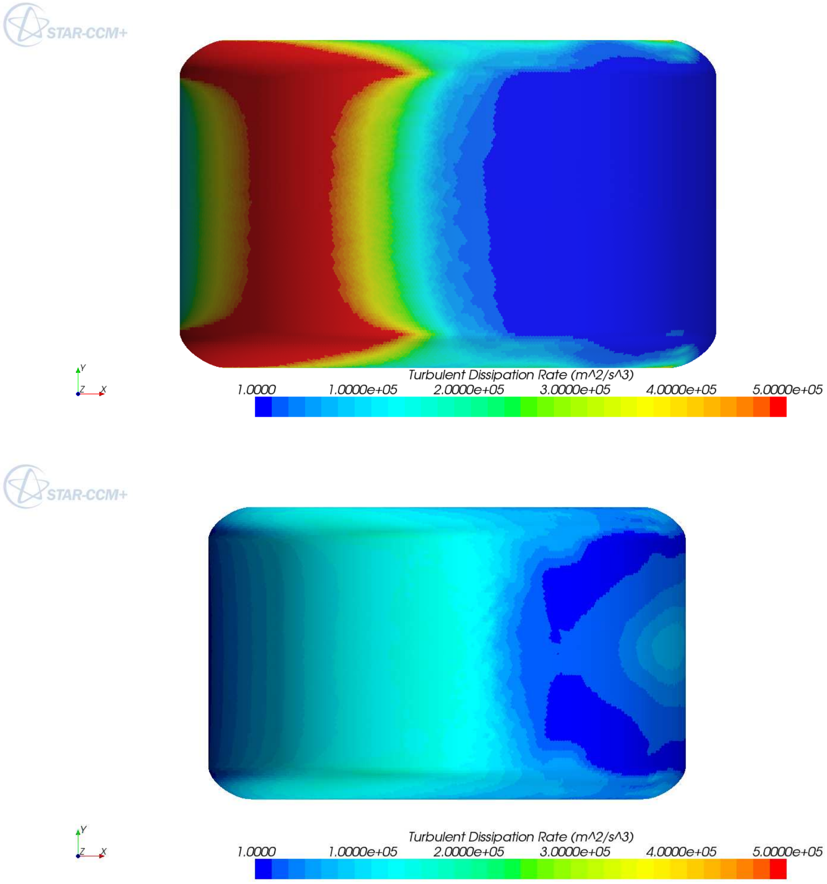

Figure 4.16: Top view of turbulent dissipation rate for the K-ε all y+ (top) and K-ε low y+ (bottom).

Moving in streamwise direction, it is clear to note a zone with elevated turbulent dissipation rate in the K- ε all y+ just before the separation while in the K-ε low y+ doesn't appear. This widely distribution of values on the tread, brings to a uniform value close to the unity. For the other wall treatment, the values hasn't this type of distribution and, its value is more far than the unity. Considering the fact turbulent dissipation rate is inversely proportional to the turbulent viscosity, this means that for the same value of turbulent kinetic energy, the turbulent viscosity for the all y+ wall treatment will be higher than the one for the low y+ wall treatment. As concern the zone with high turbulent dissipation rate, the author argues it can be addressed by the calculation of the normal to the tread.

Another important result to highlight is the thickness of the turbulent dissipation rate presents in the right side of the tyre, side that corresponds to the first values of the pressure coefficients plot illustrated in the previous pages, where a not constant trend is found. Unlike all the other turbulence models, the imposing to resolve all the viscous sublayer, not to leave the choice of the wall treatment to the CFD code, provides a different value of the turbulent dissipation, moving from the 0, always using the convention of Figure 4.11, to almost π/2 near the separation point. Since the turbulent dissipation rate influences the value of the velocity found, the author argues this might be the cause of the different value of pressure coefficient moving on the centreline of the tyre track.

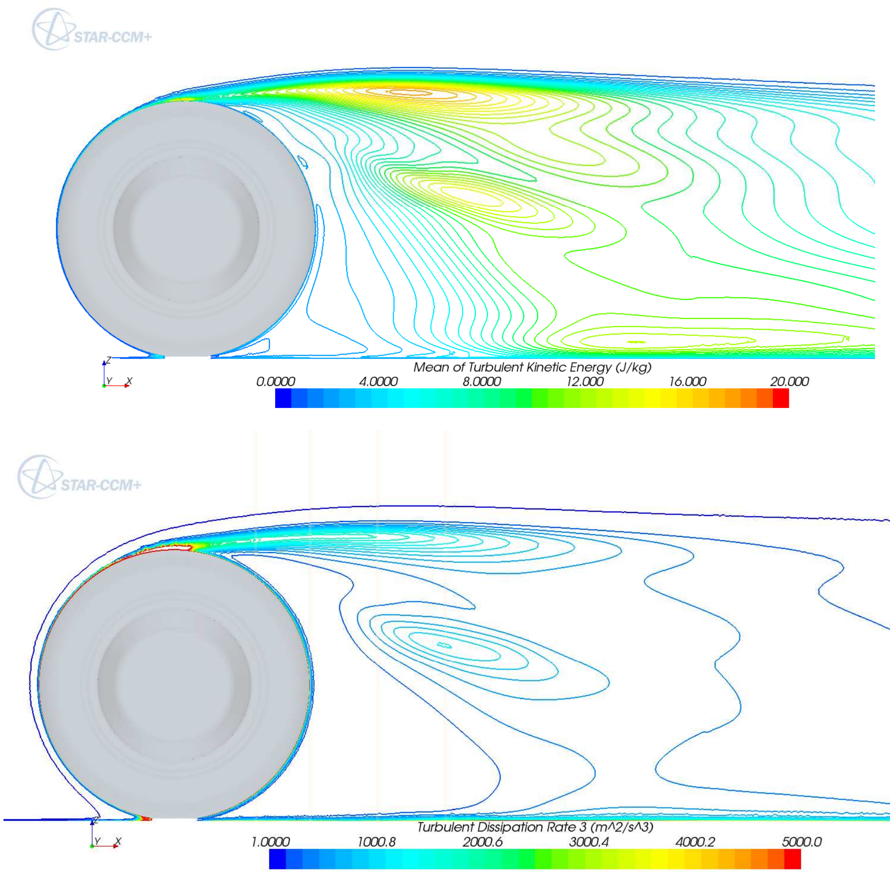

Figure 4.17: Contour turbulent kinetic energy (top) and turbulent dissipation rate (bottom) for the K-ω SST

Figure 4.17 represents the contour of the same quantities illustrated above for the K-ω SST turbulence model. As said before, this turbulence model isn’t the original K-ω, but an hybrid model between K-ε away the wall and K-ω near the wall and this is reflected in the similarities with Figure 4.14 especially in the core of high turbulent viscosity in the upper part of the wake and in the middle as also the high turbulent viscosity diffusion downstream.

In the region between the ground and the tyre, the value of turbulent kinetic energy has a smoother shear respect to both K-ε model: this is the reason why turbulent viscosity plot illustrated in the previous pages presents for the K-ω SST model a smoother shear in the same zone.

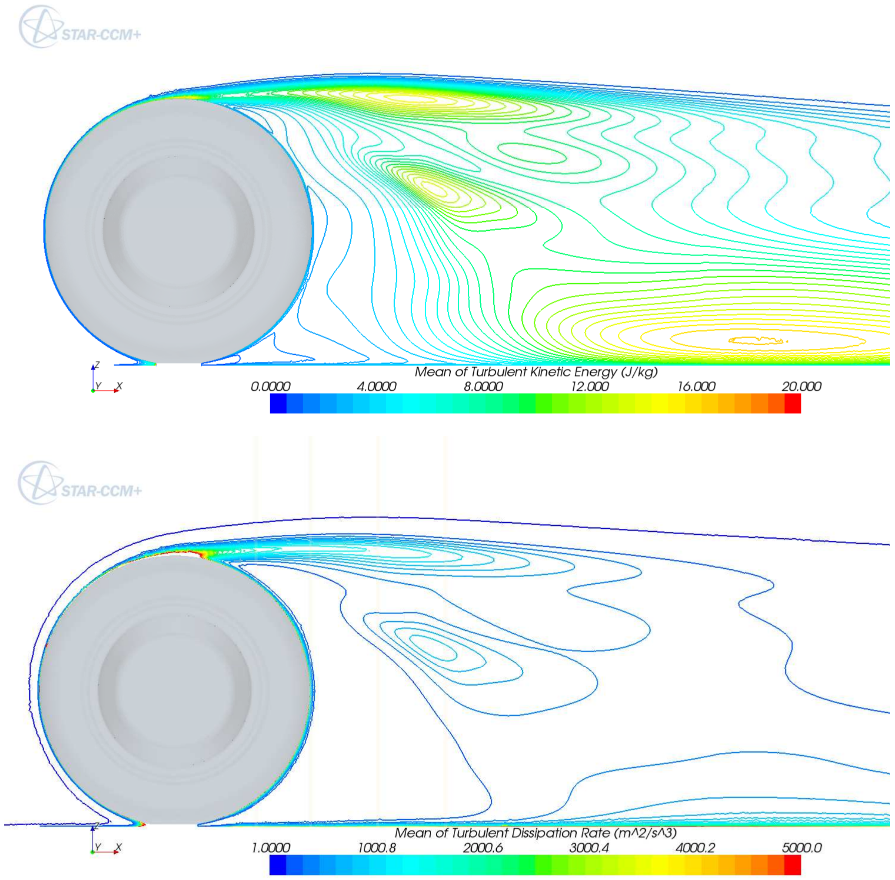

Figure 4.18: Contour turbulent kinetic energy (top) and turbulent dissipation rate (bottom) for Reynolds stress model

Finally figure 4.18 refers to the Reynolds Stress model. One important aspect is the turbulent kinetic energy, computed as the half trace of the Reynolds stress tensor provides a lower value than using an equation that models this important property of a turbulent flow; in addition, the turbulent dissipation rate spreads out less than the other models, although the equation is almost the same from numerical point of view, but the values that contribute to calculate it come from different approximations.

As concern the behaviour of the turbulent dissipation rate, this turbulence model seems to find a better agreement with K-ω SST one, with the exception of the big shear describing the separation in the upper part of the tyre that results more smooth and with a more rapid decay.

In conclusion, the most macroscopic differences are caused by the changing in the wall treatment; the choice of this feature may influence all the turbulent viscosity, so it influences heavily the velocity field.

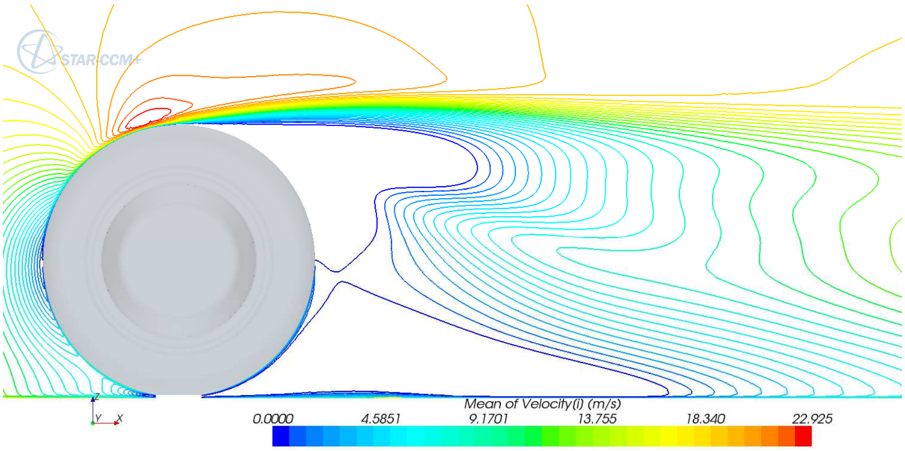

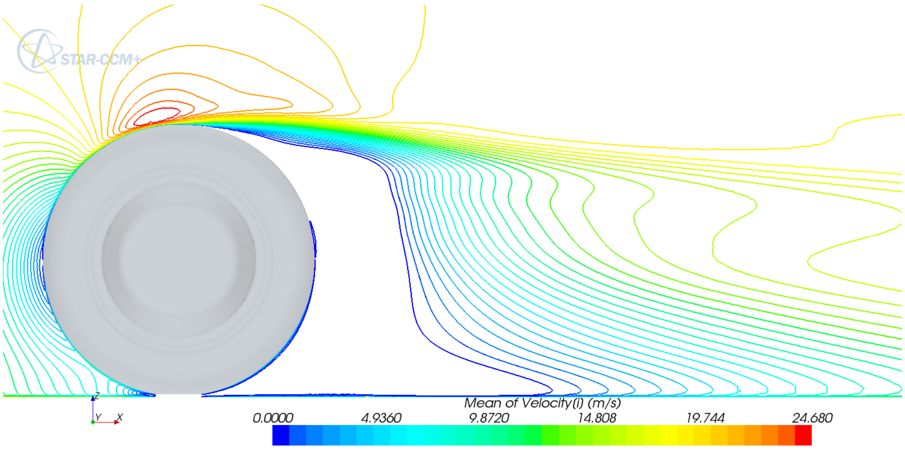

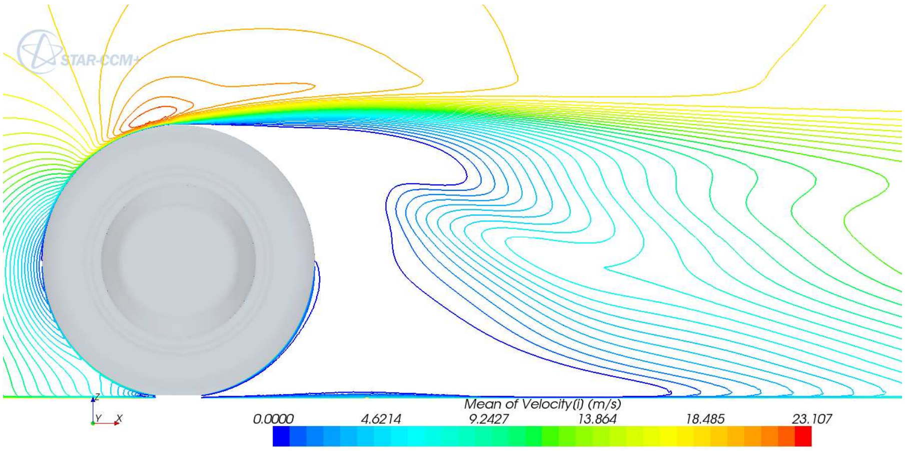

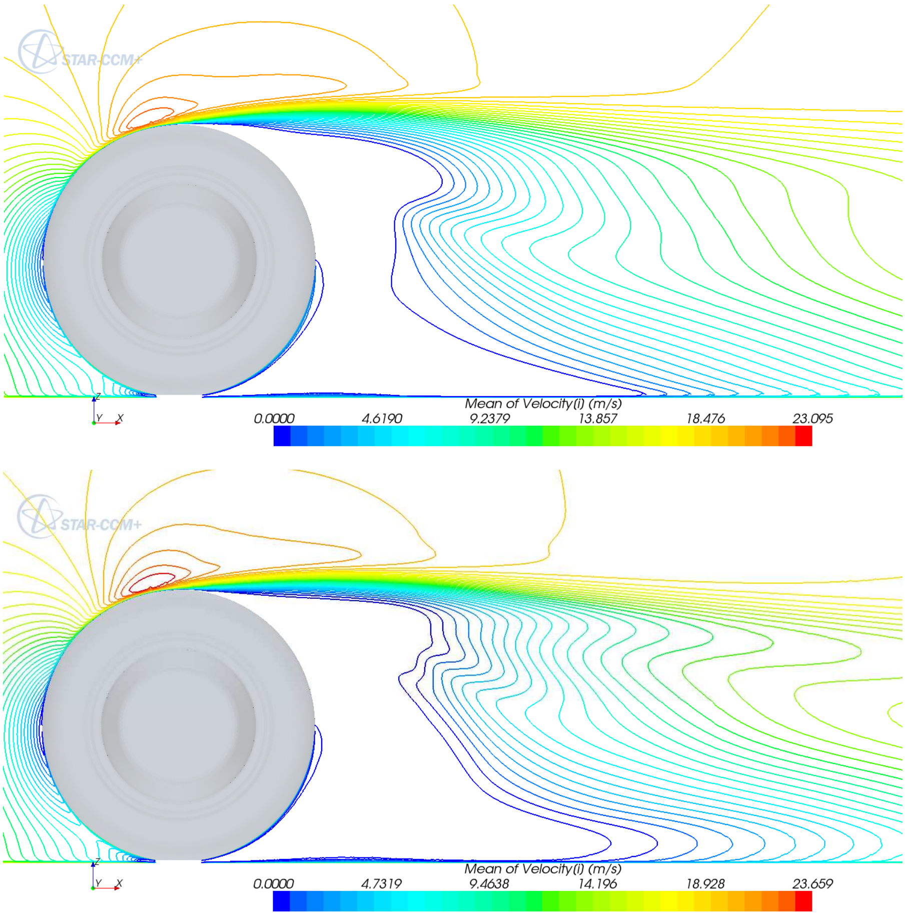

Figure 4.19: Contour mean positive streamwise velocity. From top to bottom: K-ε all y+, K-ε low y+, K-ω SST, Spalart-Allmaras, Reynolds stress model

As mentioned before, in order to understand how these scalar quantities affect the values of velocity, the Figure 4.19 are the contour of the mean positive streamwise velocity for each turbulence model.

The distribution of turbulent viscosity is immediately related with the distribution of the mean streamwise velocity. The big diffusion and the high variation of turbulent viscosity in the middle lead to create two separated vortex for the K-ε all y+, instead of a unique reversed flow zone, as all the other models provide. The presence of elevated ν_t near wall for both K-ε models causes the lower reversed zone to be wider.

It’s important to observe that different choice of turbulence model, with different result of ν_t provide different length and height of the wake: without using any kind of approximation in the near wall region the wake become smaller downstream as the region of turbulent viscosity become smaller; the opposite is seen for the other type of turbulence model. Since the K-ε low y+ is the only one with an error to the lift coefficient less than 5%, instead of an error for the other models of about 30%, the author supposed that the reason could be searched in this type of difference.

It's also worth to note how the upper shear of Spalart-Allmaras and K-ε all y+ are comparable.

In order to describe better the structure of the two couple of contra-rotating vortex which leave the tread the figures from 4.20 to 4.24 describe the contour of the mean positive streamwise velocity in frontal view at three different station streamwise: 0.5, 0.75 and 1 diameter. As other author discovered, the K-ε model is a very robust turbulence model: in fact it doesn't affect the asymmetry of the refinement box, while the other does. The difference in spanwise direction of the refinement box is more evident at x = 0.75D in direction streamwise; it is important to note that the external contour remain almost the same. The increasing in spanwise of the refinement box makes an increasing in the shear, as it can be evident especially for the Reynolds stress model and K-ω SST.

To link with what illustrated before, the low value of turbulent viscosity, viewing the flow frontwise, is transformed in a little diameter of the upper vortex, as the K-ε low y+ shows; this is comparable with what found using Reynolds stress model.

The two vortex generated by the contact patch, well visible in the first of each image, are well highlighted by the K-ω SST and the Spalart-Allmaras with a bigger height respect to K-ε and Reynolds stress model. Its interaction with the lower vortex of the wheel contributes to make the last wider.

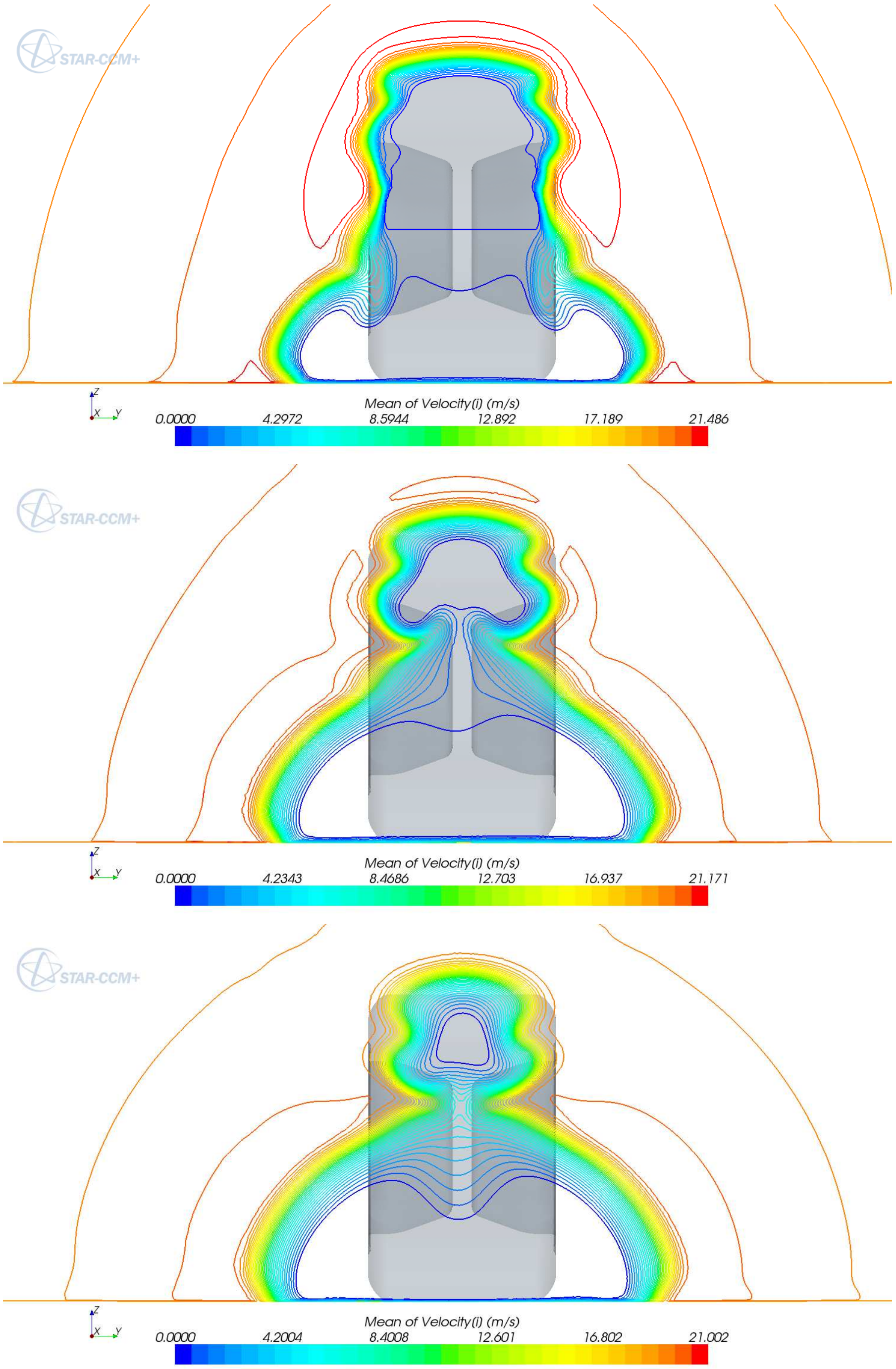

Figure 4.20: Contour mean positive streamwise velocity for K-ε all y+. From top to bottom: x = 0.5D, x = 0.75D, x = 1D

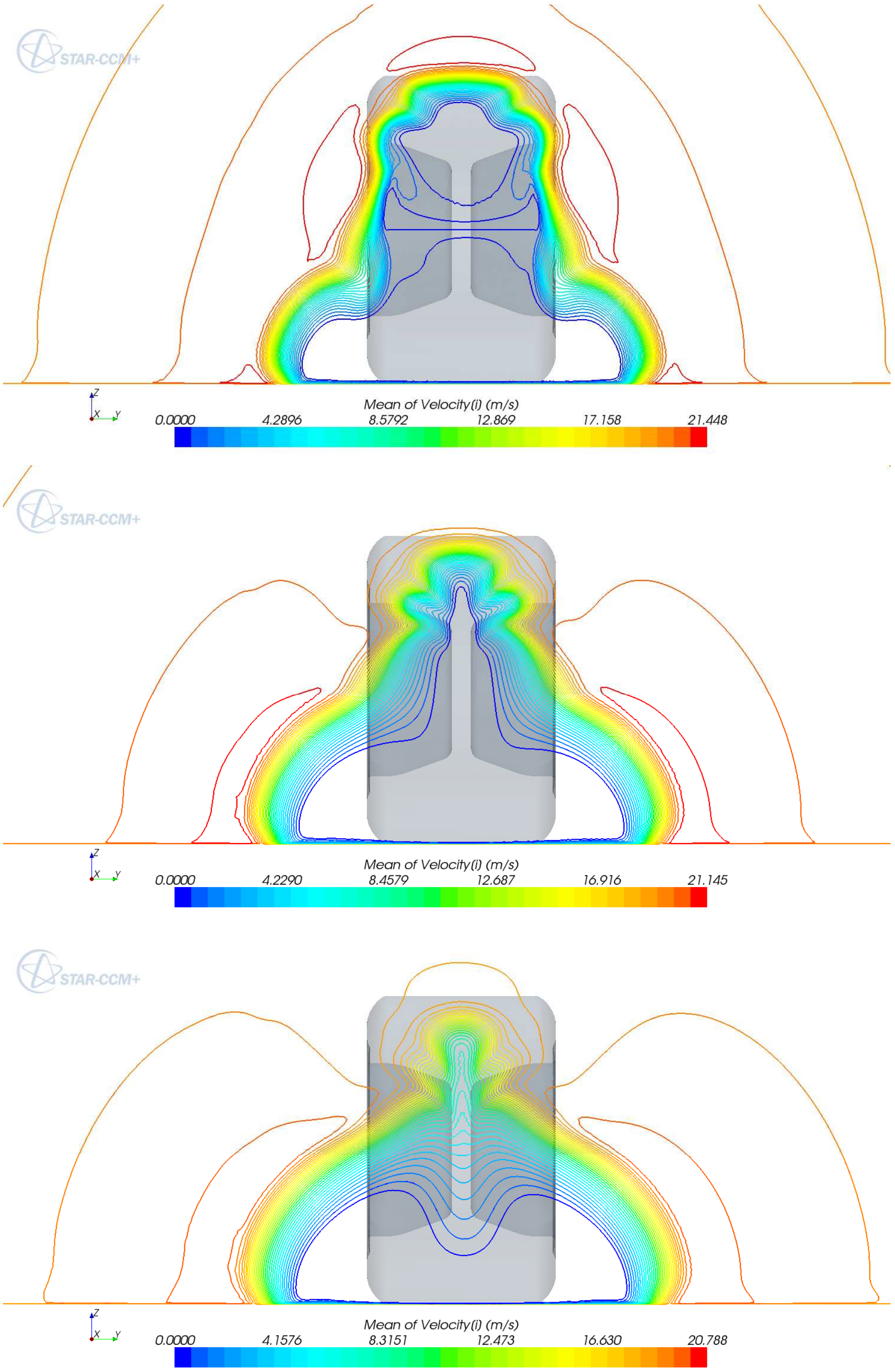

Figure 4.21: Contour mean positive streamwise velocity for K-ε low y+. From top to bottom: x = 0.5D, x = 0.75D, x = 1D

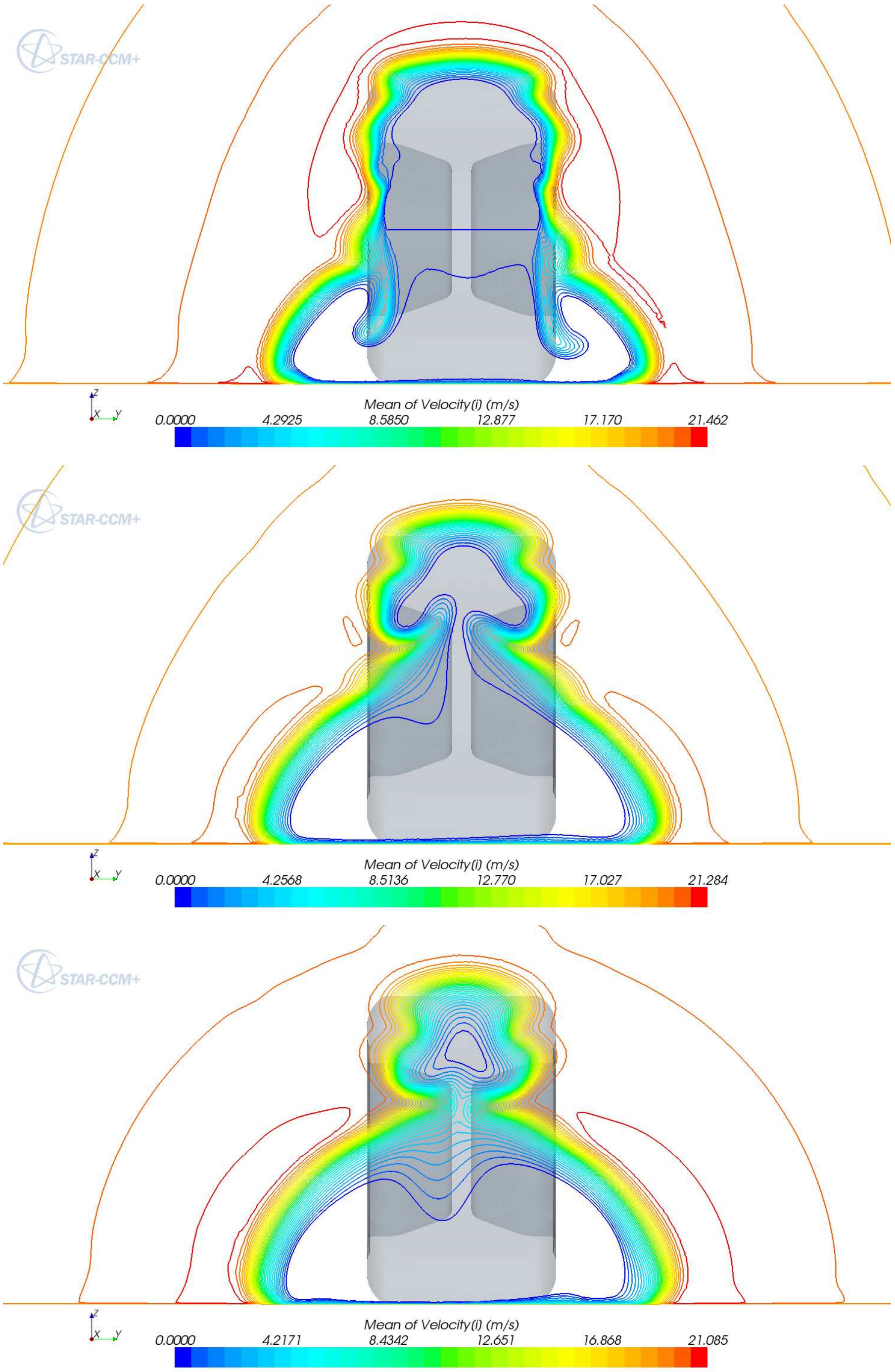

Figure 4.22: Contour mean positive streamwise velocity for K-ω SST. From top to bottom: x = 0.5D , x = 0.75D, x = 1D

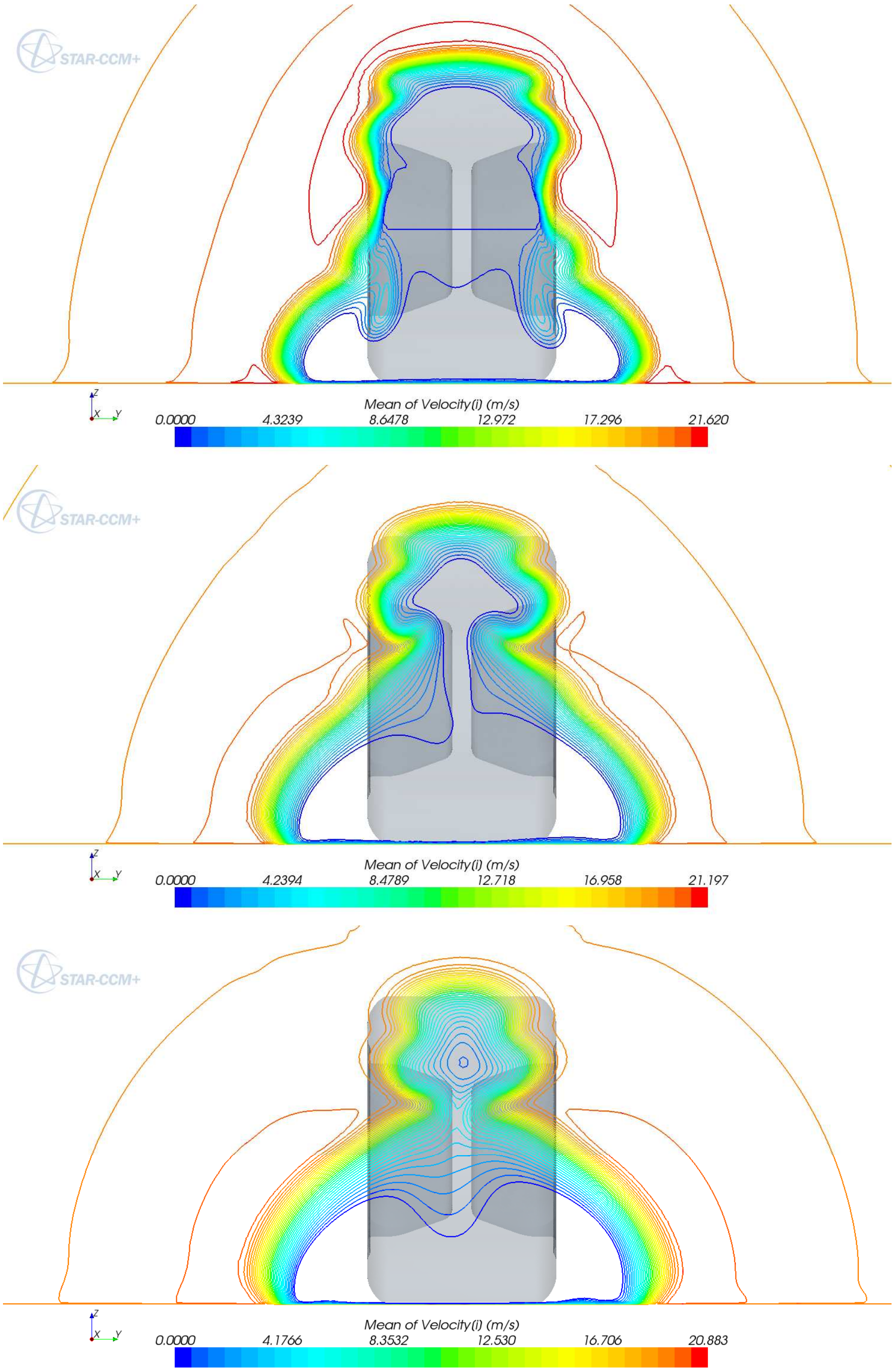

Figure 4.23: Contour mean positive streamwise velocity for Spalart-Allmaras. From top to bottom: x = 0.5D, x = 0.75D, x = 1D

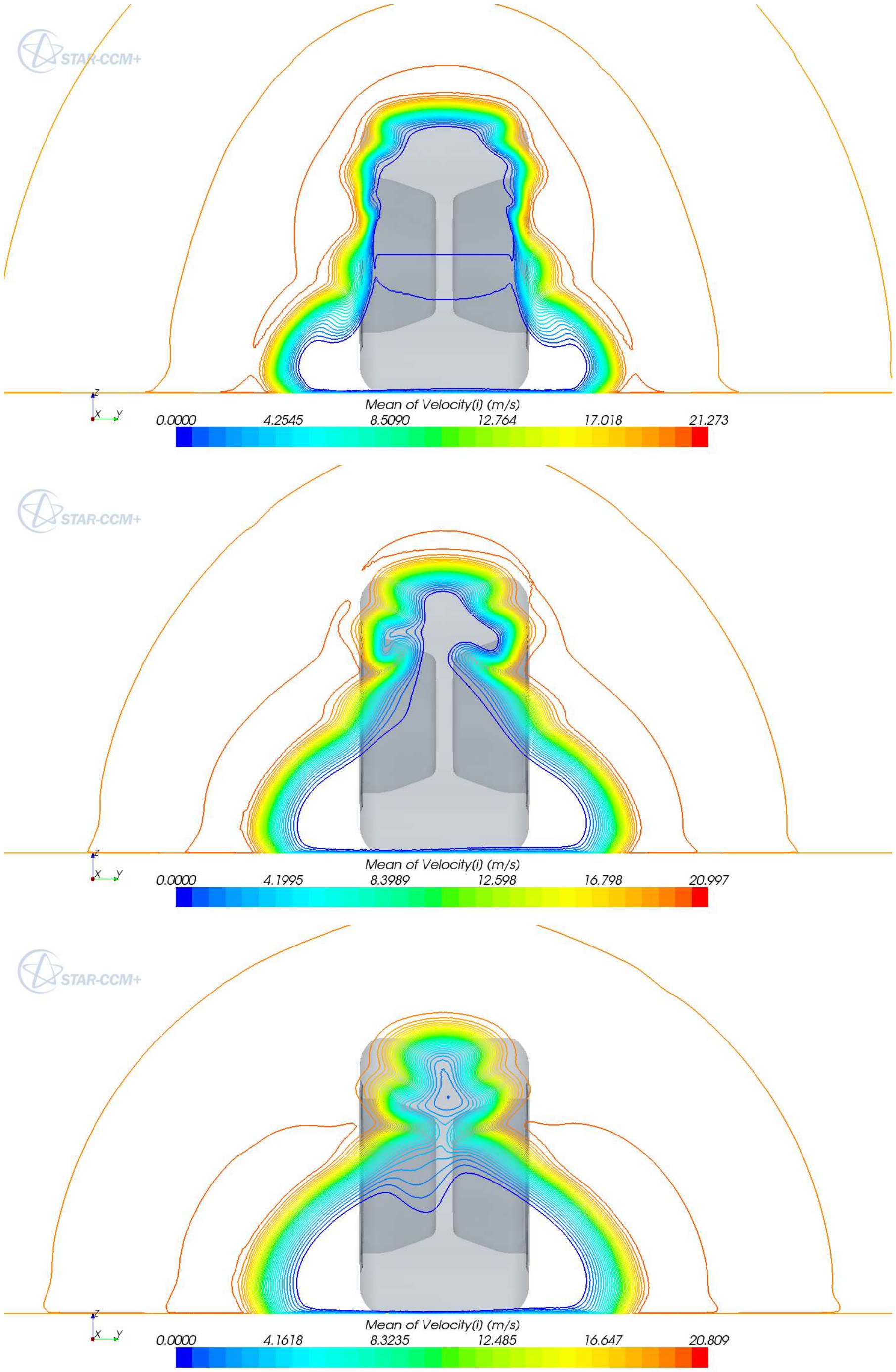

Figure 4.24: Contour mean positive streamwise velocity for Reynolds stress model. From top to bottom: x = 0.5D, x = 0.75D, x = 1D

4.4 Unsteady simulation

Finally, in this section is illustrated the two type of simulation in which the implicit unsteady (URANS) was applied, for the same mesh. The first is a result starting from a steady solution, and it is used the one at this moment provides the best value in term on lift coefficient and drag coefficient. In other words it was used the result of the simulation number 034, using low y+. The latter is a solution using only the initialization of the flow field.

As it can be highlight by Table 4.5, the values of drag and lift coefficient are substantially similar, with slightly improvement as regard the steady restart, as the one found in steady solution; basing only with this data, it could be useful once got a reliable solution in steady conditions, make a refinement simulation in unsteady conditions, in order to make the solution colser to the experimental evidence.

Table 4.5: Number of simulation, drag and lift coefficient with their error from the experimental data

RUN	Cd	%err	Cl	%err
038 steady restart	0.5614	-3.3214	0.4201	-4.5227
039 no steady restart	0.5585	-3.7068	0.4178	-5.0454

In order to follow the same path developed in the entire chapter, Figure 4.25 in next page illustrates the pressure coefficient in centreline as a function of tangential coordinate theta for both the simulations.

It is important to underline that the trend captured from the steady simulation is preserved using it as steady restart, but its peak values in the very first part of the plot have a less amplitude, while the behaviour corresponding to the lower part downstream of the tread isn’t also this time well captured. As regard the unsteady simulation with an only initialization of the fluid the pressure coefficient plot is very similar to the steady one without any improvement as concern the force coefficient.

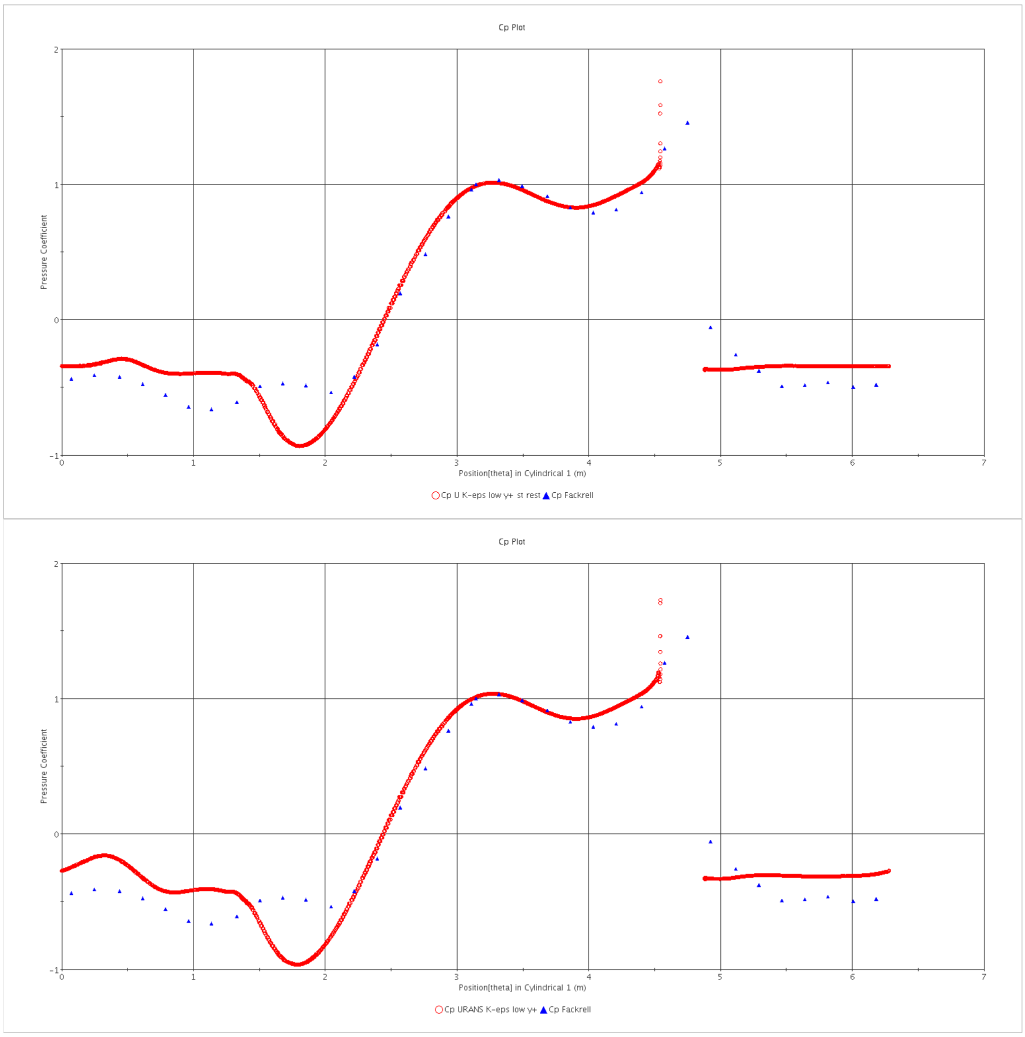

Figure 4.25: Pressure Coefficient in centreline unsteady simulation with steady restart (Top); unsteady simulation without steady restart (Bottom)

In Figure 4.26 is illustrated the values of turbulent viscosity ratio: the simulation with steady restart decays slower respect the other one, which is very similar respect the steady simulation, confirming further what found in the pressure coefficient plot.

In Figure 4.27 the contour of turbulent kinetic energy is described; as anticipated from the previous images, there is a slightly increasing of the values in the simulation with steady restart which it is reflected in a finer gradient of the values, especially in the upper part of the wake. The computational adding efforts seems not to provide a sensible improving, especially from the fact that only the simulation with steady restart allows this result.

In conclusion, the unsteady simulation can provide a better solution only when it is used after being obtained a steady solution and the improvements don't worth the computational efforts.

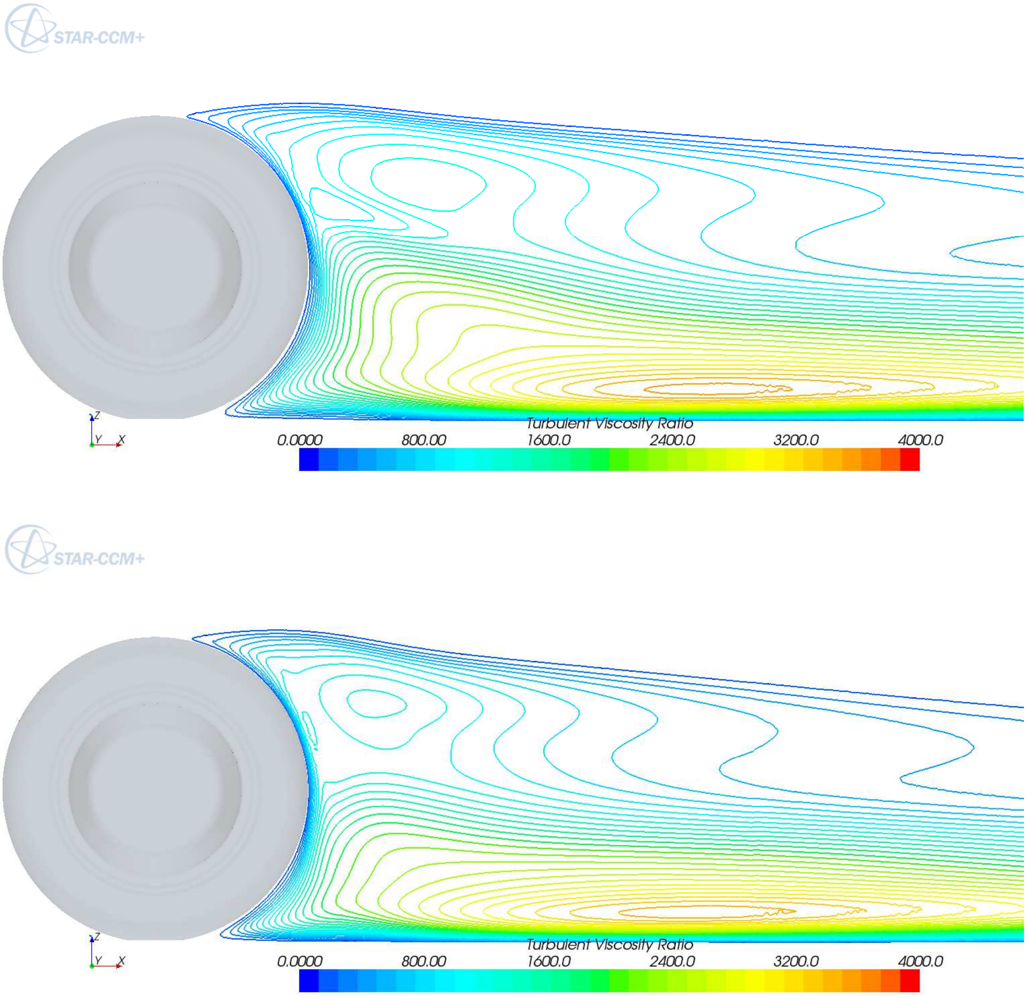

Figure 4.26: Contour of Turbulent viscosity ratio unsteady simulation with steady restart (Top); unsteady simulation without steady restart (Bottom)

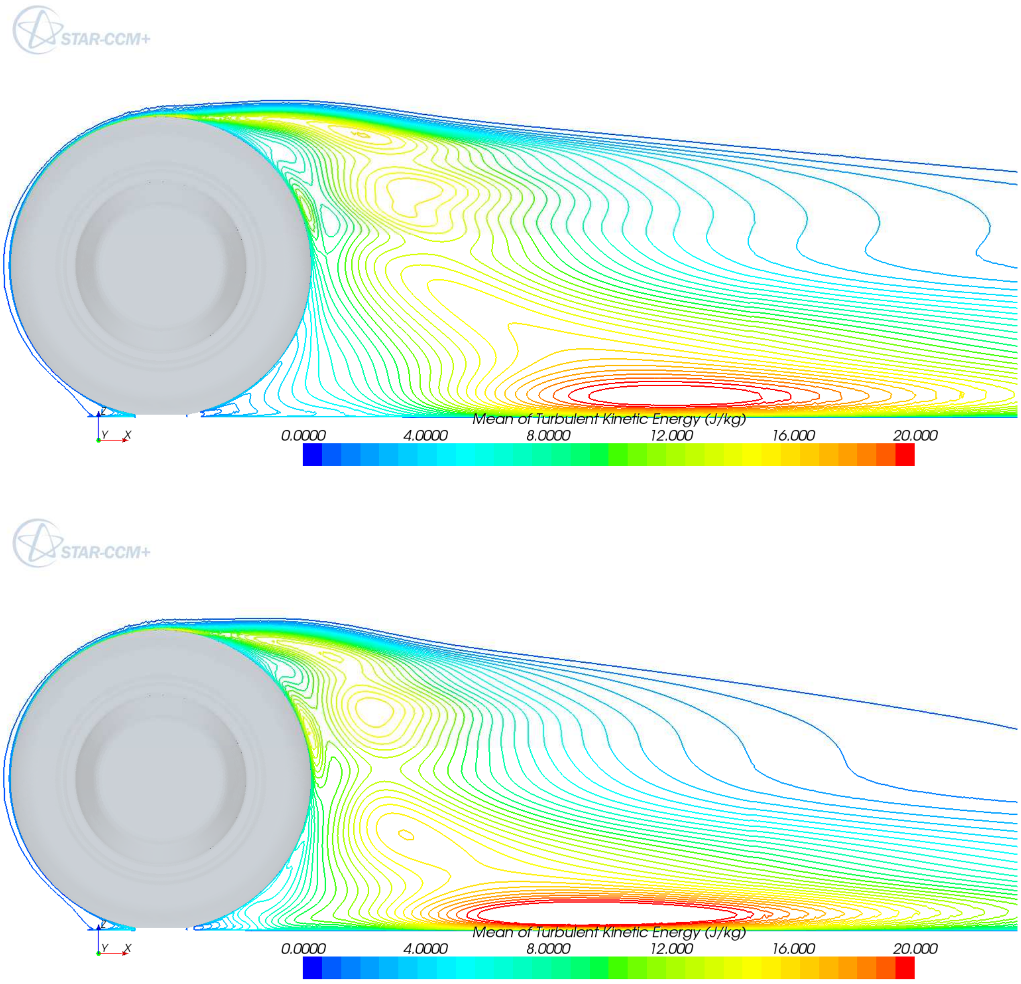

Figure 4.27: Contour of Turbulent kinetic energy unsteady simulation with steady restart (Top); unsteady simulation without steady restart (Bottom)

4.5 Flow features

The aim of this section is to illustrate the shape of the wake in order to provide a contribution to understand better this area that, although it is investigated by several authors for several time, still presents difficulty and obscure sides. The case used for this kind of consideration is the best case in terms of error to the aerodynamic coefficient.

In Figure 4.28 shows the isosurface of the lambda 2 criterion; this kind of parameter delimits the surface of vorticity and best illustrates the shape of the vortex.

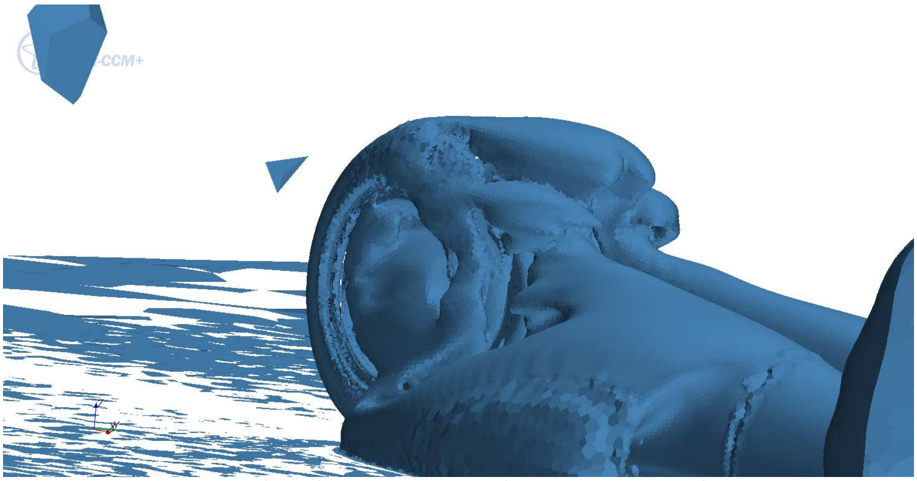

Figure 4.28: Isosurface of lambda 2 criterion for steady simulation for K-ε low y+

As concern the upper separation region the profile of the separated flows forms a couple of vortices, as anticipated of the contour of mean streamwise velocity of Figure 4.20 to 4.24; as also anticipated by the same figure, the upper vortex decays more rapidly than the lower vortex downstream; this supported the Saddigton [22] theory of the two couple of contra rotating vortices, for a length of 1 diameter in streamwise direction, that becomes only the lower couple moving downstream.

As concern the lower separation, the two couple of longitudinal contra rotating vortex spreading widely downstream. In the first part of the streamwise direction is possible to see that this kind of vortex has a bigger diameter, also easy to verify in the contour of mean streamwise velocity; the author argues that this increase of the diameter is due by the contribution given by the contact patch seen in the Figure 4.29; its contribution decays rapidly and the lower vortex changes abruptly the diameter.

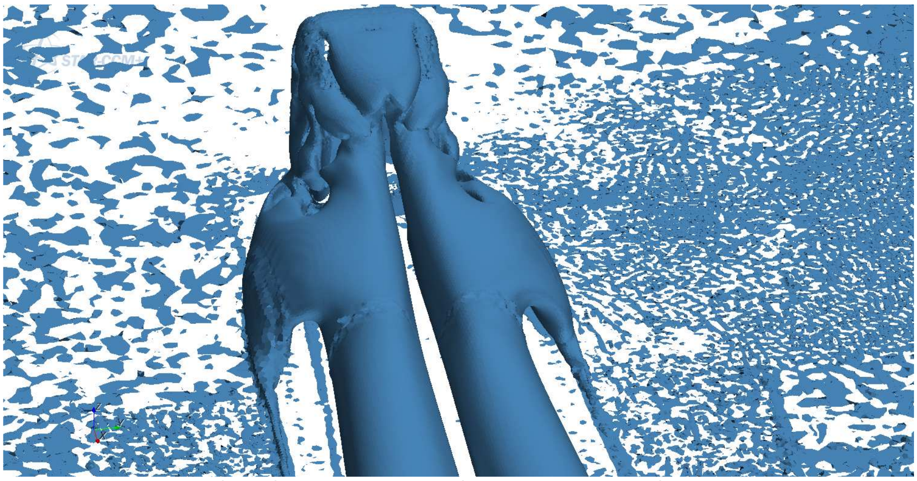

Figure 4.29: Isosurface of lambda 2 criterion for steady simulation for K-ε low y+, top view

It is also important to note that the shape of the rim may give a contribute to the upper vortex; in the latest two figure two vortices leaving the rim seem to provide another couple of vortex set down to the upper separation. The rim vortex is seen in every front mean velocity visualization as the lower lobe presented in the upper contour. The simulation with flow separation on the rim, i.e. turbulent suppression for the first 20° from the stagnation point, is the only without this kind of lobe in the upper vortex.

Streamwise velocity profile

In this subsection the profile of streamwise velocity is plotted as function of the coordinate z; these plot has the aim to visualize the reversed flow zone caused by the tyre. For each streamwise station, the velocity profile of all the turbulence models and also the unsteady simulations are plotted, in order to illustrate how the wake behaves changing turbulence model or switching from steady to unsteady simulation.

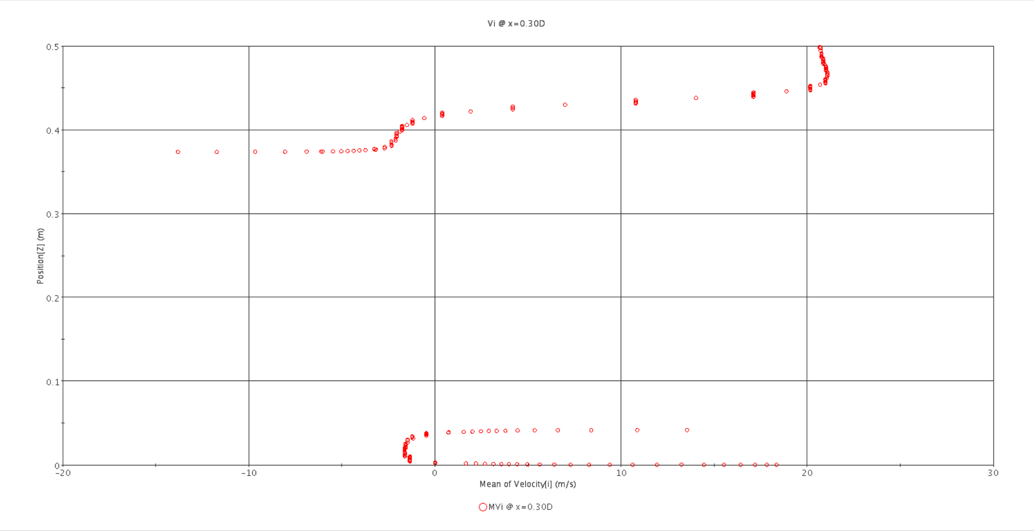
Vi @ x=0.30D
Position[Z] (m)
0.5
0.4
0.3
0.2
0.1
0
-20
-10
0
10
20
30
Mean of Velocity[i] (m/s)
○MVi @ x=0.30D

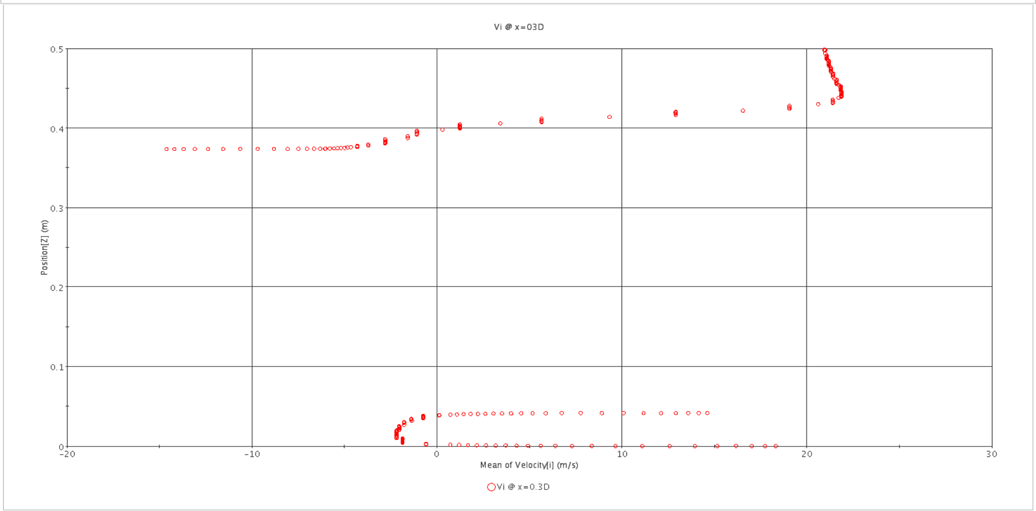
Vi @ x=03D
Position[Z] (m)
0.5
0.4
0.3
0.2
0.1
0
-20
-10
0
10
20
30
Mean of Velocity[i] (m/s)
○Vi @ x=0.3D

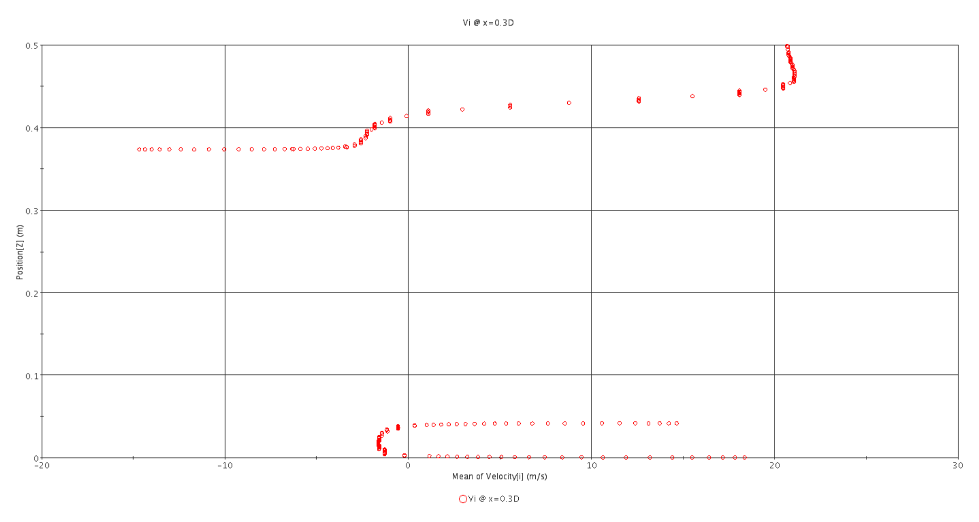
Vi @ x=0.3D
Position[Z] (m)
0.5
0.4
0.3
0.2
0.1
0
-20
-10
0
10
20
30
Mean of Velocity[i] (m/s)
○Vi @ x=0.3D

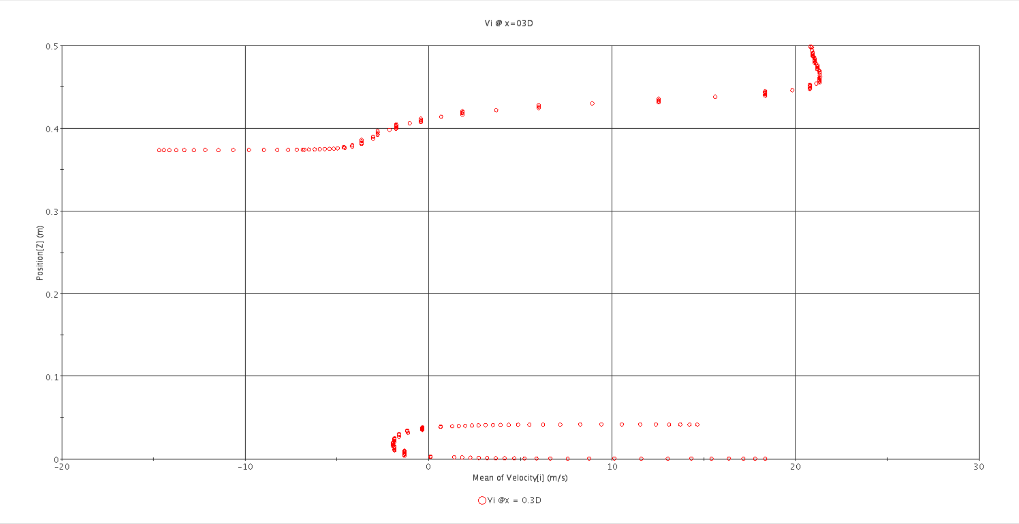
Vi @ x=03D
0.5
0.4
0.3
0.2
0.1
0
Position[Z] (m)
-20
-10
0
10
20
30
Mean of Velocity[i] (m/s)
○Vi @x = 0.3D

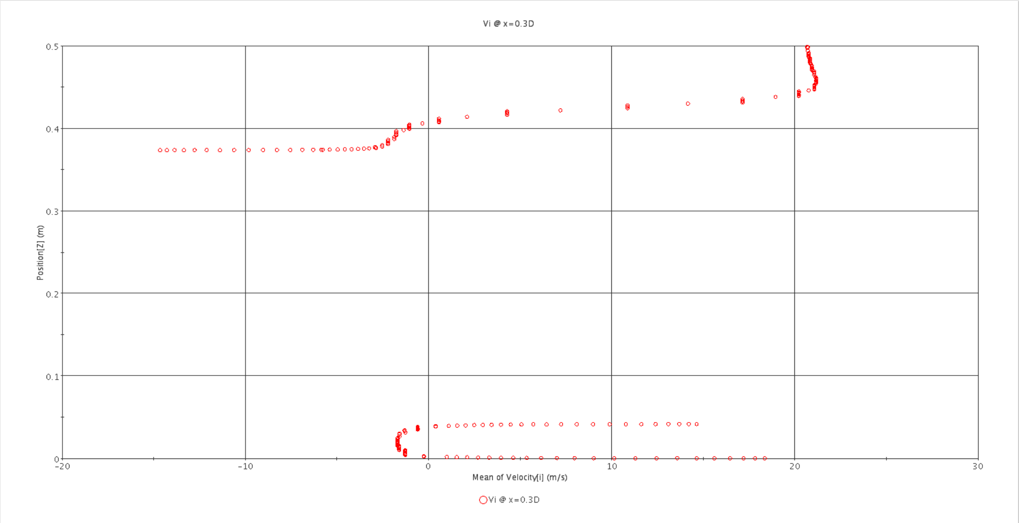
Vi @ x=0.3D
0.5
0.4
0.3
0.2
0.1
0
Position[Z] (m)
-20
-10
0
10
20
30
Mean of Velocity[i] (m/s)
○Vi @ x=0.3D

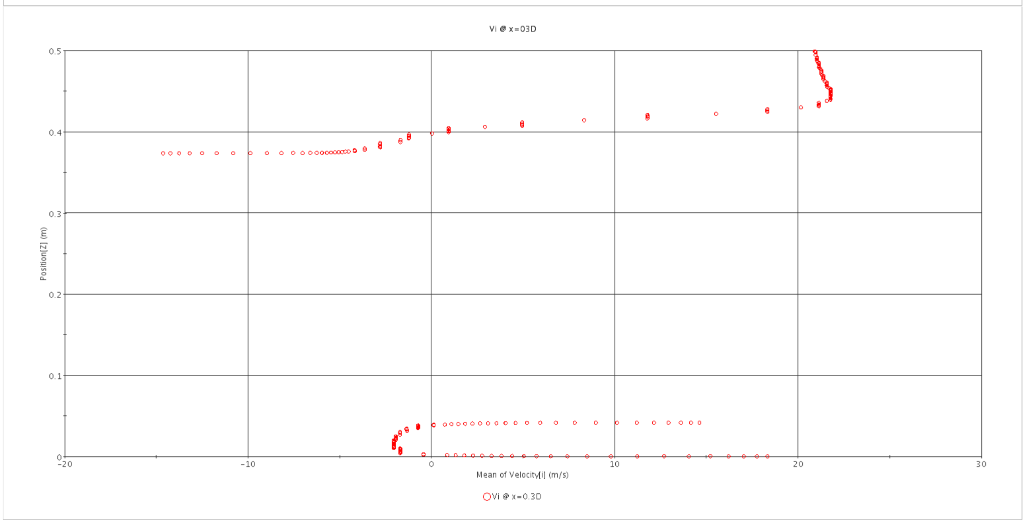
Vi @ x=03D
0.5
0.4
0.3
0.2
0.1
0
Position[Z] (m)
-20
-10
0
10
20
30
Mean of Velocity[i] (m/s)
○Vi @ x=0.3D

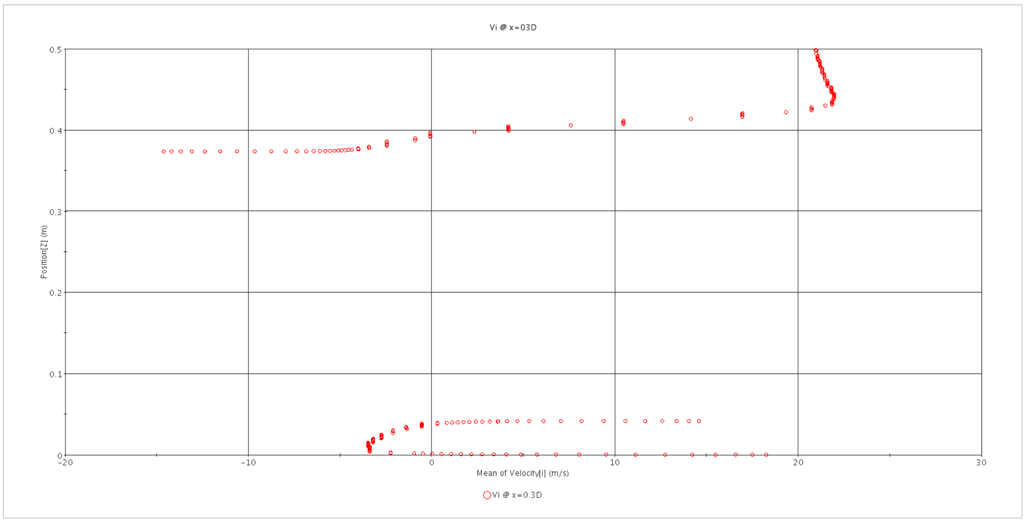

Figure 4.30: Mean positive streamwise velocity as function of z at x=0.35D. From top to bottom: K-ε all y+, K-ε low y+, K-ω SST, Spalart-Allmaras, Reynolds stress model unsteady with steady restart, unsteady without steady restart

The first Figure, 4.30, are the profiles taken in centreline at a streamwise location of 0.35D; the sequence of the plot reflects faithfully the order used to present the results in this chapter, as also all the next figures.

Common features of every plot in this figure are the step in the upper part of the profile, approximately at 1D in height, position where the shear velocity profile is affected also by the rotation of the tyre, and the reversed flow occurs in the contact patch. The step are smoother for K-ε low y+ and Spalart Allmaras, while is sharp for the others.

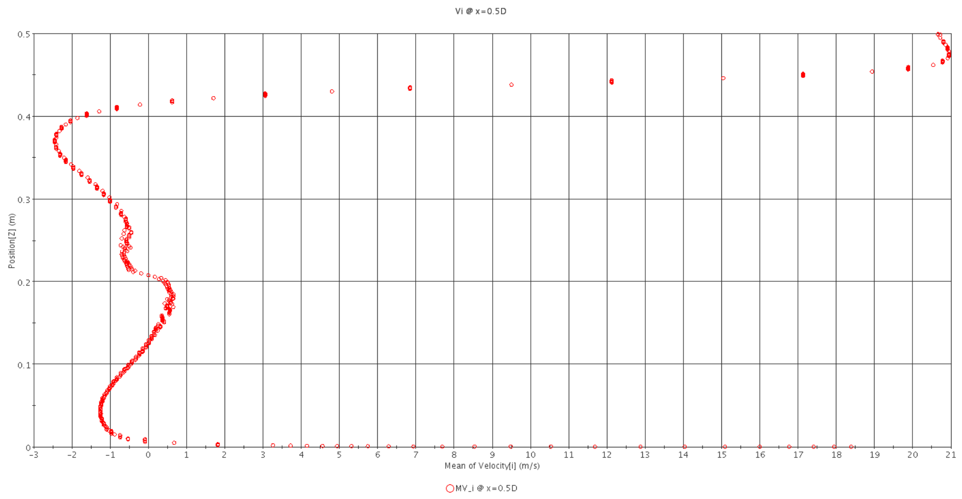
Vi @ x=0.5D
0.5
0.4
0.3
0.2
0.1
0
Position[Z] (m)
-3
-2
-1
0
1
2
3
4
5
6
7
8
9
10
11
12
13
14
15
16
17
18
19
20
21
Mean of Velocity[i] (m/s)
○MV_i @ x=0.5D

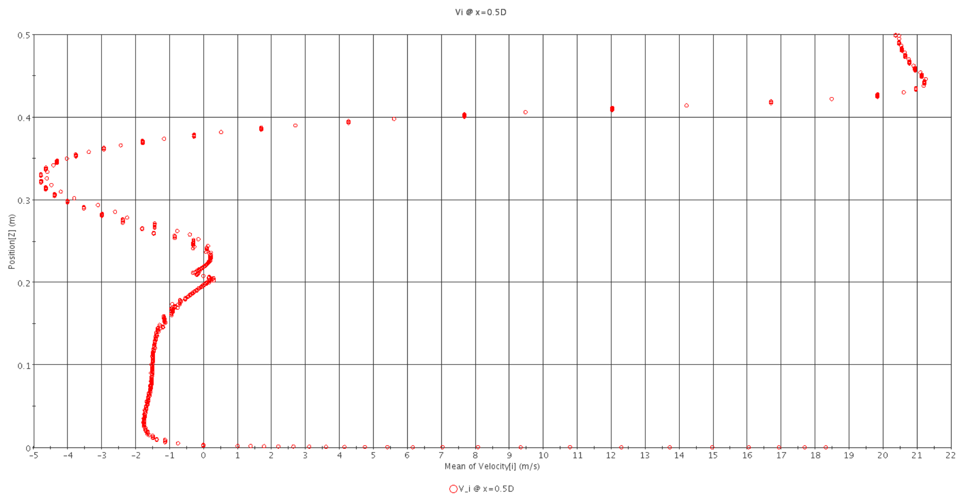
Vi @ x=0.5D
0.5
0.4
0.3
0.2
0.1
0
Position[Z] (m)
-5
-4
-3
-2
-1
0
1
2
3
4
5
6
7
8
9
10
11
12
13
14
15
16
17
18
19
20
21
22
Mean of Velocity[i] (m/s)
○V_i @ x=0.5D

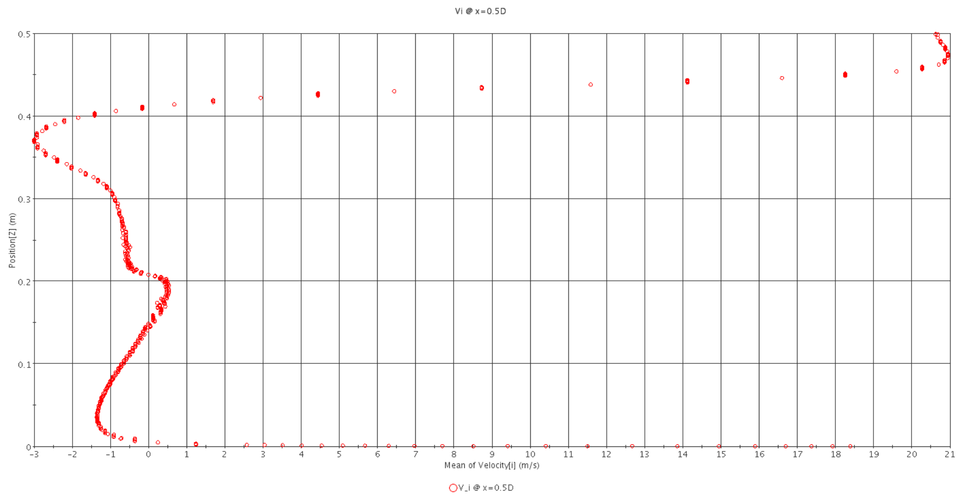
Vi @ x=0.5D
0.5
0.4
0.3
0.2
0.1
0
Position[Z] (m)
-3
-2
-1
0
1
2
3
4
5
6
7
8
9
10
11
12
13
14
15
16
17
18
19
20
21
Mean of Velocity[i] (m/s)
○V_i @ x=0.5D

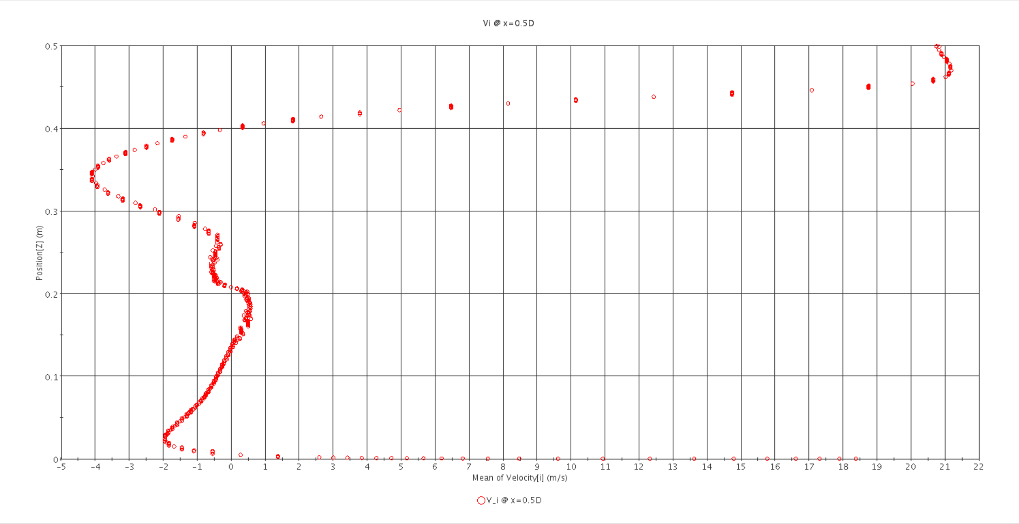
Vi @ x=0.5D
Position[Z] (m)
0.5
0.4
0.3
0.2
0.1
0
-5 -4 -3 -2 -1 0 1 2 3 4 5 6 7 8 9 10 11 12 13 14 15 16 17 18 19 20 21 22
Mean of Velocity[i] (m/s)
V_i @ x=0.5D

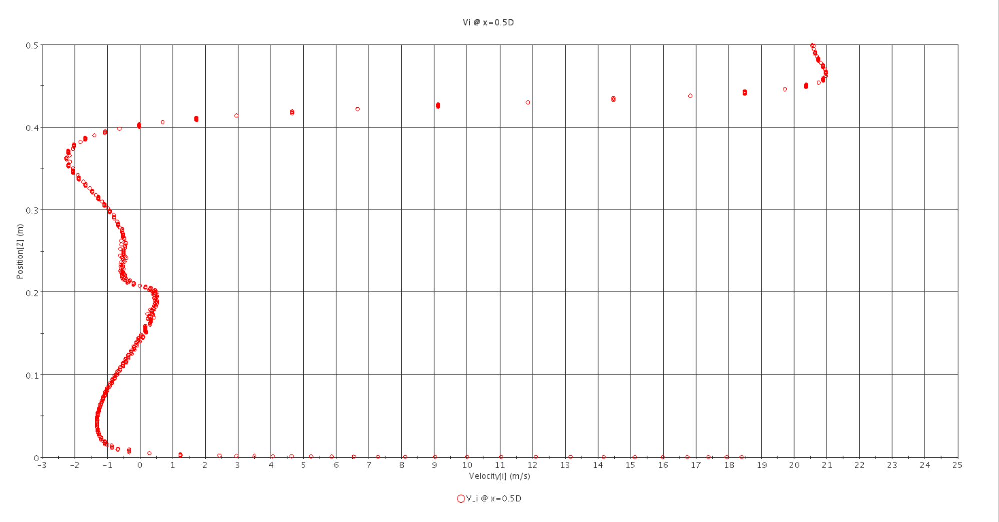
Vi @ x=0.5D
Position[Z] (m)
0.5
0.4
0.3
0.2
0.1
0
-3 -2 -1 0 1 2 3 4 5 6 7 8 9 10 11 12 13 14 15 16 17 18 19 20 21 22 23 24 25
Velocity[i] (m/s)
V_i @ x=0.5D

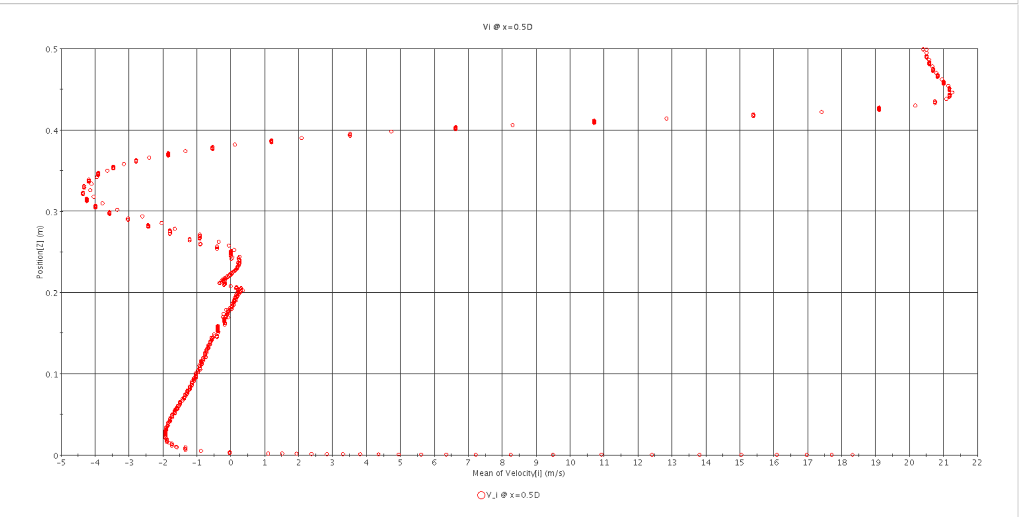
Vi @ x=0.5D
Position[Z] (m)
0.5
0.4
0.3
0.2
0.1
0
-5 -4 -3 -2 -1 0 1 2 3 4 5 6 7 8 9 10 11 12 13 14 15 16 17 18 19 20 21 22
Mean of Velocity[i] (m/s)
V_i @ x=0.5D

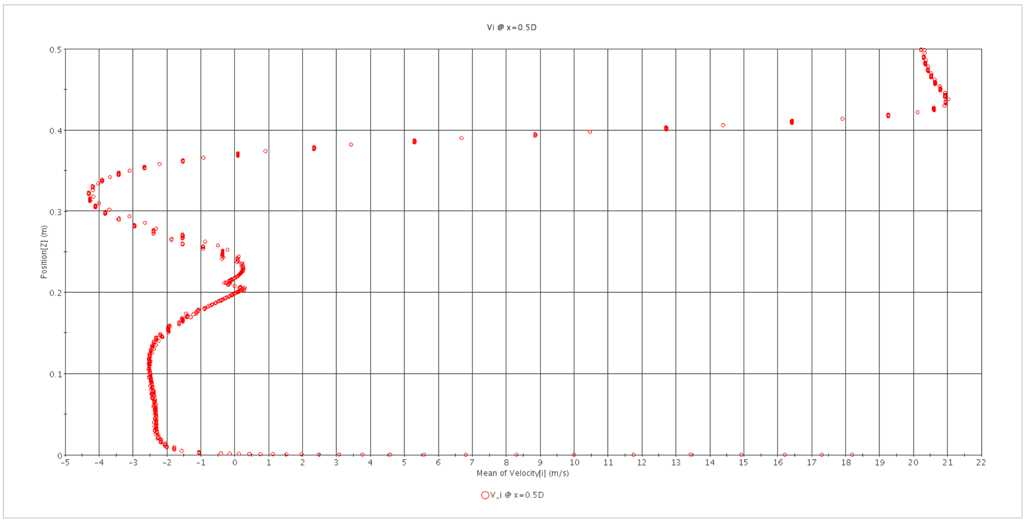

Figure 4.31: Mean positive streamwise velocity as function of z at x=0.5D . From top to bottom: K-ε all y+, K-ε low y+, K-ω SST, Spalart-Allmaras, Reynolds stress model, unsteady with steady restart, unsteady without steady restart

Figure 4.31, are the profiles taken in centreline at a streamwise location of 0.5D. It is important to emphasize that the upper recirculation has two lobes; K-ε low y+ is the only one that presents a positive profile for the smaller one and more close to the center. His peak negative value is down respect the other and this led to a shorter wake respect the other.

As regard the lower recirculation, K-ε low y+ presents the most constant profile, while the others present a sharp adverse gradient near ground.

As previous, unsteady simulation doesn't provide sensible improvement.

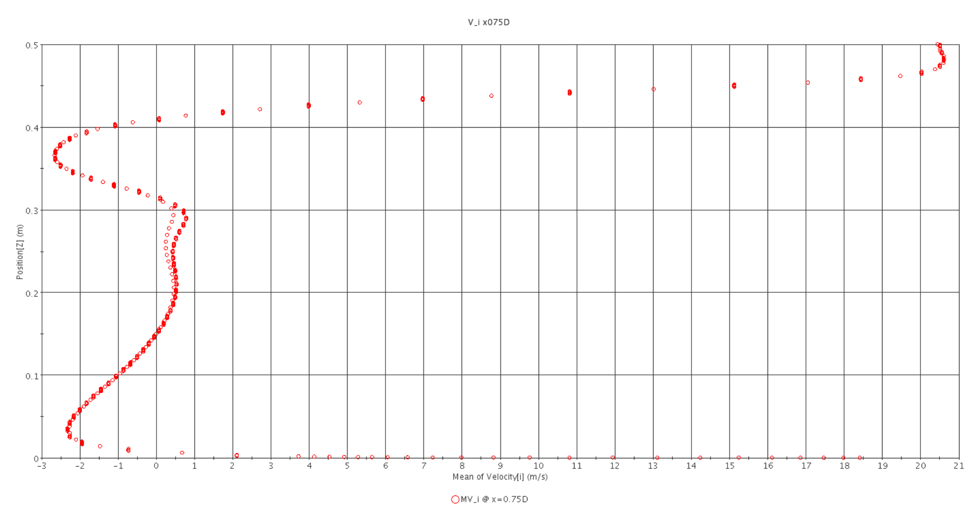
V_i x075D
Position[Z] (m)
0.5
0.4
0.3
0.2
0.1
0
-3 -2 -1 0 1 2 3 4 5 6 7 8 9 10 11 12 13 14 15 16 17 18 19 20 21
Mean of Velocity[i] (m/s)
MV_i @ x=0.75D

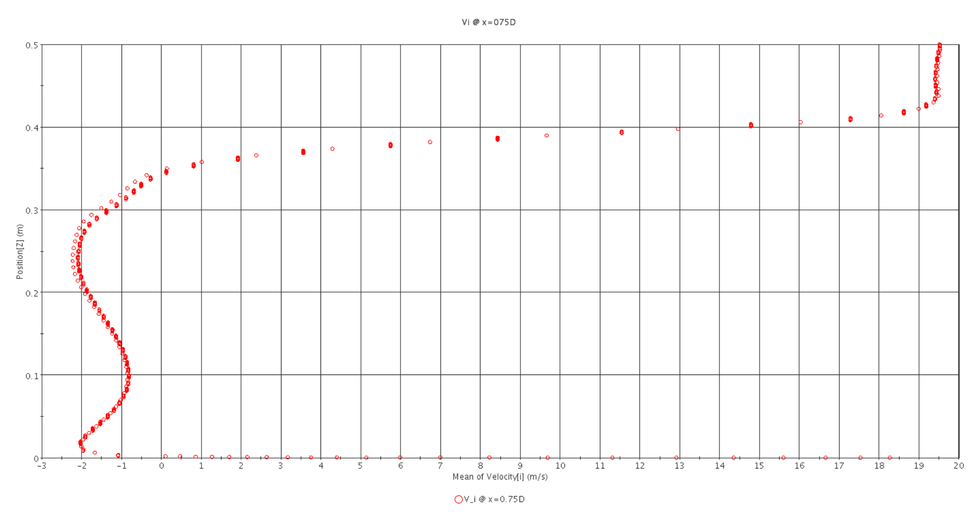
Vi @ x=075D
Position[Z] (m)
0.5
0.4
0.3
0.2
0.1
0
-3 -2 -1 0 1 2 3 4 5 6 7 8 9 10 11 12 13 14 15 16 17 18 19 20
Mean of Velocity[i] (m/s)
V_i @ x=0.75D

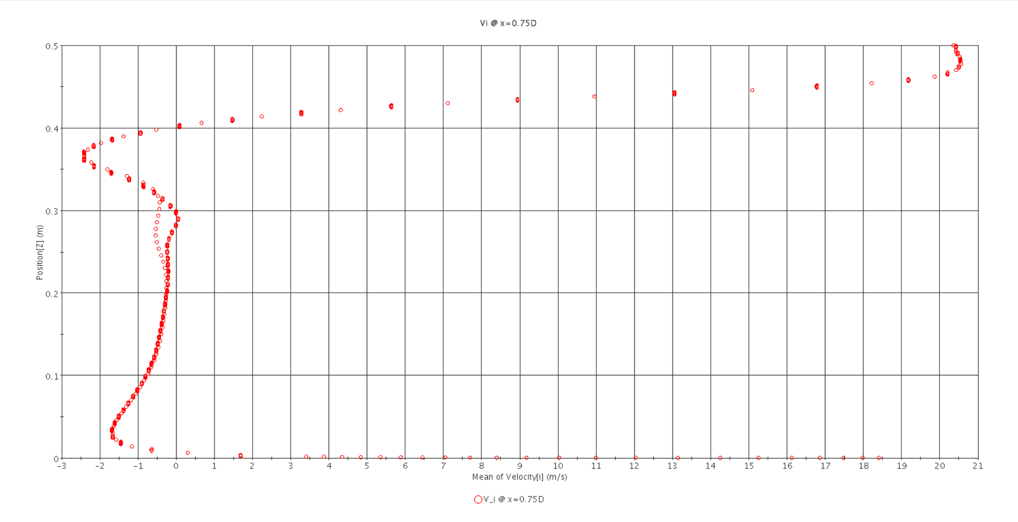
Vi @ x=0.75D
Position[Z] (m)
0.5
0.4
0.3
0.2
0.1
0
-3 -2 -1 0 1 2 3 4 5 6 7 8 9 10 11 12 13 14 15 16 17 18 19 20 21
Mean of Velocity[i] (m/s)
V_i @ x=0.75D

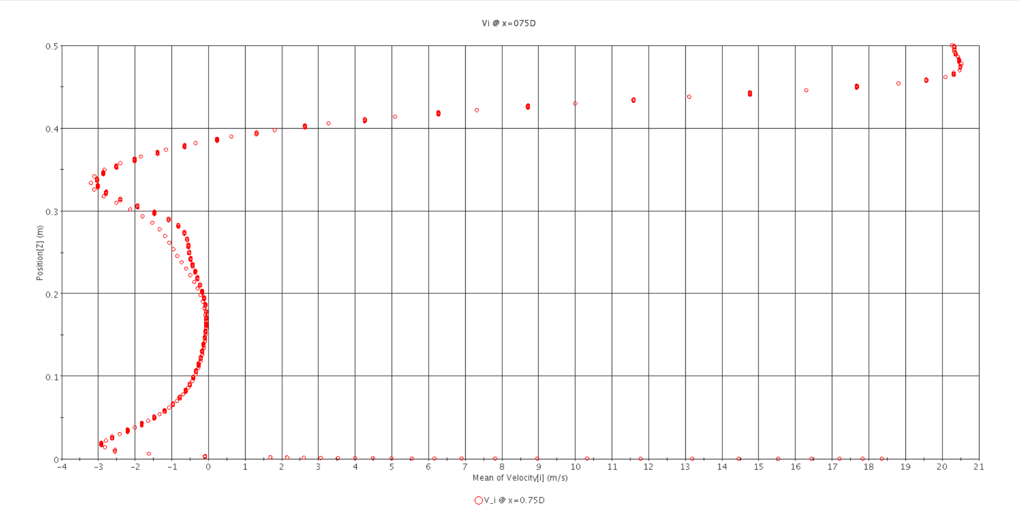
Vi @ x=075D
Position[Z] (m)
0.5
0.4
0.3
0.2
0.1
0
−4 −3 −2 −1 0 1 2 3 4 5 6 7 8 9 10 11 12 13 14 15 16 17 18 19 20 21
Mean of Velocity[i] (m/s)
○V_i @ x=0.75D

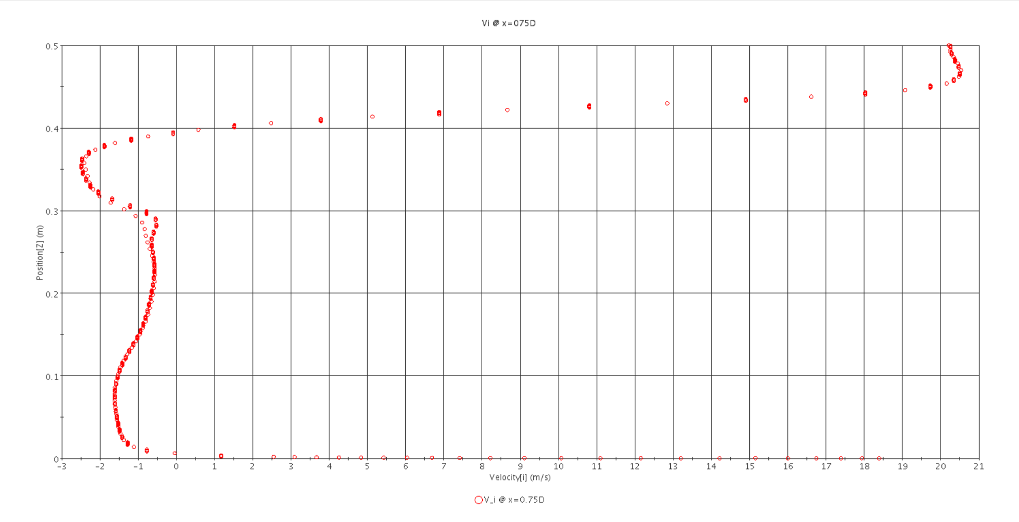
Vi @ x=075D
Position[Z] (m)
0.5
0.4
0.3
0.2
0.1
0
−3 −2 −1 0 1 2 3 4 5 6 7 8 9 10 11 12 13 14 15 16 17 18 19 20 21
Velocity[i] (m/s)
○V_i @ x=0.75D

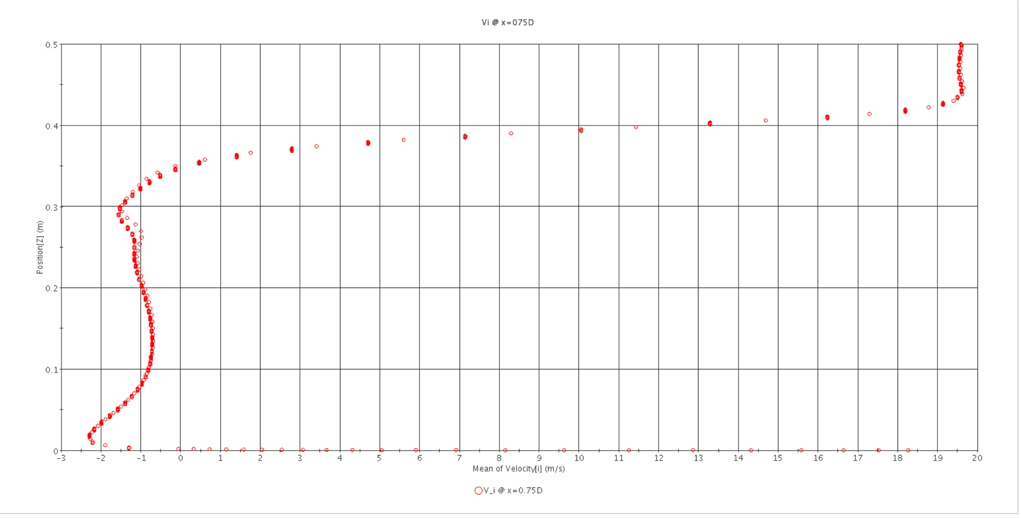
Vi @ x=075D
Position[Z] (m)
0.5
0.4
0.3
0.2
0.1
0
−3 −2 −1 0 1 2 3 4 5 6 7 8 9 10 11 12 13 14 15 16 17 18 19 20
Mean of Velocity[i] (m/s)
○V_i @ x=0.75D

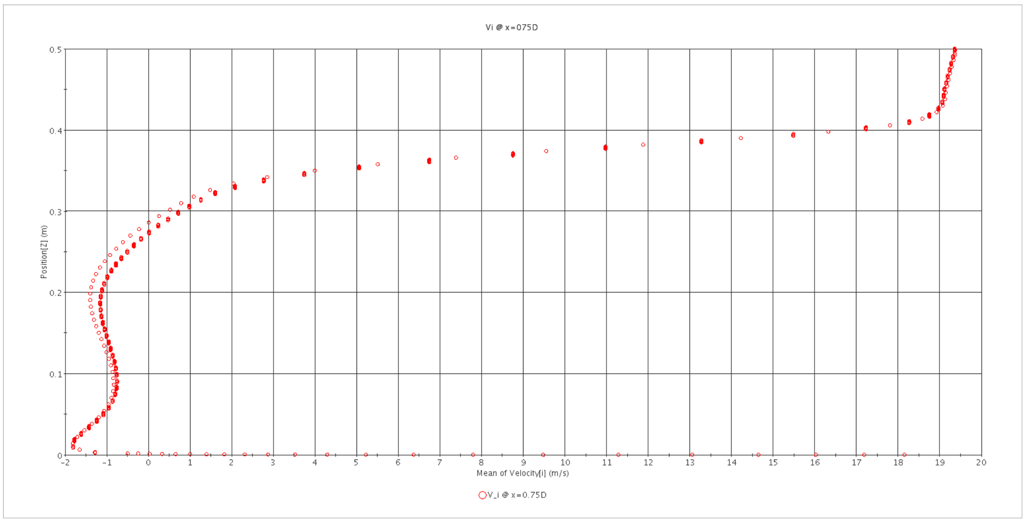

Figure 4.32: Mean positive streamwise velocity as function of z at x=0.75D . From top to bottom: K-ε all y+, K-ε low y+, K-ω SST, Spalart-Allmaras, Reynolds stress model, unsteady with steady restart, unsteady without unsteady restart

Figure, 4.32, are the profiles taken in centreline at a streamwise location of 0.75D. The shape are very similar, apart from the K-ε low y+ and the unsteady simulations; all the plot presents an almost peak negative value.

By the contrary, the upper vortex is different changing turbulence model, sharp or rounded, changing turbulence model.

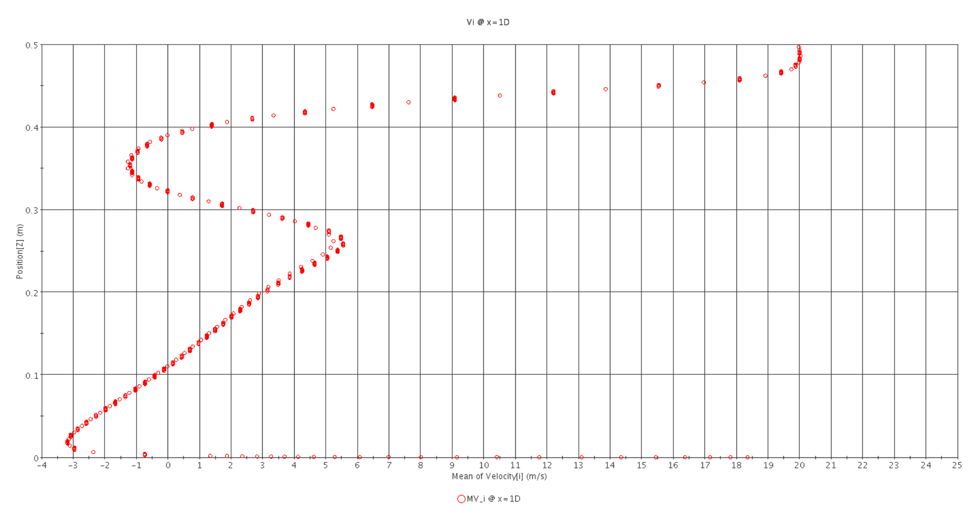
Vi @ x=1D
Position[Z] (m)
0.5
0.4
0.3
0.2
0.1
0
-4 -3 -2 -1 0 1 2 3 4 5 6 7 8 9 10 11 12 13 14 15 16 17 18 19 20 21 22 23 24 25
Mean of Velocity[i] (m/s)
○MV_i @ x=1D

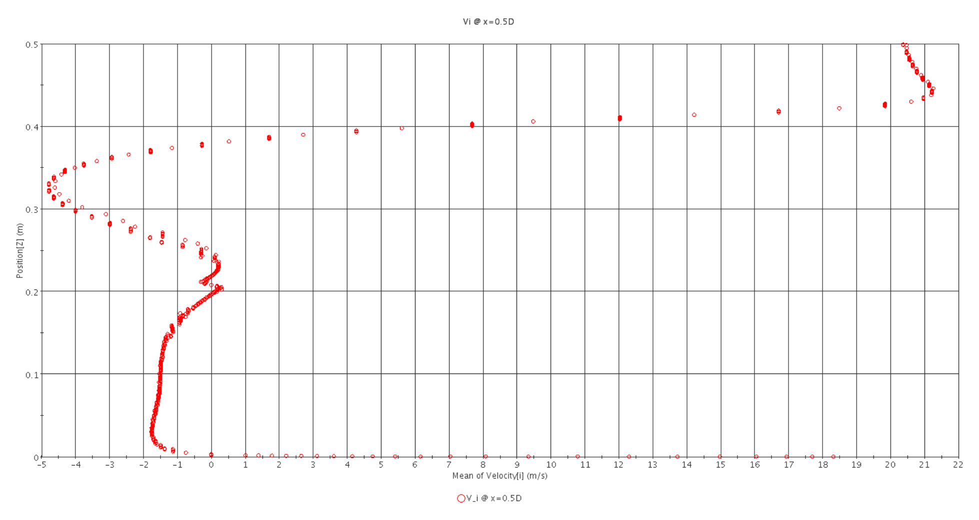
Vi @ x=0.5D
Position[Z] (m)
0.5
0.4
0.3
0.2
0.1
0
-5 -4 -3 -2 -1 0 1 2 3 4 5 6 7 8 9 10 11 12 13 14 15 16 17 18 19 20 21 22
Mean of Velocity[i] (m/s)
○V_i @ x=0.5D

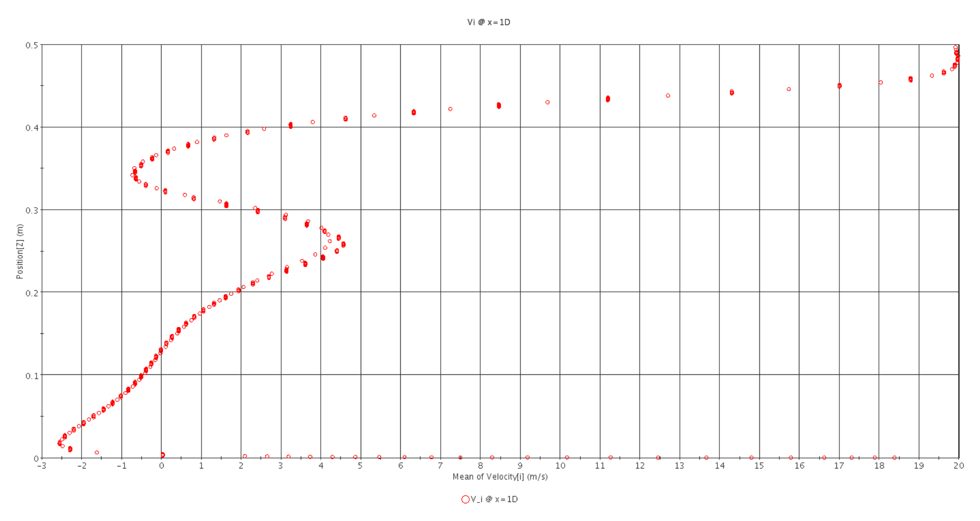
Vi @ x=1D
Position[Z] (m)
0.5
0.4
0.3
0.2
0.1
0
-3 -2 -1 0 1 2 3 4 5 6 7 8 9 10 11 12 13 14 15 16 17 18 19 20
Mean of Velocity[i] (m/s)
○V_i @ x=1D

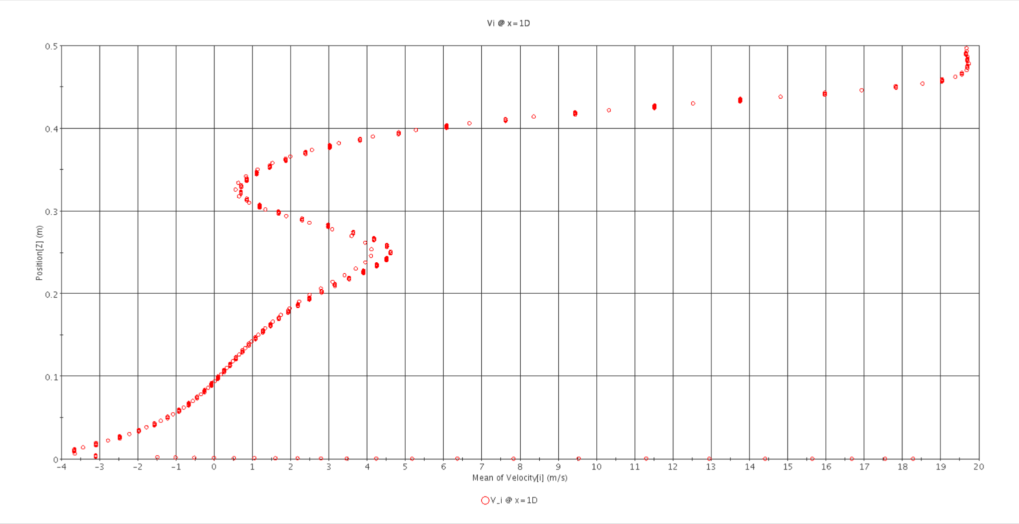
Vi @ x=1D
Position[Z] (m)
0.5
0.4
0.3
0.2
0.1
0
-4 -3 -2 -1 0 1 2 3 4 5 6 7 8 9 10 11 12 13 14 15 16 17 18 19 20
Mean of Velocity[i] (m/s)
○ V_i @ x=1D

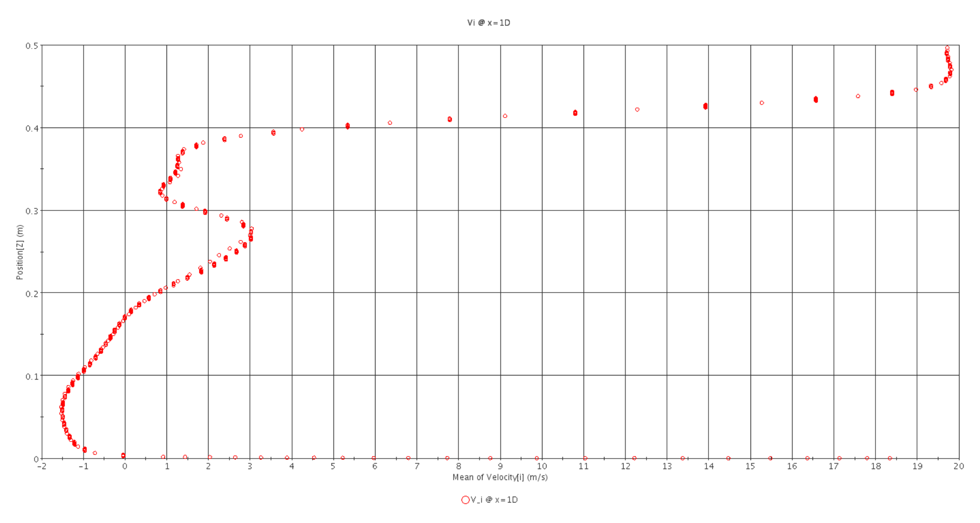
Vi @ x=1D
Position[Z] (m)
0.5
0.4
0.3
0.2
0.1
0
-2 -1 0 1 2 3 4 5 6 7 8 9 10 11 12 13 14 15 16 17 18 19 20
Mean of Velocity[i] (m/s)
○ V_i @ x=1D

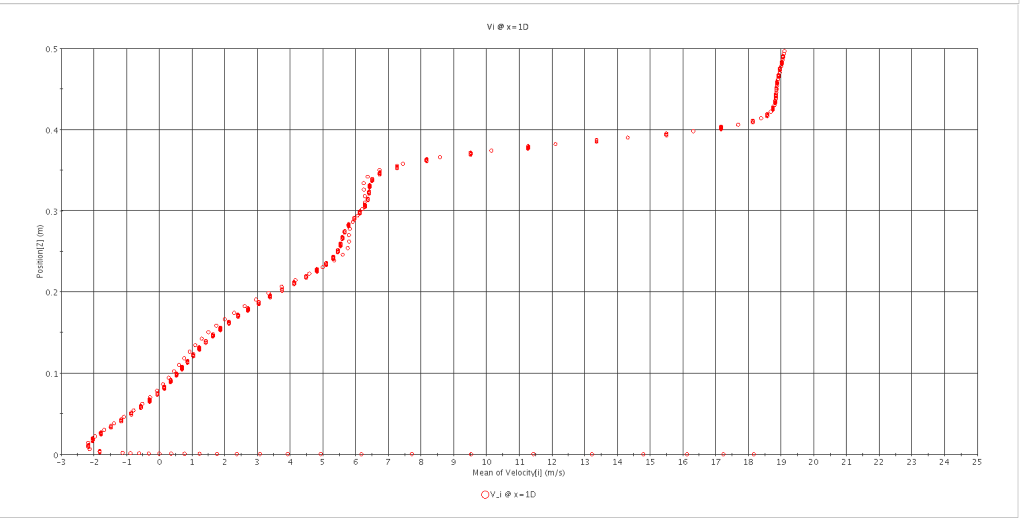
Vi @ x=1D
Position[Z] (m)
0.5
0.4
0.3
0.2
0.1
0
-3 -2 -1 0 1 2 3 4 5 6 7 8 9 10 11 12 13 14 15 16 17 18 19 20 21 22 23 24 25
Mean of Velocity[i] (m/s)
○ V_i @ x=1D

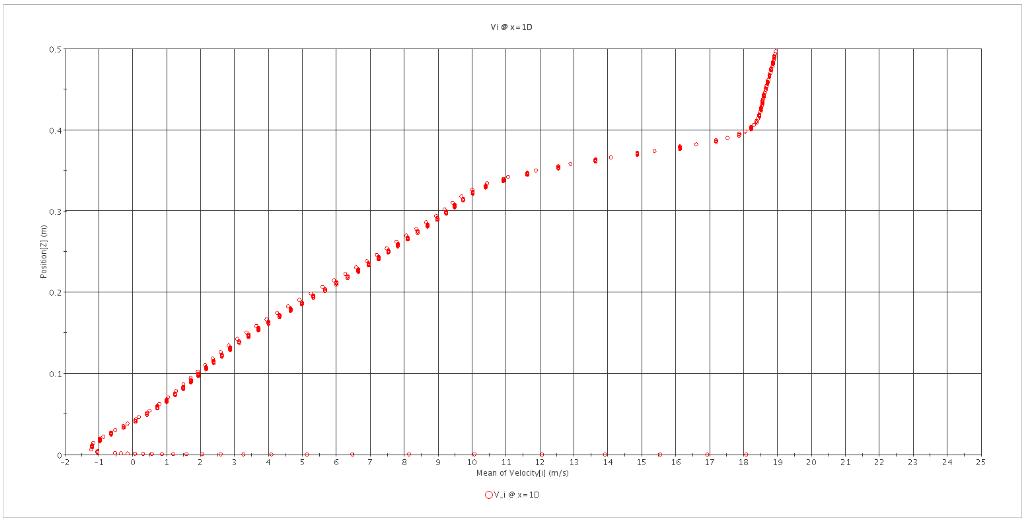

Figure 4.33: Mean positive streamwise velocity as function of z at x=1D. From top to bottom: K-ε all y+, K-ε low y+, K-ω SST, Spalart-Allmaras, Reynolds stress model, unsteady with steady restart, unsteady without unsteady restart

Figure, 4.33, are the profiles taken in centreline at a streamwise location of 1D. It can be seen as some profile have sharp shear as K-ε all y+, Spalart-Allmaras, or rounded for K-ε low y+ and Reynolds Stress Model.

The lower part is different for every type of model choice, but although the tyre is relatively away, it can be seen part of reversed flow, witnessed the fact that the wake isn’t vanished yet.

Chapter

5

Conclusions

The present work deals with an investigation of the flow around an isolated tyre using CFD commercial code and an unstructured mesh to describe the domain. In order to compare the numerical results with experimental data, the B2 Fackrell’s wheel has been used, due to the amount of reliable data available for it. The first part of the job was to achieve a meshing setup as most insensitive as possible, with the lowest number of cells. The second part was the identification of the best turbulence model, wall function or turbulent suppression, which matches the experimental data, especially regarding the centerline pressure distribution. The unsteady simulation – with and without a steady restart – has been executed in order to achieve some improvements. In the end, a new model for the tyre wake was presented, together with the streamwise velocity distribution in some downstream stations.

5.1 Meshing conclusions

The problem of estimating the lift coefficient with a good level of accuracy is exacerbated by the wrong identification of the separation point position: the CFD code predicts the separation to occur earlier than in the reality. The calculation of the drag coefficient returned acceptable values when using a different ratio of elements on the ground and on the tyre (respectively 1:2); raising this ratio, in order to resolve properly the viscous sublayer on the tyre, led to problems of wide fluctuations and bad convergence.

Concerning the convergence, the residuals plot show that the finest mesh has drastically reduced fluctuations, led to more acceptable results in term of force coefficient and allowed a quicker convergence towards a constant value.

The use of double the number of prisms on the tyre with respect to the discretisation of the ground allows to better resolve the part of the flow closely surrounding the tyre, and led to a smoother velocity profile; the upper vortex – detaching from the tyre – results more squeezed using the same number of prism on the ground and it diffuses more in the flow field.

The pressure distribution on the centerline isn’t affect by the variation of meshing parameters in a sensible way, and it is shifted downstream with respect to the experimental data.

5.2 Turbulence models conclusions

Before investigating the most famous turbulence models behavior, two simulations using turbulence suppression have been executed, according to the observations made by Fackrell in his job: the first simulation, uses turbulence suppression for the first 20°, while the second prevents separation for occurring in the first 80°, measured from the stagnation point. The results of the first analysis present different values of lift and drag coefficient, due to the separation occurring in the wheel rim; the second simulation presents the same trend of the aforementioned results. Regarding the velocity profile, the shear leaving the tyre tread in the first simulation is higher than in the second case, and the value of turbulent viscosity ratio has a peak; this in turn led to a higher vertical dimension in the lower vortex. In the aforementioned simulation, due to the separation occurring on the rim, the shape of the velocity shear becomes different from all the other simulations; this is reckoned by the author a non-physical result, since the Fackrell’s jetting phenomena isn’t present, in contrast with what occurs in the other simulations, not only in this work, but also in the literature.

The use of turbulence suppression involves a reduction in the production of turbulent kinetic energy, which in turn causes the rapid decay of the vortex and the less diffusivity in the flow field, as witnessed by the contour of stream velocity profile.

Additional simulations are executed, by keeping the meshing parameters frozen and changing turbulence models. From the results, it is evident how all the turbulence models used, representative of the standard used in the industrial environment, underestimate the main coefficient of force, lift and drag. The model which produces results closest to the experimental data is K- ε low y +, with an error respect lift coefficient of the same order of magnitude as the drag coefficient.

An analysis of the pressure coefficient in the centreline shows evidently how fully resolving the viscous sublayer allows for secondary trend to be captured, but the separation point occurs always downstream and the K-ω SST presents the closest value with respect to the experimental data. Surprisingly, the Spalart-Allmaras model produces results comparable in terms of force coefficient and pressure distribution to those of a two-equations model, with remarkable savings in terms of computational effort. Another important result is that no turbulence model, from the easy one-equation Spalart-Allmaras to the complete Reynolds Stress Model, is able to describe correctly the behaviour of the pressure in the bottom part of the tread located downstream.

Investigating how the turbulence model affects the flow field allows drawing some considerations. The difference in the wall treatment is reflected in the smaller thickness of the turbulent viscous layer, which leads to an upper vortex less diffused on the flow. The K-ε model, with both wall treatment, presents the highest value of turbulent viscosity, while the K-ω SST model has gradients near the wall comparable to those obtained with the Reynolds Stress model; far downstream, in the upper part, the results are is comparable with K-ε one. This confirms how the model was built: a K-ε model away from the wall and a K-ω model near the wall. Spalart-Allmaras method has smoother gradient near the tyre tread, especially in the zone near contact patch. The distribution of turbulent viscosity in the upper part is more similar to the K-ε all y+, and the thickness of the turbulent region increases moving downstream, witnessing the high diffusivity of the single-equation scheme. In the end, Reynolds Stress model presents similarity to K-ε low y+ in the very first upper part, while close to the centreline the shear is smoother as with the K-ω method. The presence of the ground is better captured by the K-ε models.

Inquiring deeply, therefore studying the main actors of the modelling equations, turbulent kinetic energy and turbulent dissipation rate, it is found that the high level of both values holds the turbulent viscosity almost constant in the very first part of the upper flow stream, for in the case of the K-ε all y+ model. Moving downstream, the dissipation value fades, while the shear of the kinetic energy remains almost constant, and this leads to an increase of the turbulent viscosity, as seen before. Changing only the wall treatment translates in a relevant variation of the turbulent kinetic energy, while the core seen in the K-ε all y+ model in the upper region can be attributed to the particular wall treatment used. The reason of the rapid decay of the upper tyre wake is found in the values of turbulent dissipation rate on the wheel tread, smooth in the low y+, and sharp in all y+. K-ω SST model foresees, in the region between the ground and the tyre, a smoother shear of turbulent kinetic energy with respect to both K-ε models, leading to turbulent viscosity a smoother shear in the same zone. Regarding the Reynolds Stress model, the turbulent dissipation rate spreads out less than the other models due to the way it is calculated; its behaviour is similar to the K-ω SST one, with the exception of the big shear describing the separation in the upper part of the tyre, which is more smooth and with a more rapid decay.

Considering all the observations drawn, the use of fully resolved viscous sub-layer is the most sensitive and upgrading change that this work identifies.

From the contour of streamline velocity at the centerline, it is evident how the big diffusion and the high variation of turbulent viscosity in the middle created two separated vortex for the K-ε all y+, instead of a unique reversed flow zone, as all the other models provide; high values of ν_t near wall for both K-ε models cause the lower reversed zone to be wider with respect to the other models. The lower wake becomes smaller downstream as the region of turbulent viscosity shrinks when no wall law is applied. It is significant to note how upper shears calculated with Spalart-Allmaras and K-ε all y+ methods are comparable.

From the flow visualization in spanwise direction, it can be seen that K-ε models are very robust and insensitive to the asymmetry in spanwise direction; the others presents a smoother shear, without varying the form of the wake.

The vortices generated by the contact patch are well highlighted by the K-ω SST and the Spalart-Allmaras method, with a bigger height with respect to K-ε and Reynolds Stress Model and the interaction with the lower vortex of the wheel contributes to make the latter wider.

The contribution given by the unsteady simulation is limited if a steady solution is used as initial condition, and becomes nearly non-existent in the case of flow initialization.

Investigation of the tyre wake describes two pairs of contra-rotating vortices: the upper, affected only by the streamwise velocity, decays more rapidly than the lower, also due to the presence of the ground plane that energizes the vortex, and to the interaction with the contact patch. Also the shape of the rim can influence the width of the lower pair of vortices.

5.3 Further recommendations

For the next investigations, the author suggests to use another type of initialization: it could be useful to start a simulation using the results of a potential code, analysing the flow on the body and on the ground.

Since the best achievements in obtaining closer result to the experimental evidence are due to the changing in wall treatment, it is interesting to change the wall treatment in the simulations with turbulence model different from the K-ε one.

In the end, a more in-depth study of the shape of the contact patch could be executed, by modifying it in order to make it closer to the reality. A possibility is – for instance – to use the results of a FE structural analysis of the contact between the tyre and the ground plane in order to make the simulation as close as possible to the reality.

Bibliography

[1] Batchelor G. K. An *Introduction to Fluid Dynamics*. Cambridge University Press, 1967.

[2] Hajiloo A. et al. *Limited Mesh Refinement Study of the Aerodynamic Flow Field Around a Car-Like Shape: Computational Verses Experimental Fluid Dynamics*. Technical Report 960677, SAE, 1996.

[3] Ramnefors M. et al. *Accuracy of Drag Predictions on Cars using CFD – Effect of Grid Refinement and Turbulence Models*. Technical Report 960681, SAE, 1996.

[4] Axelsson N. et al. *Accuracy in Computational Aerodynamics Part 1: Stagnation Pressure.* Technical Report 980037, SAE, 1998.

[5] Perzon S. et al. *Accuracy in Computational Aerodynamics Part 2: Base Pressure*. Technical Report 980038, SAE, 1998.

[6] Dhaubhadel M.N. Review: CFD Applications in the Automotive Industry. *Journal of Fluids Engineering*, 118(4):647-653, December 1996.

[7] Fackrell J.E. *The Aerodynamic Characteristics of an Isolated Wheel Rotating in Contact with the Ground.* PhD thesis, Imperial College, University of London, 1974

[8] Axon L. *The aerodynamic characteristics of automobile wheels – CFD prediction and wind tunnel experiment*, PhD thesis, Cranfield University, 1999

[9] Morelli A. *Aerodynamic Effects of an Automobile Wheel.* Technical Report Trans 47/69, MIRA, 1969.

[10] Morelli A. *Aerodymanic Actions on an Automobile Wheel*. In Scibor-Rylski A.J., editor, *Road Vehicle Aerodynamics - Proceedings of the First Symposium on Road Vehicle Aerodynamics, City University*, 1970.

[11] Stapleford W.R. and Carr G.W. *Aerodynamic Characteristics of Exposed Rotating Wheels.* Technical Report 1970/2, MIRA, 1970

[12] Fackrell J.E. and Harvey J.K. *The Flow Field and Pressure Distribution of an Isolated Road Wheel*. In Stephens.H.S., editor, *Advances in Road Vehicle Aerodynamics.* BHRA Fluid Engineering, 1973.

[13] Fackrell J.E. and Harvey J.K. *The Aerodynamics of an Isolated Road Wheel.* In Pershing B., editor, *Proceedings of the Second AIAA Symposium of Aerodynamics of Sports and Competion Automobiles,* 1975.

[14] Cogotti A. Aerodynamic Characteristics of Car Wheels. In *Technological Advances in Vehicle Design Series, SP3 - Impact of Aerodynamics on Vehicle Design,* pages 173-196. International Journal of Vehicle Design, 1983.

[15] Bearman P.W. et al. *The Effect of a Moving Floor on Wind Tunnel Simulation of Road Vehicles.* Technical Report 880245, SAE, 1988.

[16] Hilhorst R. and Giachi M. *An Experimental Study on Drag Evaluation Referred to the Geometry of the Formula One Racing Car Tires*. In *Proceedings of the Royal Aeronautical Society Vehicle Aerodynamics Conference*, 1994.

[17] Schiefer.U. et al. *Two Different Approaches to a Better Simulation of Road Conditions in the Wind Tunnel*. In *Proceedings of the MIRA International Conference on Vehicle Aerodynamics,* 1996.

[18] B. Basara, D. Beader, and V. P. Przulj. *Numerical simulation of the air flow around a rotating wheel*. In *Proc. of 2nd MIRA International Conference on Vehicle Aerodynamics,* Birmingham, UK, October 1998.

[19] A. F. Skea, P. R. Bullen, and J. Qiao. The use of CFD to predict the air flow around a rotating wheel. In *Proc. of 2nd MIRA International Conference on Vehicle Aerodynamics,* Birmingham, UK, October 1998.

[20] A. Waschle, S. Cyr, T. Kuthada, and J. Wiedermann. *Flow around an isolated wheel – Experimental and numerical comparison of two CFD codes.* Technical Paper 2004-01-0445, Society of Automotive Engineers, Warrendale, PA, 2004.

[21] Knowles R.D. *Monoposto Race car wheel aerodynamics: investigation of near wake structure & support sting interferences*. PhD Thesis, Cranfield University, 2005

[22] Saddington A.J., Knowles R.D., Knowles K., Laser Doppler anemometry measurement in the near wake of an isolated Formula One wheel, Exp Fluids 42:671-681, Springer, 2007

[23] Axerio J. Iaccarino G. et al, *Computational and Experimental investigation of the flow structure and vortex Dynamics in the wake of a Formula One Tire*. Paper 09B-0082, Society of Automotive Engineers, 2009

[24] Basara, B., Beader, D., and Przulj, V., *Numerical Simulation of the Air Flow Around a Rotating Wheel*. 3rd MIRA International Vehicle Aerodynamics Conference, Rugby, U.K., 18–19 October 2000.

[25] McManus J., Zhang X., *A computational Study of the flow around an isolated wheel in contact with the ground*, Journal of Fluids Engineering, n 128, pgg 520-530, May 2006.

[26] Pope A., Turbulent Flows, Cambridge University Press, U.K., 2000.

[27] NX, user's guide.

[28] ANSA, user's guide.

[29] STARCCM+, user's guide.

[30] Wilcox, D.C. 1998. *Turbulence Modeling for CFD*, 2nd edition, DCW Industries, Inc.

[31] Menter, F.R. 1994. *Two-equation eddy-viscosity turbulence modeling for engineering applications*, *AIAA Journal* **32**(8) pp. 1598-1605.

[32] Durbin, P.A. 1996. *On the k-ε stagnation point anomaly, Int. J. Heat and Fluid Flow* **17,** pp. 89-90.

[33] Spalart, P.R., and Allmaras, S.R. 1992. *A one-equation turbulence model for aerodynamic flows*, AIAA-92-0439.

[34] Dacles-Mariani, J., Zilliac, G., Chow, J.S., and Bradshaw, P. 1995 *Numerical/experimental study of a wingtip vortex in the near field*, *AIAA Journal*, **33**(9), pp. 1561-1568.

[35] Rodi, W. 1991. *Experience with Two-Layer Models Combining the k-ε Model with a One-Equation Model Near the Wal*", 29th Aerospace Sciences Meeting, January 7-10, Reno, NV, AIAA 91-0216.